Investigations of Earthquake Source Processes Based on Fault Models with Variable Friction Rheology

Thesis by

Yoshihiro Kaneko

In Partial Fulfillment of the Requirements

for the Degree of

Doctor of Philosophy

California Institute of Technology

Pasadena, California

2009

(Defended January 30, 2009)

Acknowledgements

First and foremost, I would like to express my sincere gratitude to my advisor Nadia Lapusta, for all her support, patience, and guidance during the course of my graduate study. Nadia is always willing to spend hours with me on discussing my research, and has always taken extremely good care of me and other students. I also deeply appreciate her support while allowing me to pursue my ideas in the middle of my PhD.

I would like to thank all other members of my committee, Jean-Philippe Avouac, Pablo Ampuero, Tom Heaton, and Rob Clayton for reviewing my thesis and providing valuable suggestions and criticism. I am especially grateful to Jean-Philippe and Pablo for our research collaboration that resulted in parts of this thesis. The research with Jean-Philippe originated from his well-taught reading course (Ge 277) that motivated me to explain observations of seismic and aseismic slip. I have greatly benefited from discussions about earthquake physics with Tom Heaton. Rob Clayton has been a very good academic advisor.

Discussions with and lectures of Nadia Lapusta, Hiroo Kanamori, Jeroen Tromp, Don Helmberger, Mark Simons, Rob Clayton, and Mike Gurnis have taught me a lot both about scientific subjects and about ways to investigate them. I thank them for sharing their knowledge and insight with me.

My sincere appreciation extends to my current and former colleagues. It has been a pleasure to discuss research with Yi Liu, Carl Tape, Elisabeth Nadin, Ozgun Konca, Eun-Seo Choi, Daoyuan Sun, Ravi Kanda, Qinya Liu, Xiao Lu, Ting Chen, and Hiro Noda. Frequent discussions with Yi Liu helped me to gain analytical insights for my complicated numerical results. My PhD study would not have been smooth and fun without the friendship of Carl and Elisabeth.

My understanding of earthquake source physics was enhanced by discussions with and suggestions from researchers outside of Caltech, among them Allan Rubin, Yehuda Ben-Zion, Paul Segall, Ralph Archuleta, Terry Tullis, Joan Gomberg, Jim Rice, and Eric Dunham. I am grateful to all of them. I thank Yue Tian and Allan Rubin for giving me the permission to use their figures in this thesis and for providing me with digital copies of them.

I thank my parents in Japan for their understanding and support throughout my undergraduate and graduate studies in the United States. At last, I want to express my big thanks to my wife, Misaki, for her love, friendship, and support that made this work possible and enjoyable.

Abstract

Ample experimental and observational evidence suggests that friction properties on natural faults vary spatially. In the lab, rock friction depends on temperature and confining pressure and it can be either velocity weakening or velocity strengthening, leading to either unstable or stable slip. Such variations in friction rheology can explain patterns of seismic and aseismic fault slip inferred from field observations.

This thesis studies earthquake source processes using models with relatively simple but conceptually important patterns of velocity-weakening and velocity-strengthening friction that can arise on natural faults. Based on numerical and analytical modeling, we explore the consequences of such patterns for earthquake sequences, interseismic coupling, earthquake nucleation processes, aftershock occurrence, peak ground motion in the vicinity of active faults, and seismic slip budget at shallow depths. The velocity-dependence of friction is embedded into the framework of logarithmic rate and state friction laws.

In addition to using existing boundary integral methods, which are accurate and efficient in simulating slip on planar faults embedded in homogeneous elastic media, the thesis develops spectral element methods to consider single dynamic ruptures and long-term histories of seismic and aseismic slip in models with layered bulk properties.

The results of this thesis help to understand a number of observed fault slip phenomena, such as variability in earthquake patterns and its relation to interseismic coupling, seismic quiescence following decay of aftershocks at inferred rheological transitions, instances of poor correlation between static stress changes and aftershock occurrence, the lack of universally observed supershear rupture near the free surface, and coseismic slip deficit of large strike-slip earthquakes at shallow depths. The models, approaches, and numerical methods developed in the thesis motivate and enable consideration of many other earthquake source problems, such as the combined effect of two or more triggering mechanisms on aftershock rates, inferring friction properties on natural faults based on seismic and geodetic measurements, seismic hazard assessment based on observed interseismic coupling, and the effect of heterogeneous and/or nonelastic bulk properties on earthquake sequences.

Contents

5 Spectral Element Modeling of Spontaneous Earthquake Rupture on Rate and State Faults: Effect of Velocity-Strengthening Fault Friction at Shallow Depths on Dynamic Rupture **113**

List of Figures

List of Tables

Chapter 1

Introduction

Observations of seismic and aseismic slip on natural faults show spatio-temporal complexity at a number of scales. This complexity is manifested by small and large earthquakes, processes of earthquake nucleation, postseismic slip, creeping segments, and aseismic transients often accompanied by seismic tremor. At least some of the complexity is likely caused by spatial variations in fault friction properties. In laboratory experiments, variability of friction properties is found in different rock types or the same rock type under different physical conditions. Understanding the consequences of such heterogeneities for seismic and aseismic slip is an interesting and fundamental scientific problem, which is also very important for seismic hazard assessment.

In this thesis, we investigate earthquake source processes by constructing models with relatively simple but conceptually important patterns of velocity-weakening and velocity-strengthening properties that can arise on natural faults.

1.1 Observational and experimental evidence for systematic variations in friction properties on natural faults

Evidence for variations in fault friction properties with the rock types, confining pressure, and temperature have been found in a number of laboratory studies. In particular, rate- and state-dependent friction laws (called rate and state friction laws in this work) have been developed based on rock friction experiments [e.g., *Dieterich*, 1978, 1979; *Ruina*, 1983; *Tullis*, 1988; *Blanpied et al.*, 1995; *Marone*, 1998] for slip velocities from 10^{-8} to 10^{-3} m/s. The laws reflect variations of frictional shear strength of various materials due to their dependence on slip velocity (also called slip rate) and on a state variable or variables that describe(s) the evolving properties of the contact surface. In the standard aging formulation for situations with time-independent effective normal stress $\bar{\sigma}$, the shear strength τ is expressed as

$$\tau = \bar{\sigma}\mu = \bar{\sigma}\left[\mu_0 + a\ln\left(\frac{V}{V_0}\right) + b\ln\left(\frac{V_0\theta}{L}\right)\right] , \tag{1.1}$$

$$\frac{d\theta}{dt} = 1 - \frac{V\theta}{L} , \tag{1.2}$$

where $a > 0$ and $b > 0$ are rate and state constitutive parameters, V is slip velocity, μ_0 is the reference friction coefficient corresponding to the reference slip velocity V_0, θ is a state variable which can be interpreted as the average age of the population of contacts between two surfaces, and L is the characteristic slip for state evolution [e.g., *Dieterich*, 1978, 1979; *Rice and Ruina*, 1983; *Ruina*, 1983; *Dieterich and Kilgore*, 1994]. Parameters a, b, and L depend on a number of factors, such as rock types, effective normal stress $\bar{\sigma}$, and bulk temperature. Note that other equations for state-variable evolution and formulations with two and more state variables have been proposed [*Ruina*, 1983; *Rice and Ruina*, 1983; *Gu et al.,* 1984; *Kato and Tullis*, 2001]. Recent studies [*Bayart et al.*, 2006; *Ampuero and Rubin*, 2008] rekindled the discussion of which state evolution law matches experiments better, and this is a subject of active research.

Another subject of active research on fault friction is enhanced dynamic weakening at seismic slip velocities. There is growing evidence that friction is lower at seismic slip velocities than rate and state friction laws predict [e.g., *Toro et al.*, 2003; *Rice*, 2006; *Han et al.*, 2007; *Lu et al.*, 2007, and references therein]. One of the consequences of such additional weakening, in particular of its rate-dependent formulation, is the promotion of self-healing or pulse-like ruptures [e.g., *Heaton*, 1990; *Lu et al.*, 2007, and references therein]. Conclusions in this thesis have been drawn on the basis of the standard rate and state friction framework, without the inclusion of enhanced dynamic weakening. Verifying the conclusions with the rate and state framework extended to include dynamic weakening mechanisms remains a goal for future work.

Rate and state friction has been successfully used to model and explain various earthquake phenomena including earthquake nucleation, postseismic slip, foreshocks, aftershocks, aseismic transients, small repeating earthquakes, the variability of earthquake source duration, and the stability of the pattern of seismic asperities [e.g., *Rice and Ruina*, 1983; *Ruina*, 1983; *Tse and Rice*, 1986; *Marone et al.*, 1991; *Dieterich*, 1992, 1994; *Tullis*, 1996; *Ben-Zion and Rice*, 1997; *Gomberg et al.*, 1998; *Marone*, 1998; *Scholz*, 1998; *Bilek and Lay*, 2002; *Lapusta and Rice*, 2003; *Perfettini et al.*, 2003; *Bilek et al.*, 2004; *Yamanaka* *and Kikuchi*, 2004; *Liu and Rice*, 2005; *Miyazaki et al.*, 2006; *Kaneko and Lapusta*, 2008; *Chen and Lapusta*, 2009]. Stability of sliding and nucleation of seismic slip on rate and state faults governed by laws (1.1) and (1.2) have been considered in a number of theoretical studies [*Rice and Ruina*, 1983; *Ruina*, 1983; *Dieterich*, 1992; *Rice et al.*, 2001; *Rubin and Ampuero*, 2005]. Fault regions with $a - b > 0$ have steady-state velocity-strengthening friction properties and tend to slip in a stable manner with the imposed loading rate. Fault regions with $a - b < 0$ have steady-state velocity-weakening properties and are capable of producing earthquakes. However, even on steady-state velocity-weakening fault regions, sufficiently small slipping zones cannot develop fast slip under slow tectonic loading, and the slipping zone has to become large enough to produce a rapid sliding event. Throughout this thesis, we omit the words “steady-state” and simply refer to velocity weakening/strengthening. The aseismic process of slow and gradually accelerating slip in a small, slowly varying zone that eventually leads to unstable slip is often referred to as a nucleation process. The term “unstable slip” typically refers to simulated earthquakes that are inertially controlled events characterized by rapid expansion of the slipping zone with rupture speeds that are a significant fraction of wave speeds and slip velocities much larger than the loading rate.

Hence analysis of rate and state laws predicts that fault regions can either slip stably or produce stick-slip motion, depending on whether they are velocity weakening or velocity strengthening. Evidence of such behavior on natural faults comes from measurements of surface deformation. Due to recent progress in geodetic, paleogeodetic, and remote-sensing techniques to monitor surface deformation, it is becoming clear that, in the inter-

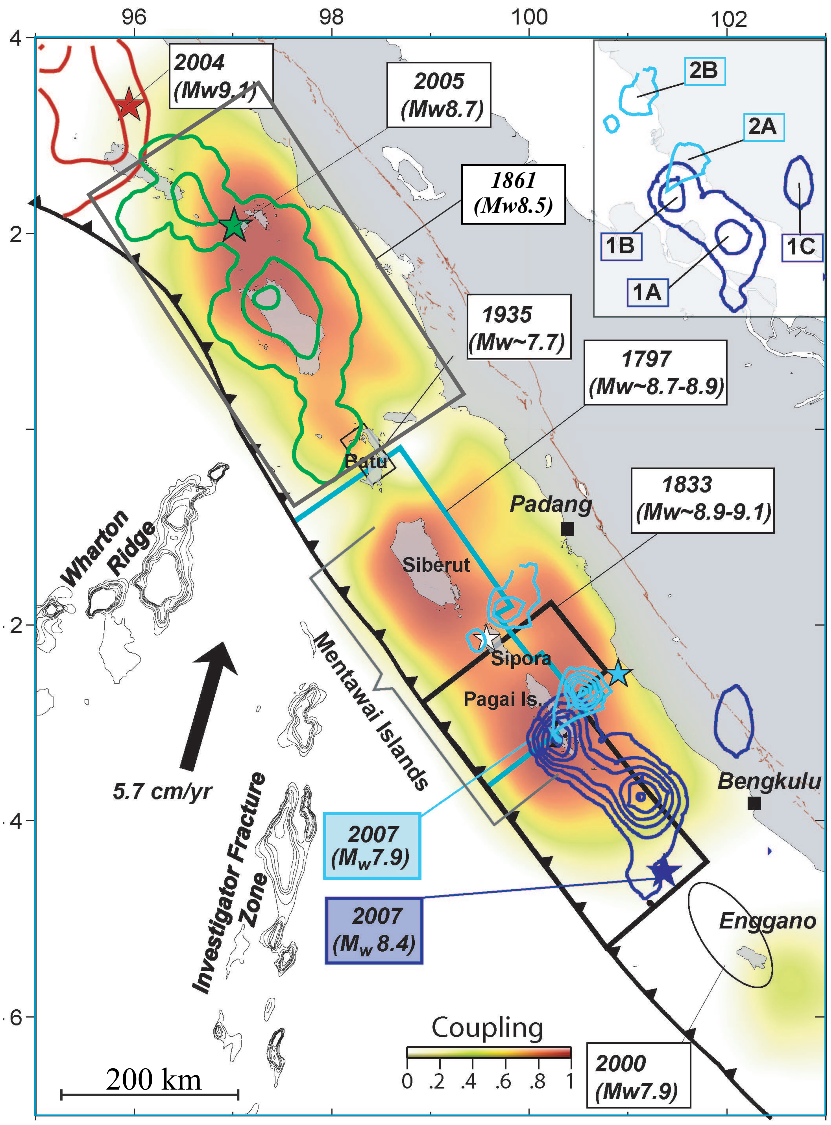

Figure 1.1: The pattern of locking of the plate interface along the subduction zone offshore Sumatra (Figure adopted from *Chlieh et al.* [2008]). Comparison of interseismic coupling along the megathrust with the rupture areas of the giant 1979, 1833, 1861, and 2005 earthquakes [*Chlieh et al.*, 2008]. Background color represents interseismic coupling obtained by modeling of coral and GPS data. Green and red 5-m contour lines of slip for the 2004 Sumatra-Andaman and 2005 Nias-Simeulue earthquakes are from *Chlieh et al.* [2007] and *Briggs et al.* [2006], respectively. Outermost contours depict the limits of rupture. Ruptures during the great 1797 and 1833 earthquakes are from elastic dislocation models based on uplift of coral microatolls [*Natawidjaja et al.*, 2006].

seismic period of stress build up between successive large earthquakes, some fault areas remain locked while others are creeping. The pattern of interseismic coupling, defined as the ratio of interseismic slip deficit divided by the long term slip, is thus generally found to be heterogeneous [*Freymueller et al.*, 2000; *Igarashi et al.*, 2003; *Fournier and Freymueller*, 2007; *Chlieh et al.*, 2008]. This observation suggests interfingering of velocity-weakening and velocity-strengthening regions on a given fault segment. The example of the Sunda megathrust is particularly instructive (Figure 1.1). There, the pattern of locking of the Sunda megathrust in the interseismic period shows both downdip and along strike variations [*Hsu et al.*, 2006; *Chlieh et al.*, 2008]. Some regions on the megathrust remain locked in the interseismic period and accommodate large earthquakes occasionally, while others, e.g., the Batu Islands area near the equator and Enggano area, indicate continuous interseismic creep. Observation of postseismic deformation following the 2005 Nias earthquake additionally revealed that its coseismic slip area is surrounded by areas with rapid afterslip, and therefore are governed by velocity-strengthening friction [*Hsu et al.*, 2006].

The variations of friction properties on natural faults have also been inferred to be strongly depth dependent (e.g., Figure 1.1). The transition from velocity weakening to velocity strengthening at the base of seismogenic zone has been understood in laboratory experiments as the effect of increasing temperature with depths [*Blanpied et al.*, 1991, 1995]. In addition, accumulating evidence supports the presence of velocity-strengthening friction at shallow depths. In laboratory experiments, rock friction at low normal stress typically exhibits velocity-strengthening behavior due to unconsolidated fault gouge [e.g., *Marone et al.*, 1991; *Marone*, 1998]. Studies of interseismic shallow creep [e.g., *Lyons* *et al.*, 2002], shallow afterslip of large earthquakes [e.g., *Marone et al.*, 1991; *Marone*, 1998; *Hsu et al.*, 2006], and the deficit of seismicity at shallow depths [e.g., *Shearer et al.*, 2005] provide indirect observational evidence for velocity-strengthening fault rheology at shallow depths.

Finally, heterogeneities of fault friction properties may exist on a wide range of scales. For example, microearthquake studies in various tectonic settings provide some evidence on interfingering of velocity-weakening and velocity-strengthening patches [*Schaff et al.*, 2002; *Nadeau and McEvilly*, 2004; *Igarashi et al.*, 2003; *Bourouis and Bernard*, 2007]. Those earthquakes repeatedly rupture isolated fault segments, indicating that their ruptured areas are surrounded by velocity-strengthening regions and suggest that heterogeneities of fault friction proprieties exist even in much smaller scales than the scale shown in Figure 1.1.

Given that heterogeneities in friction properties commonly exist on natural faults, it is important to understand the role of systematic variations in friction properties on seismic and aseismic slip. In this thesis, we investigate the consequences of such variations for earthquake sequences, interseismic coupling, earthquake nucleation processes, aftershock occurrence, peak ground motion in the vicinity of active faults, and seismic slip budget at shallow depths.

1.2 Understanding patterns and interactions of seismic and aseismic fault slip

One ultimate goal of seismotectonic studies is to provide ways of assessing the timing, spatial extent, and moment of seismic ruptures. Simple conceptual models assume that rupture segmentation is persistent and that earthquake timing and moment are related due to requirement that, in the long term, any point of a given fault has to slip seismically, in order to make up for slip deficit given by the secular relative motion of the adjacent stably slipping domains. These simple models predict the quasi-periodic repetition of "characteristic" earthquakes with similar rupture extent and moment [*Schwartz and Coppersmith*, 1984] or a time-predictable or slip-predictable behavior if non-quasi-periodic behavior is allowed [*Shimazaki and Nakata*, 1980]. As observations have accumulated, it has become quite evident that none of these simple models are applicable to natural faults [*Schwartz*, 1999; *Murray and Segall*, 2002; *Weldon et al.*, 2004]. This is not surprising since interactions due to stress transfers within a fault system favor complex chaotic behavior [e.g., *Cochard and Madariaga*, 1996]. However, real fault systems might, in fact, obey some systematic behaviors in terms of their segmentation [*Thatcher*, 1990] and the timing of major earthquakes [*Sieh et al.*, 2008]. The spatial extent of seismic ruptures seems to be, in part, controlled by geometrical complexities such as local non-planarity and fault stepovers [*Wesnousky*, 2006]. As discussed in Section 1.1, there is also growing evidence that spatial variations of fault friction properties is another important factor that could influence both the spatial extent, the size, and the timing of earthquake ruptures, an issue that is the focus of Chapter 2.

As shown in well-studied behavior of the Sunda megathrust (Figure 1.1), some fault regions tend to rupture in repeating similar "characteristic" earthquakes while others behave irregularly, with quite different rupture area and amount of slip in successive seismic ruptures [*Hsu et al.*, 2006; *Chlieh et al.*, 2008; *Konca et al.*, 2008; *Sieh et al.*, 2008]. This behavior seems to depend on areas of low interseismic coupling, which can act as systematic or non-systematic barriers to seismic rupture [*Chlieh et al.*, 2008]. However, previous studies showed that the relationship leading to heterogeneous interseismic stress and strain build up is not unique [e.g., *Dmowska and Lovison*, 1992]. Velocity-weakening segments expected to rupture during earthquakes may accumulate partial amounts of interseismic slip. Furthermore, velocity-strengthening patches do not necessarily creep significantly in the interseismic period [e.g., *Bürgmann et al.*, 2005]. For example, the distribution of seismic asperities in the Kurile-Japan trench seems to be relatively stationary [*Yamanaka and Kikuchi*, 2004] and lie within a zone with high interseismic coupling [*Ito et al.*, 2000]. The area between the asperities could obey velocity-strengthening friction but might not creep significantly in the interseismic period because of the stress shadow effect of the neighboring velocity-weakening segments. In that case, the interfingering of velocity-weakening and velocity-strengthening regions is best inferred from the comparison of seismic slip and afterslip distribution [*Miyazaki et al.*, 2004; *Baba et al.*, 2006]. The details of how the pattern of interseismic coupling relates to earthquake ruptures is thus not straightforward.

In Chapter 2, we construct a simple fault model that reproduces behaviors observed on the Sunda megathrust due to variations in friction properties. We use the simulation methodology developed by *Lapusta et al.* [2000] that resolves for all stages of each earthquake episode: the aseismic nucleation process in gradually varying zones of accelerating slip, the subsequent inertially controlled event (unstable slip) with realistic slip velocities and rupture speeds, the postseismic slip, and the interseismic quasi-static deformation between events. A fault region of high interseismic coupling is modeled as two segments with velocity-weakening friction separated by a relatively small velocity-strengthening patch. The width and friction properties of the velocity-strengthening patch are varied so that some events are stopped by the patch and hence rupture only one locked segment, while others propagate through the patch, rupturing both locked segments and resulting in larger earthquakes. In the latter case, the patch causes a decrease in seismic potency rate. By varying the strength and width of the velocity-strengthening patch, we identify parameter regimes in which such a patch acts either as a “permanent” or as a “intermittent” barrier. Depending on the characteristics of intervening velocity-strengthening areas, seismic asperities can either rupture in isolation or simultaneously, leading to the kind of complexity observed on the Sunda megathrust.

We find that the probability that an earthquake breaks through the velocity-strengthening patch can be quantified by a non-dimensional parameter B that depends on friction properties and sizes of both the velocity-strengthening patch and velocity-weakening regions. Parameter B also characterizes the effect of the variation in friction properties on interseismic coupling, which can be observed from geodetic or remote-sensing measurements. Patches with higher values of B result in locally lower interseismic coupling and act as permanent barriers to seismic rupture. We find that interseismic coupling as high as 0.75 can indicate a permanent barrier. Patches with a range of lower values of B lead to a more subtle effect on interseismic coupling, decreasing it from 1 to values between 0.75 and 0.95, but such patches can have a profound effect on the pattern of seismic ruptures, resulting in complex sequences of large earthquakes with quite different rupture area and amount of slip in successive seismic ruptures.

1.3 Modeling earthquake nucleation and aftershock occurrence

One special case of interaction between aseismic and seismic slip is the nucleation process, i.e., aseismic, gradually accelerating, slip in a slowly varying zone that eventually leads to a seismic event. Understanding earthquake nucleation is an important yet difficult task due to lack of direct observations such as in situ measurements at seismogenic depths. A widely accepted model for earthquake nucleation is a developing frictional instability on a preexisting fault, the phenomenon inferred from laboratory experiments and theoretical studies.

In Chapter 3, we simulate and compare several plausible scenarios of earthquake nucleation in continuum models of rate and state faults. Two fault models are used to create two different environments for earthquake nucleation. The first model incorporates uniform velocity-weakening friction properties and a weaker patch of slightly (10%) lower effective normal stress. By varying the size of the weaker patch, we can either achieve completely homogeneous fault properties within the nucleation zone or induce normal-stress heterogeneity there. This is a realistic nucleation scenario, as faults can contain such weaker patches for a number of reasons that include local fault non-planarity or spatial variations in pore pressure. At the same time, observations suggest that earthquakes tend to cluster at inferred transitions from locked to creeping regions [e.g., *Schaff et al.*, 2002; *Bollinger et al.*, 2004; *Waldhauser et al.*, 2004]. We explore that scenario in the second model that contains a rheological transition from velocity-strengthening to velocity-weakening friction. Such transitions create stress concentrations that promote earthquake nucleation.

Nucleation processes are simulated as a part of spontaneously occurring earthquake sequences on a fault that is subjected to slow, tectonic-like loading [*Lapusta et al.*, 2000]. This approach allows us to study nucleation processes that naturally develop in our models, with conditions before the nucleation originating from the previous stages of earthquake occurrence and not from arbitrarily selected initial conditions that one would need to impose to study only one instance of earthquake nucleation.

We consider five representative cases of earthquake nucleation, compare them in terms of their slip-velocity evolution, and discuss the effects of heterogeneity in normal stress, heterogeneity in friction properties, and variations in loading. We find significant differences among the simulated nucleation processes. Different loading histories lead to different nucleation processes and sizes of nucleation zones. Nucleation processes at weaker patches behave similarly to theories based on spring-slider models, with some notable deviations, whereas nucleation processes at rheological transitions behave differently, producing complex slip-velocity histories. These differences have important implications for aftershock phenomena as discussed in Chapter 4.

Studying nucleation processes has also been motivated by aftershock occurrence. Earthquakes are typically followed by increased seismic activity, usually referred to as aftershock sequences, that decays over time. The decay of aftershocks is well described empirically by Omori's law (see *Utsu et al.* [1995] for a recent review). Several different mechanisms have been proposed to explain the occurrence and time evolution of aftershocks, including including increased loading rate due to aseismic processes such as postseismic slip [e.g., *Benioff*, 1951; *Perfettini and Avouac*, 2004] or relaxation of the viscoelastic lower crust [e.g., *Freed and Lin*, 2001], pore fluid motion and induced variations in fault strength [e.g., *Nur and Booker*, 1972; *Bosl and Nur*, 2002], triggering due to dynamic stress changes [e.g., *Hill et al.*, 1993; *Gomberg et al.*, 2003; *Felzer and Brodsky*, 2006], evolution of viscoelastic damage rheology due to sudden increase in strain [e.g., *Ben-Zion and Lyakhovsky*, 2006], and accelerated nucleation on rate and state faults due to static stress changes induced by the mainshock [*Dieterich*, 1994].

In Chapter 4, we build on the model proposed by *Dieterich* [1994] and explore the aftershock behavior due to static perturbations of rate and state nucleation processes using continuum earthquake models. The full explanation for aftershocks may well involve a combination of mechanisms, with different mechanisms potentially dominating in different situations or during different stages of aftershock sequences. However, it becomes increasingly clear that rate and state friction is a good description of the fault constitutive response during slow slip, and hence accelerated rate-and-state nucleation due to static stress changes has the potential to significantly contribute to all aftershock sequences.

Dieterich [1994] built an aftershock model that reproduced Omori's law using static triggering of rate and state nucleation sites. In that model, a preexisting population of rate and state nucleation sites is perturbed by static stress changes due to a mainshock. In the population, each nucleation site is governed by the same nucleation process but time-shifted in such a way that the population results in a constant background seismicity rate. After a positive static shear stress step, the nucleation process at each site accelerates, producing an increased seismicity rate (or aftershock rate) that matches Omori's law for a wide range of parameters. An important ingredient in this aftershock model is the nucleation process and its response to static stress changes. In *Dieterich* [1994], the nucleation process was specified in terms of its slip-velocity evolution. To obtain the evolution, two simplifications in modeling nucleation were used: (i) elastic interactions were described by a one-degree-of-freedom spring-slider system and (ii) the assumption $V\theta/L \gg 1$ was used to simplify the rate and state friction formulation based on a study of earthquake nucleation in a continuum model [*Dieterich*, 1992]. These simplifications allowed the derivation of analytical expressions for both slip-velocity evolution during nucleation and the resulting aftershock rate. The approach of *Dieterich* [1994] has been further explored in a number of works [*Gomberg et al.*, 1998, 2000; *Gomberg*, 2001; *Gomberg et al.*, 2005] and has been used to interpret observed aftershock sequences [*Gross and Kisslinger*, 1997; *Gross and Bürgmann*, 1998; *Toda et al.*, 1998, 2005]. In particular, aftershock rates based on simulations in spring-slider systems with the full aging rate and state formulation were found to follow the results of *Dieterich* [1994] quite well, validating simplification (ii) for spring-slider models.

Given the determining role of the nucleation process in the aftershock model of *Di-*

eterich [1994] and subsequent studies, it is important to understand whether spring-slider models provide a good approximation of the nucleation process on natural faults. Spring-slider models approximate a slip zone of a constant size (inversely proportional to the spring stiffness assumed) with uniform slip and stress history throughout the slip zone and simplified elastic interaction with the surrounding bulk. Hence spring-slider models cannot represent spatially inhomogeneous aseismic slip in a zone of evolving size, which is a characteristic feature of nucleation processes in models that incorporate both rate and state friction laws and elastic continuum [*Rice*, 1993; *Lapusta and Rice*, 2002, 2003; *Rubin and Ampuero*, 2005].

In Chapter 4, we study the response of the simulated nucleation processes to static stress changes and the resulting aftershock rates, compare them with the results of *Dieterich* [1994], and explain the observed similarities and differences. We find that the model with a weaker patch behaves similarly to the spring-slider model of *Dieterich* [1994], while the model with rheological transition exhibits qualitatively different behavior. In particular, aftershock rates are affected by normal-stress heterogeneity in the nucleation zone. Nucleation processes at rheological transitions behave differently, producing complex slip-velocity histories, non-monotonic responses to static stress changes, and aftershock rates with pronounced peaks and seismic quiescence. For such processes, positive stress steps sometimes delay nucleation of seismic events by inducing aseismic transients that relieve stress and postpone seismic slip. Superposition of the complex aftershock response for spatially variable stress changes results in Omori's law for a period of time followed by seismic quiescence. Such behavior was observed at the base of the seismogenic zone near the 1984 Morgan Hill earthquake. We show that the computed aftershock rates are linked to unperturbed slip-velocity evolution in the nucleation zone and construct simplified analytical scenarios that explain some features of the response. The qualitative differences we find between the two nucleation models indicate that aftershock response of rate and state faults to static stress changes would depend on the conditions under which nucleation occurs on natural faults and may be different from predictions based on spring-slider models.

1.4 Developing a spectral element method (SEM) for simulations of fault slip: Effect of velocity-strengthening fault friction at shallow depths on dynamic rupture

Understanding complex and realistic scenarios of seismic and aseismic slip demands accurate and efficient numerical models that incorporate appropriate fault constitutive laws. A common approach to model slip on a rate and state fault is to employ boundary integral methods (BIMs), which are used in Chapters 2 - 4. In BIMs, field quantities are considered only at the boundary of a domain, and integral expressions are used to account for elastic interactions with the surrounding media. In the framework of BIM, nucleation, rupture propagation, and arrest of earthquakes have been successfully modeled [e.g., *Ben-Zion and Rice*, 1997; *Lapusta et al.*, 2000]. However, these studies have been mostly restricted to planar faults embedded into a uniform elastic space. At the same time, observations point to complicated crustal structures with variable bulk properties, fault damage zones, and non-planar fault geometries. It is important to include those factors into earthquake models, combining them with laboratory-derived constitutive fault relations such as rate and state friction.

In Chapter 5, we develop a spectral element method (SEM) for simulating dynamic rupture on rate and state faults. Finite element methods (FEMs) and, in particular, spectral element methods (SEMs), can incorporate variable bulk properties and more complex fault geometries. Using a SEM for seismic wave propagation dates back to the study of *Komatitsch and Vilotte* [1998]. The 3D SEM we use was originally developed by *Komatitsch and Tromp* [1999]; our work is an extension of the study by *Ampuero* [2002] that incorporated a LSW fault boundary into the SEM framework. We have extended the formulation to rate and state faults. To validate the developed SEM approach, we have conducted detailed comparison of SEM and BIM simulation results obtained for an antiplane problem. Incorporating rate and state faults into a SEM formulation requires a semi-implicit numerical scheme which makes the implementation more challenging than that for LSW friction.

Using the developed SEM, we study how dynamic rupture is affected by a shallow fault region of velocity-strengthening friction. Accumulating evidence supports the presence of a velocity-strengthening region at shallow depths ($\lesssim$3 km), as discussed in Section 1.1. Hence, it is important to understand how this affects earthquake rupture dynamics and, as a consequence, ground motion and seismic hazard assessment in the vicinity of active faults. Furthermore, the shallow velocity-strengthening region may also be relevant for tsunami earthquakes in subduction zones as it may slow down the up-dip propagation of rupture, boost the low-frequency content, and promote tsunami generation [*Polet and Kanamori*, 2000; *Seno*, 2002]. In addition, a typical Earth bulk structure has strong variation of elastic parameters with depth. The reduction of elastic moduli near the free surface results in ground-motion amplification, and thus it has important consequences for seismic hazard [e.g., *Olsen*, 2000]. Such bulk variations cannot be accommodated with existing BIM formulations, while SEM can incorporate them with ease. We simulate dynamic rupture scenarios on a fault embedded in a layered bulk structure and studied how the peak ground motion at on- and off-fault sites is affected by the bulk structure combined with different fault rheologies.

We find that a shallow velocity-strengthening fault region can significantly alter dynamic rupture and ground motion. The velocity-strengthening region suppresses supershear propagation at the free surface occurring in the absence of such region, which could explain the lack of universally observed supershear rupture near the free surface. In addition, the velocity-strengthening region promotes faster falloff of slip velocity behind the rupture front and decreases final slip throughout the entire fault, causing a smaller average stress drop. The slip decrease is largest in the shallow parts of the fault, resulting in a depth profile of slip qualitatively consistent with observations of shallow coseismic slip deficit in large strike-slip earthquakes [*Fialko et al.*, 2005]. The shallow velocity-strengthening region also reduces the amplification of strong ground motion due to a low-velocity bulk structure.

Earthquake ruptures in Chapter 5 are nucleated either abruptly or relatively rapidly, as common in simulations of single-rupture scenarios [e.g., *Day et al.*, 2005; *Rojas et al.*, 2007; *Harris et al.*, 2009]. While the conclusions in that Chapter should not depend on the nucleation procedure, a number of earthquake problems (e.g., in Chapters 2 - 4) require the ability to simulate more gradual nucleation under slow tectonic loading, postseismic and other aseismic slip, and sequences of simulated earthquakes, while still accounting for inertial effects during simulated earthquakes. For simple fault geometries and a uniform elastic medium, this has been accomplished by BIM approaches [e.g., *Lapusta et al.*, 2000; *Lapusta and Liu*, 2009].

In Chapter 6, we develop a SEM that enables us to simulate long-term fault slip histories while allowing flexibility in fault geometry and bulk properties. The developed 2D model merges a quasi-static SEM with the fully dynamic SEM presented in Chapter 5. Merging two methods to simulate long-term fault slip punctuated by dynamic earthquake ruptures is challenging and requires the development of proper criteria for switching from the quasi-static to dynamic SEM and vice versa. In addition, modeling long-term slip histories of faults is challenging by itself due to the wide range of temporal and spatial scales involved. Slow loading requires tens to thousands of years in simulated time, and large earthquakes rupture faults that are tens to hundreds of kilometers long. At the same time, rapid fluctuations in stress and slip rate at the propagating dynamic rupture tip during an earthquake occur over distances of order meters and times of order a small fraction of a second. Properly resolving all of these processes demands an efficient and accurate numerical model. We thus set up an antiplane benchmark problem and validate the developed SEM approach by comparing SEM and BIM simulation results in a 2D model of small repeating earthquakes.

Using the developed formulation, we investigate the effect of both fault friction properties and bulk properties on coseismic slip deficit at shallow depths ($\lesssim$3 km). The consideration of the effect of friction properties is motivated by the results of Chapter 5 which shows, based on single rupture scenarios, that such deficit can be caused by a shallow fault region with velocity-strengthening friction. Now we can explore this effect in the context of long-term slip histories. The effect of bulk properties is considered to investigate another candidate mechanism of low initial stress in low-rigidity shallow bulk materials resulting from uniform tectonic strain suggested by *Rybicki and Yamashita* [1998]. We investigate both mechanisms in the context of an earthquake sequence using the developed SEM (Chapter 6). For the set of parameters we have considered, low-rigidity shallow bulk materials do not lead to coseismic slip deficit. While the low-rigidity materials do cause lower interseismic stress accumulation, they also cause dynamic amplification of coseismic slip rates, with the net effect on slip being nearly zero. At the same time, the addition of velocity-strengthening friction to shallow parts of the fault leads to coseismic slip deficit in all cases we have considered.

Chapter 2

Influence of Variations in Fault Friction Rheology on Earthquake Rupture Patterns and Interseismic Coupling

Some fault regions with high interseismic coupling (ISC) tend to rupture in repeating similar ’characteristic’ earthquakes while others behave irregularly, with quite different rupture area and amount of slip in successive seismic ruptures, as evidenced by the behavior of the Sunda megathrust [*Chlieh et al.*, 2008; *Konca et al.*, 2008]. In this Chapter, we construct a simple fault model based on rate and state friction that reproduces such behavior due to variability in friction properties. We then investigate effect of variations in friction properties on earthquake rupture patterns and interseismic coupling.

This Chapter is based on the manuscript in preparation by Y. Kaneko, J.-P. Avouac, and N. Lapusta.

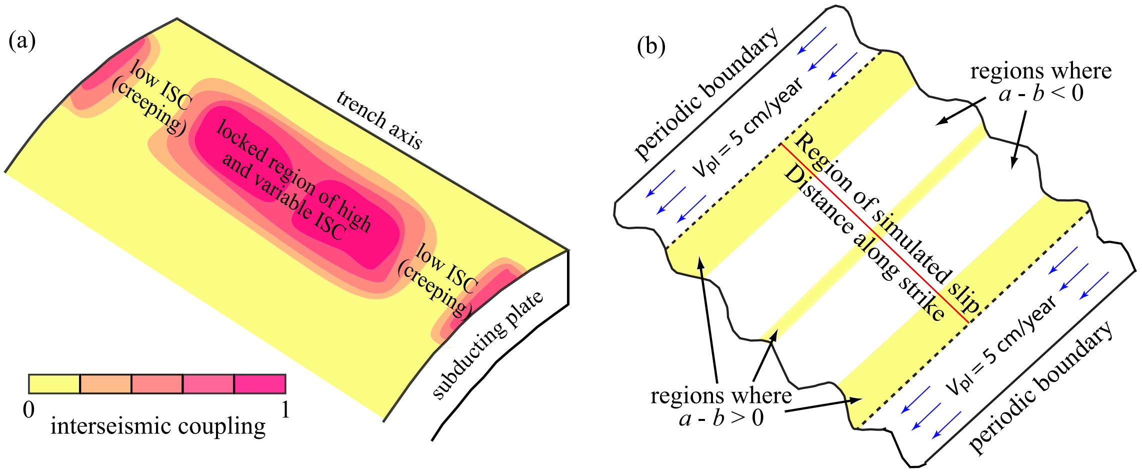

Figure 2.1: (a) Schematic illustration for spatial variations of interseismic coupling (ISC) on a plate interface along a generic subduction zone. The proportion of slip accommodated by interseismic creep varies spatially, from 0% in fully locked areas (ISC = 1) to 100% in areas creeping with the interplate rate (ISC = 0). (b) A sketch illustrating the fault model we use. The VS regions are indicated by yellow.

2.1 Numerical model of earthquake cycles with heterogeneous interseismic coupling

The model contains a planar fault governed by rate and state friction with the aging form of state variable evolution [*Dieterich*, 1978, 1979; *Ruina*, 1983] and embedded in a medium of homogeneous elastic properties (Appendix 2.6). The fault has two identical velocity-weakening (VW) segments separated and surrounded by velocity-strengthening (VS) regions (Figure 2.1b). We opt for a simple 2D implementation in which the fault has assumed distribution of a and b of rate and state constitutive parameters and is loaded by imposing a constant sliding velocity on both sides (Figure 2.2a). The edges of VS regions on both sides of the model are thus made to creep with the plate rate, leading to locally zero ISC. The computation of ISC is described in Appendix 2.8. The width of these VS patches is chosen large enough so that the seismic ruptures always taper off well before reaching the edges of the patches. These patches slip aseismically throughout the simulated time and thus represent permanent barriers (Figure 2b). As we show in the following, the width and friction properties of the central VS patch can be adjusted so that it acts as a permanent or intermittent barrier to the propagation of the seismic ruptures initiating on one or the other adjacent VW segments. To assign slip potency and magnitudes to the simulated earthquake, a downdip width of 40 km is assumed.

2.2 Earthquake sequence in presence of a velocity-strengthening (VS) patch

Despite the simple geometry and distributions of friction properties, the model produces rich earthquake patterns. An example is shown in Figure 2.2. Most earthquakes nucleate at the transitions from VS to VW regions, where interseismic stress accumulation rate is maximum. Some events remain small (e.g., events 3-7 in Figure 2.2b) while others propagate across the VW segments. The intervening VS patch sometimes acts as a barrier to the coseismic ruptures (Events 1, 26, and 33 in Figure 2.2b) even though, in this case, the effect of the VS patch on ISC is subtle (ISC $\sim$ 0.9). The VW segments are nearly fully locked (ISC $\sim$ 1) and generally correspond to the places of high coseismic slip (in other words, they form seismic asperities). Larger earthquakes generally produce larger slip at the same fault location, consistent with nearly constant stress drop.

This simple example qualitatively explains the complex sequence of recent and histor-

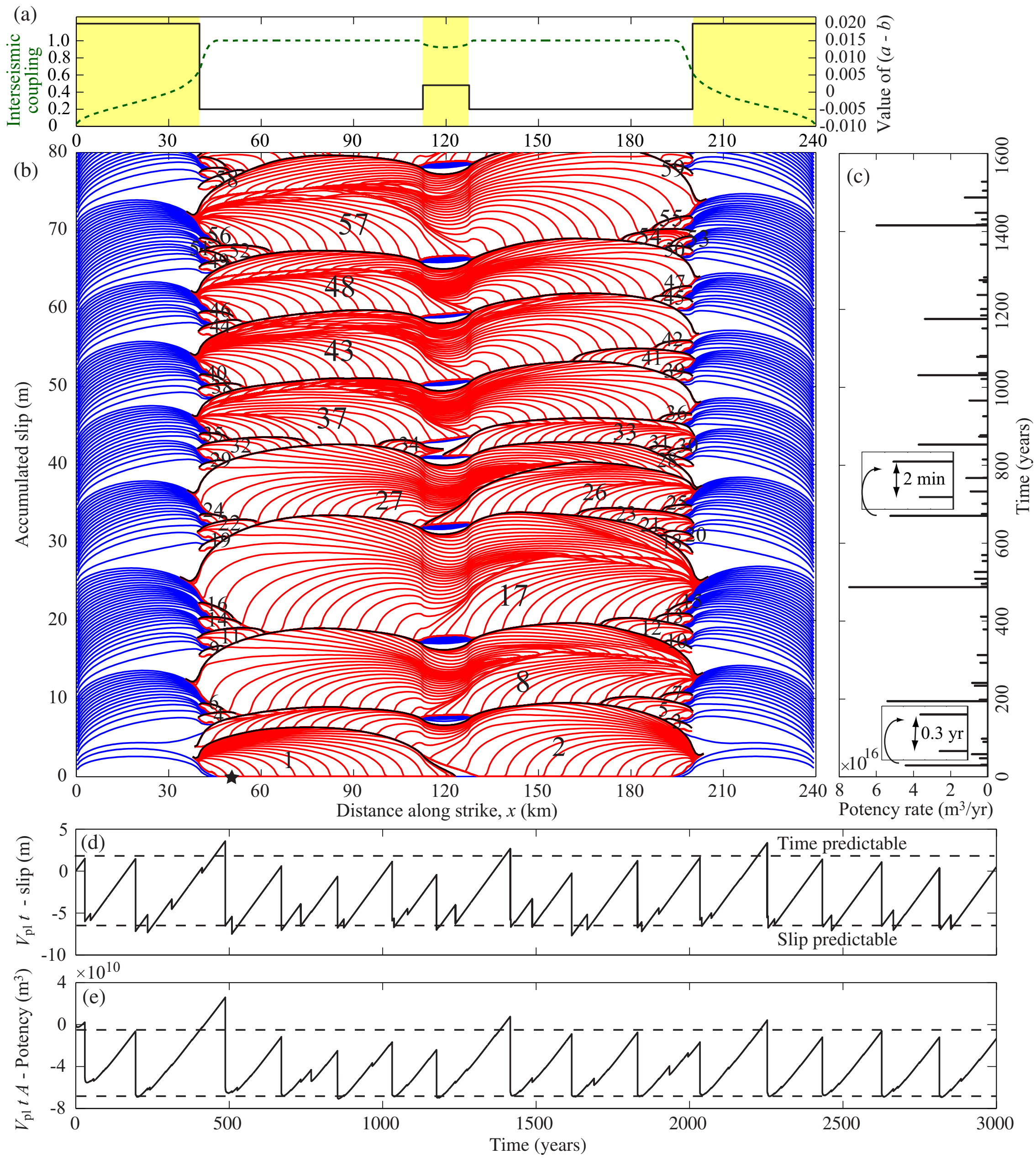

Figure 2.2: An example of the simulated long-term fault behavior. (a) The imposed spatial distribution of the friction parameter $(a - b)$ (black) and the simulated interseismic coupling (ISC). The computation of ISC is described in Appendix 2.8. (b) Contours of slip accumulated over 1600-year history. Red lines are intended to capture dynamic events and are plotted every 2 s during the simulated earthquakes, when $V_{\max} > 1$ cm/s. Blue lines display slip accumulation every 10 years. Slip accumulation after each earthquake is shown by black lines. Numbers indicate earthquakes in the order of their occurrence. (c) Potency rate over time, using the updip distance of 40 km. The insets depict successive events that occurred close in time. (d) Time dependence of slip deficit at the fault location x = 50 km indicated by a star in panel b. Dashed lines are approximate fits to the time- and slip-predictable models. (e) Potency deficit over the entire fault.

ical events and their relation to ISC on the Sunda megathrust. The VS regions of low ISC on both sides of the model act as permanent barriers to coseismic ruptures as observed in the south of the Mentawai Islands area or near the Batu Island area in Sumatra [*Chlieh et al.*, 2008]. Partial ruptures of a locked segment of subduction megathrust beneath the Mentawai islands [*Konca et al.*, 2008] may be explained by the presence of narrow VS barriers. After an event that ruptures only one of the VW segments, static stress transfers to the neighboring VW segment, leading to “clustering” of earthquakes; the two VW segments tend to rupture closer in time than their recurrence periods (Figure 2.2c). Negative stress drop (i.e., stress increase after an event) in the ruptured VS patch promotes propagation of the subsequent large earthquake through the patch. As a result, overlap of the slipped regions and the larger size of the subsequent event are indications of the presence of VS patches. These phenomena have been reported for the 700-year-long sequence of historical earthquakes beneath the Mentawai islands [*Sieh et al.*, 2008].

In the particular simulation of Figure 2.2, the system does not produce characteristic earthquakes. At a given point on the fault, the behavior obeys neither the slip-predictable nor the time-predictable model (Figure 2.2d). The behavior is closer to being slip predictable, even more so if one considers the average slip (or equivalently the slip potency) rather than the slip at one particular point (Figure 2.2e). A nearly slip-predictable behavior is not a surprising outcome given the chosen friction law, since, after each earthquake, the shear stress on the ruptured area drops to a value approximately determined by $\bar{\sigma}[f_{\mathrm{o}} + (a-b)\ln(V_{\mathrm{dyn}}/V_{\mathrm{o}})]$, where $\bar{\sigma}$ is the effective normal stress, f_0 is the reference friction coefficient corresponding to the reference slip rate V_0, and V_{dyn} is coseismic slip rate ($\sim$1-10 m/s). Also, the chosen friction law does not imply a threshold shear stress for earthquakes to nucleate so that it does not favor a time-predictable behavior. The simulation also shows that assessing a time- or slip-predictable behavior requires an extended history and is difficult with just a few earthquake cycles.

2.3 Characteristics of individual earthquakes

The rupture extent in individual earthquakes is determined by two kinds of barriers: lower prestress resulting from slip in previous events or the VS patches. In the case of low prestress close to the hypocenter, only relatively small events can develop (Figure 2.3a,d). Some events rupture the entire VW segment in which they have nucleated but arrest at the central VS patch, where the stress drop is negative (Figure 2.3b,e). For a given size and $\bar{\sigma}(a-b)$ of the VS patch, the overall prestress in the VW segments generally determines whether the two locked segments rupture together or independently. For example, in the case (c),(f) of Figure 2.3, the average prestress over the VW segment where the rupture starts is higher ($\tau = f_0\bar{\sigma} - 0.1$ MPa) than in the case (b),(e) of Figure 2.3 (where $\tau = f_0\bar{\sigma} - 0.9$ MPa). As a result, the rupture propagates through the central VS patch in the former case but not in the latter case. The distribution of prestress is spatially heterogeneous for all cases because the arrests of previous earthquakes and rheological boundaries create local stress concentrations. Static stress drops of the simulated earthquakes are in the range (1-10 MPa) typical for natural earthquakes (Figure 2.3g). The distribution of magnitudes has a gap between 7.8 and 8, which corresponds to the difference in magnitudes between the earthquakes confined to one VW segment and those rupturing across the central VS patch.

2.4 Quantifying the influence of a velocity-strengthening (VS) patch on interseismic coupling and the rupture pattern

Whether a VS patch can stop the propagation of seismic rupture depends on both the amount of stress that is supplied to the patch by the incoming rupture and the amount of stress increase needed for the patch to sustains seismic slip. Here, we show that the behavior of the model, in terms of the percentage of ruptures that propagate through the VS patch, can be described by a single non-dimensional parameter that incorporates the ratio of these stresses and hence includes properties of both the VS and VW parts of the fault.

In Figure 2.4, we represent the effect of the size D and VS parameter $(a-b)$ of the central VS patch on the seismic rupture pattern and ISC (averaged over the patch). The effect on seismic rupture patterns is quantified by the ratio of earthquakes that rupture both VS segments (and thereby propagate through the VS patch) to earthquakes that rupture at least one of the VW segments. We find that the percentage of the two-segment ruptures and ISC are well characterized by the following non-dimensional parameter:

$$B = \left[(2\pi)^{1/2}\bar{\sigma}_{\mathrm{vs}}(a_{\mathrm{vs}} - b_{\mathrm{vs}})D\right] / \left(\mu_{\mathrm{vw}}\bar{\sigma}_{\mathrm{vw}}b_{\mathrm{vw}}L_{\mathrm{vw}}R\right)^{1/2} \ , \tag{2.1}$$

where a and b are rate and state constitutive parameters, R and D are the sizes of the

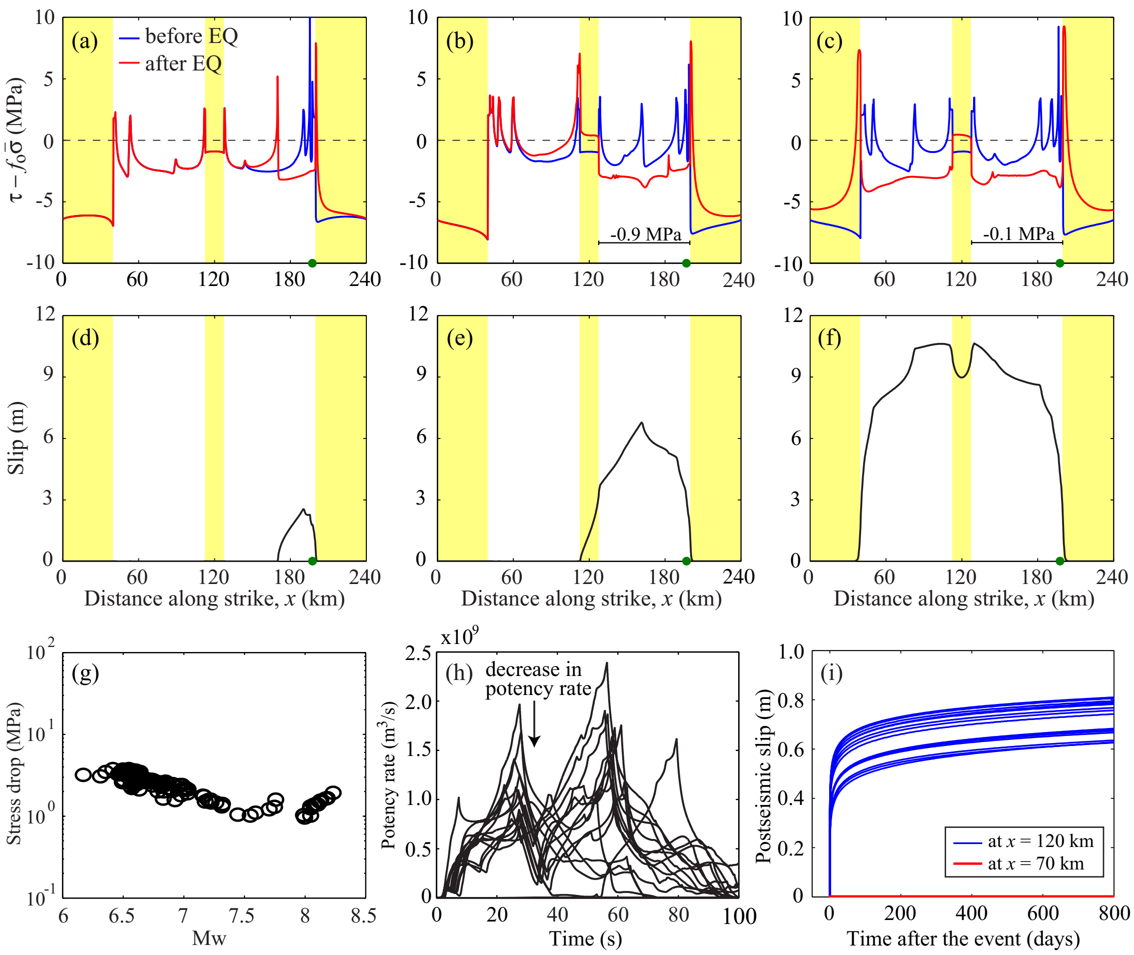

Figure 2.3: Characteristics of simulated earthquakes and postseismic slip. (a)-(f) Spatial distribution of shear stress and corresponding slip for three representative events of different sizes. Shear stress minus a reference value, $\tau - f_o\bar{\sigma}$, before and after each earthquake is shown. We define the beginning of an earthquake as the time when maximum slip rate $V_{\max}$ reaches 1 cm/s, and the end as the time when $V_{\max} < 1$ cm/s. Epicenters are marked by green dots. Average levels of the prestress over the VW region are indicated in panels (b) and (c). (g) Stress drops of all the events in 3000-year history. (h) Potency rates of events that reach the central VS patch and continue their propagation on the other side of the patch. The VS patch causes a marked decrease in potency rate. (i) Postseismic slip of the same events as in panel (h). A point within the VS patch (x = 120 km) and the VW region (x = 70 km) are compared.

VW segment and the VS patch, respectively, $\bar{\sigma}$ is the effective normal stress, μ is shear modulus, L is the characteristic slip, and the subscripts ’vs’ and ’vw’ are used to denote quantities related to the VS patch and VW segment, respectively. The derivation of the parameter is shown in Appendix 2.9. The curves of constant B in Figure 2.4 approximately follow the constant percentages of two-segment ruptures indicated by the color scale. When $B \gtrsim 4$, the patch acts as a permanent barrier, in the sense that no seismic rupture propagates through the patch over the simulated 3000-year history. When $B \lesssim 1$, the patch acts as an intermittent barrier (i.e., more than 50i% of one-segment ruptures propagate through the patch). For $B \lesssim 0.2$, 90% of rutpures that reach the patch propagate through. When the patch acts as a permanent barrier, the resulting earthquakes are approximately confined within each VW segment (Figure 2.4C1; Figure 2.5C1) and are more ’characteristic’ in their sizes, whereas a VS patch with $B \lesssim 4$ leads to greater variability of event sizes by allowing larger events to occur (Figure 2.4C2,C3; Figure 2.5C2).

In the case of the VS patch with $B \gtrsim 4$, earthquakes still occur irregularly (Figure 2.5C1), since the length R of each VW segment is much larger than the nucleation size h^*_{RA}. When $R \lesssim 3h^*_{\mathrm{RA}}$, there would be quasi-periodic repetition of ’characteristic’ earthquakes with similar rupture extent and moment, whereas, for $R \gtrsim 3h^*_{\mathrm{RA}}$, more complex behavior arises due to emergence of smaller earthquakes at the VW-VS transitions. In this study, we only consider the cases with VW segments much larger than the nucleation sizes ($R \gg 3h^*_{\mathrm{RA}}$), with the typical values of h^*_{RA} and R of the order of 2 km and 70 km, respectively.

The non-dimensional parameter B derived for explaining the coseismic rupture patterns

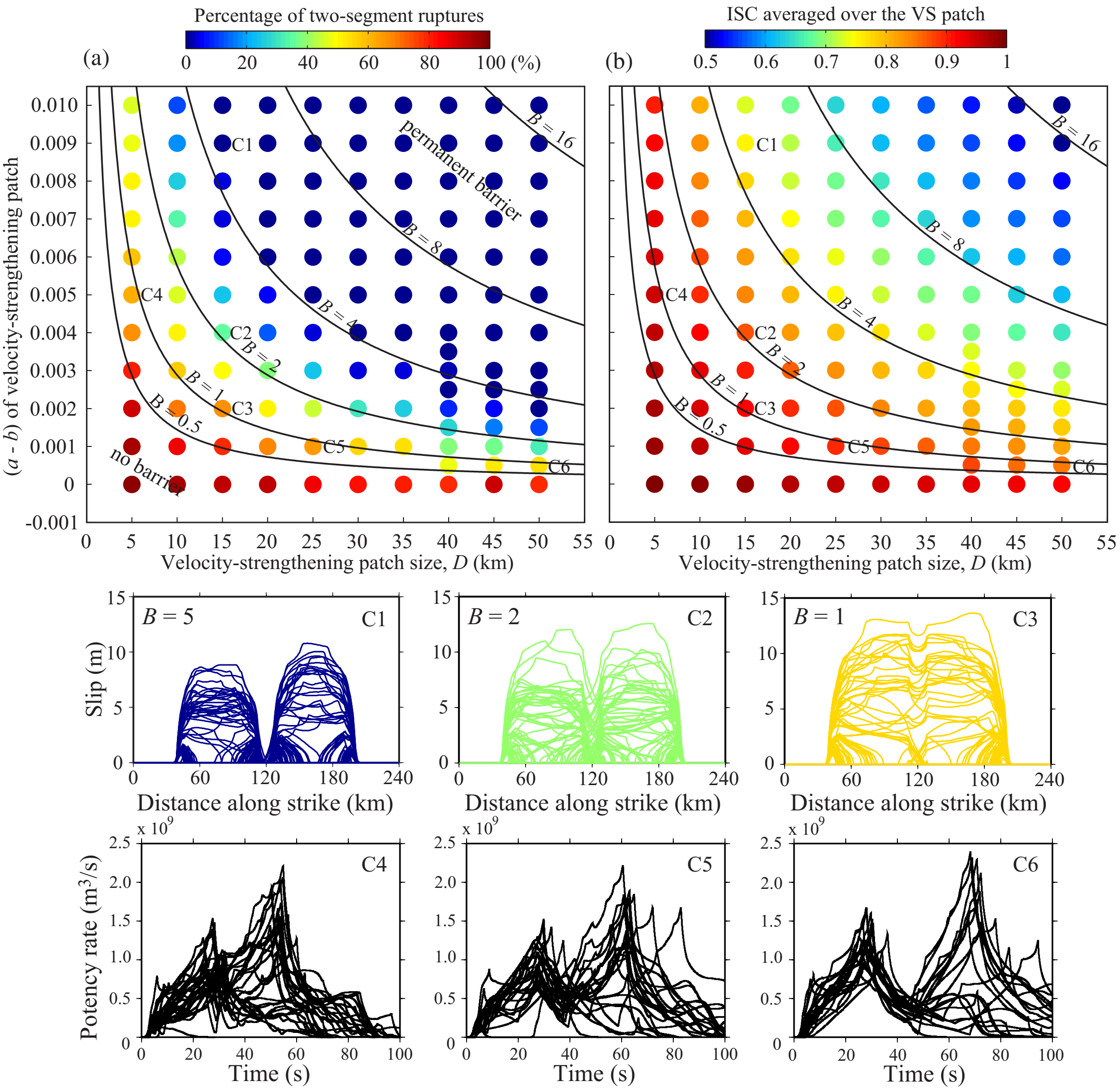

Figure 2.4: Phase diagrams that illustrate the effect of the central velocity-strengthening patch on the long-term behavior of the model. (a) Each dot represents a simulation of more than 3000 years of fault slip with the parameters of the patch given by the diagram axes. For different patch sizes D, the model size is adjusted so that the size R of each velocity-weakening segment is the same for all cases. Colors indicate the percentage P of events that rupture one of VW segments and continue their propagation on the other side of the VS patch (P = 0% is a permanent barrier, i.e. no ruptures that reach the patch propagate to the other side). Curves represent the function $(a_{\rm vs} - b_{\rm vs}) = B\left(\mu_{\rm vw}\bar{\sigma}_{\rm vw}b_{\rm vw}L_{\rm vw}R\right)^{1/2}/[(2\pi)^{1/2}\bar{\sigma}_{\rm vs}D]$, with the number on each curve corresponding to the value of B. (b) Simulated ISC averaged over the VS patch in the same set of simulations as in panel (a). Panels C1-C3 show slip distributions of events corresponding to Cases C1-C3 indicated in the diagram (a). Potency rates of all the events that propagated through the patch for Cases C4-C6 are shown in panels C4-C6.

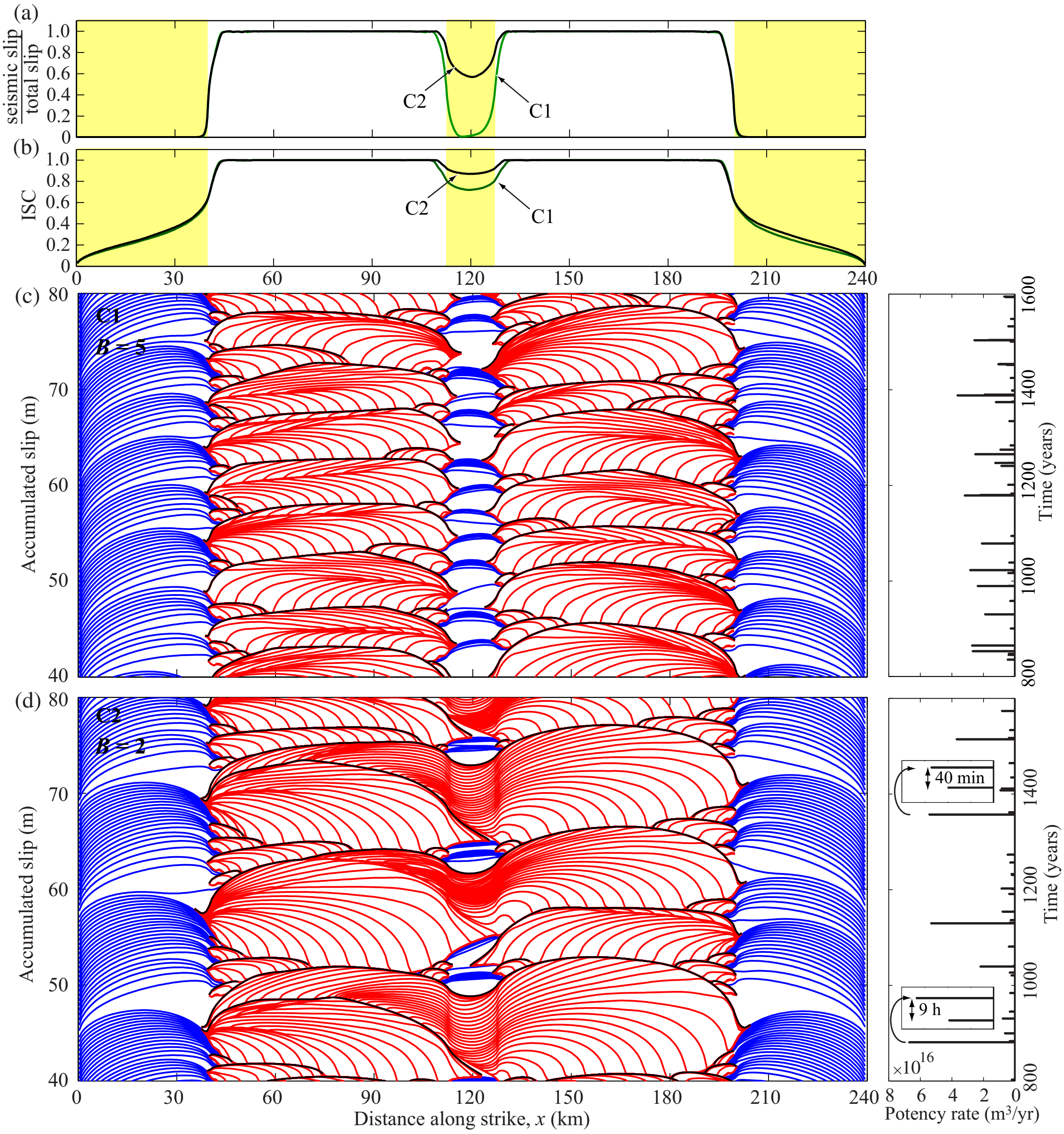

Figure 2.5: Examples of simulated long-term fault behavior. (a) The ratio of seismic slip to total slip for Cases C1 (green) and C2 (black) in Figure 4. (b) Simulated ISC for Cases C1 (green) and C2 (black). (c) Contours of slip accumulated over 800-year history and potency rate for Case C1. Lines have the same meaning as in Figure 2b. (d) Contours of slip accumulated over 800-year history and potency rate for Case C2.

can also capture the behavior of ISC over the VS patch (Figure 2.4b), where larger values of B correspond to smaller values of ISC over the patch. Since accumulated slip at a given time is relatively uniform over the fault domain and equals the sum of co-, inter-, and postseismic slip, it is not surprising that seismic behavior is related to the interseismic slip and hence to the values of ISC. We find that a patch with only slightly reduced ISC (ISC $\approx$ 0.75) can systematically arrest coseismic ruptures (Figure 2.4b and Figure 2.5c). This means that most of the total slip at the VS patch occurs postseismically (Figure 2.5c). The presence of a permanent barrier with relatively high values of ISC (ISC $\approx$ 0.75) corresponds to small percentages of co- and interseismic slip compared to that of afterslip.

The examples of Figures 2.4-2.5 and additional cases in Appendix 2.10 show that the parameter B is a good predictor of the model behavior over a wide range of parameters. Hence one can evaluate the values of B on faults in different tectonic settings based on observations of seismic and aseismic slip. Doing so would enable us to constrain the parameters of fault friction.

2.5 Conclusions

This study illustrates how heterogeneities of fault rheological properties can affect individual ruptures, earthquake sequences, and the pattern of ISC. The model described here is able to reproduce a wide range of behaviors observed on natural faults. In particular, our model is capable of explaining the complex sequence of recent and historical events, and their relation to ISC, on the Sunda megathrust. Our results show that areas of relatively high values of ISC ($\approx$0.75) can act as permanent barriers to coseismic ruptures. Areas of lower ISC on natural faults may limit the rupture extent of large earthquakes, with important implications for seismic hazard. Our study suggests that VS barriers may be the primary cause for the relative persistence of seismic rupture segmentation and asperities observed in some tectonic settings.

We find that the probability that an earthquake breaks through the velocity-strengthening patch can be quantified by a non-dimensional parameter B that depends on friction properties and sizes of both the velocity-strengthening patch and velocity-weakening regions. Parameter B also characterizes the effect of the variation in friction properties on interseismic coupling, which can be observed from geodetic or remote-sensing measurements. Patches with higher values of B result in locally lower interseismic coupling and act as permanent barriers to seismic rupture. Patches with a range of lower values of B lead to a more subtle effect on interseismic coupling, decreasing it from 1 to values between 0.75 and 0.95, but such patches can have a profound effect on the pattern of seismic ruptures, resulting in complex sequences of large earthquakes with quite different rupture area and amount of slip in successive seismic ruptures.

Our results indicate that the presence of a VS patch can be identified from the rupture kinematics of individual earthquakes and the distribution of afterslip. The source-time functions of earthquakes that rupture through the VS patch contain double peaks (Figure 2.4C4-C6). This is because both the potency rate and the rupture velocity first decrease as rupture propagates through the central VS patch and then increase after the rupture front enters the neighboring VW segment. Once the rupture velocity history of an earthquake is obtained from slip inversions, the patch size can be estimated from the duration of decreased potency rates between two peaks. A double peaked source-time function could also arise due to a region of lower prestress on a VW fault (sometimes referred to as an ’antiasperity’). However, the two types of heterogeneities can be distinguished using post-seismic observations, since afterslip would occur within a VS barrier (Figure 2.3i), but not within a VW region of lower prestress. Thus, variations in seismic potency rates combined with the distribution of afterslip can be used to infer smaller-scale heterogeneities in friction properties within a locked region of high ISC, where relatively small VS patches could have a profound effect on the long-term seismic behavior but a subtle effect on ISC, as is the case in a number of simulations presented here.

2.6 Appendix: Description of the fault model and parameters

Our fault model is based on a 2D antiplane (Mode III) framework and contains variations in steady-state friction properties. The fault motion is in the along-dip direction, and only variations with along-strike direction x are considered, so that the fault behavior is described by dip-parallel slip $\delta(x,t)$, slip rate $V(x,t) = \partial\delta(x,t)/\partial t$, and the relevant component of shear stress $\tau(x,t)$. The relation between slip $\delta(x,t)$, slip velocity $V(x,t)$, and the corresponding shear stress $\tau(x,t)$ is given by:

$$\tau(x,t) \;=\; \tau^{o}(x) + f(x,t) - \frac{\mu}{2c_s}V(x,t)\ , \tag{2.2}$$

where μ is the shear modulus, c_s is the shear wave speed, τ^o is the loading stress that would act on the interface if it were constrained against any slip, and $f(x,t)$ is a linear functional of prior slip over the causality cone [*Rice*, 1993; *Lapusta et al.*, 2000]. The last term, known as radiation damping, is extracted from the functional $f(x,t)$ so that $f(x,t)$ can be evaluated without concern for singularities. The details of elastodynamics and simulation methodology for the model are described in *Lapusta et al.* [2000].

Earthquakes are simulated as a part of spontaneously occurring earthquake sequences on a fault that is subjected to slow, tectonic-like loading. This approach allows us to study naturally developing earthquakes in our models, with conditions before the nucleation originating from the previous stages of earthquake occurrence rather than from arbitrarily selected prestress. Our simulations resolve all stages of each earthquake episode: the aseismic nucleation process in gradually varying zones of accelerating slip, the subsequent inertially controlled event (unstable slip) with realistic slip rates and rupture speeds, the postseismic slip, and the interseismic quasi-static deformation between events.

The fault is governed by rate and state friction with the aging form of state variable evolution. For situations with time-independent effective normal stress $\bar{\sigma}$, the shear strength τ is expressed as

$$\tau = \bar{\sigma}\left[f_0 + a\ln\left(\frac{V}{V_0}\right) + b\ln\left(\frac{V_0\theta}{L}\right)\right] , \tag{2.3}$$

$$\frac{d\theta}{dt} = 1 - \frac{V\theta}{L} , \tag{2.4}$$

where $a > 0$ and b are rate and state constitutive parameters, V is slip rate, f_0 is the reference friction coefficient corresponding to the reference slip rate V_0, θ is a state variable which can be interpreted as the average age of the population of contacts between two surfaces, and L is the characteristic slip for state evolution [e.g., *Dieterich*, 1978, 1979; *Rice and Ruina*, 1983; *Ruina*, 1983; *Dieterich and Kilgore*, 1994]. The actual fault resistance to sliding in our model is given by rate and state friction regularized at zero slip velocity [e.g., *Lapusta et al.*, 2000].

We use parameters applicable for natural faults or derived from laboratory experiments except for characteristic slip L. The value of L used is 8 mm, larger than the laboratory values of the order of 1-100 μm, to make large-scale simulations numerically tractable. Unless otherwise noted, we use μ = 30 GPa, c_s = 3.3 km/s, $\bar{\sigma}$ = 50 MPa, f_0 = 0.6, $V_0 = 10^{-6}$ m/s, $a_{\mathrm{vw}} = 0.010$, and $b_{\mathrm{vw}} = 0.015$, where the subscript 'vw' is used to denote quantities related to the VW segments.

2.7 Appendix: Criteria for spatial discretization and time-stepping parameters

The simulated fault domain $\lambda = 480$ km is composed of the 240-km region where friction is applied, and the 240-km loading region of the prescribed slip rate. In our numerical simulations, the spatial cell size Δx needs to be small enough to properly resolve both the aseismic nucleation process and the cohesive zone size during dynamic rupture propagation. In all of our simulations, good resolution of the cohesive-zone size is a more strict constraint on the spatial discretization. The ratio $\Lambda/\Delta x$ of the cohesive zone size Λ to the cell size $\Delta x = 29$ m needs to be 3-5 or larger for faults with rate and state friction [*Kaneko* *et al.*, 2008]. The value of Λ in a typical scenario is ≈ 200 m and hence $\Lambda/\Delta x > 5$. The resulting ratio $h^*_{\mathrm{RA}}/\Delta x = 2\mu b L/[\pi(b-a)^2\bar{\sigma}\Delta x] = 63$, where h^*_{RA} is the estimate of the nucleation size for $a/b \gtrsim 0.5$ given by *Rubin and Ampuero* [2005], is high enough to properly resolve the nucleation processes.

Time t is discretized into variable time steps. The minimum value of the time step is related to the time $\Delta t_{\mathrm{cell}} = \Delta x/c_s$ needed for the shear wave to propagate through one spatial cell; it is given by $0.5\Delta x/c_s = 0.044$ s. Such a small value of Δt_{min} is needed because slip in one time step must be comparable to or smaller than the characteristic slip L of the friction law to resolve the state-variable evolution. The largest time step allowed in all simulations is 0.2 years. In the mode-dependent convolution truncation, $T_w(1) = \lambda/c_s$ and $q_w = 4$. A typical simulation with 3000 years of simulated slip history takes 5 days on a single 2.33-GHz processor.

2.8 Appendix: Definition of interseismic coupling (ISC)

We consider interseismic periods at each point on the fault to correspond to the time periods when $V(x,t) < V_{\mathrm{pl}}$, where V_{pl} is the plate rate. Such periods are illustrated in Figure 2.6. For the interseismic periods, spatially and temporally variable ISC can be defined as $1 - V(x,t)/V_{\mathrm{pl}}$. To report a temporally averaged value of ISC for each fault location x, we compute:

$$\mathrm{ISC}(x) = 1 - \delta^{\mathrm{cum}}_{\mathrm{int}}(x)/[V_{\mathrm{pl}} T^{\mathrm{cum}}_{\mathrm{int}}(x)] \ , \tag{2.5}$$

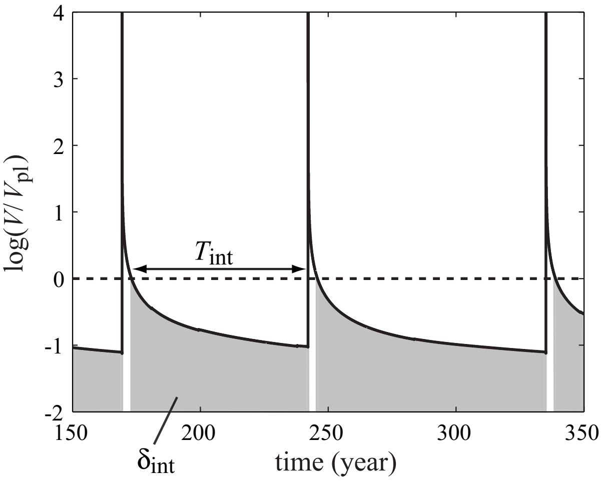

Figure 2.6: Illustration of interseismic periods in our simulations. Slip velocity V at the center of the VS patch is shown for one of the simulations. $T_{\rm int}$ and $\delta_{\rm int}$ are the duration and slip, respectively, during one of the interseismic periods, defined as the time periods with $V(x,t) < V_{\rm pl}$. To compute a temporally averaged ISC, we use the sum of $T_{\rm int}$ and $\delta_{\rm int}$ for all interseismic periods in formula (2.5).

where $T_{\rm int}^{\rm cum}$ is sum of the interseismic time intervals at the location x for the entire simulation and $\delta_{\rm int}^{\rm cum}$ is the slip accumulated at x over all interseismic periods.

2.9 Appendix: Derivation of the non-dimensional model parameter *B*

The behavior of the model in terms of the percentage of ruptures that propagate through the VS patch (Figure 2.4) can be described by a single non-dimensional parameter that incorporates properties of both VS and VW parts of the fault. Let us consider the condition under which a single seismic rupture that has reached the VS patch would propagate through the patch. During fast seismic slip, shear stress at the VS patch would go up, which means that the patch requires additional shear stress $\Delta\tau_{\rm seis}$ over its entire length D to sustain seismic slip. The rupture that has reached the VS patch increases shear stress at the patch due to stress concentration in front of the rupture; if that stress increase is adequate, the rupture would propagate through the patch. Hence we define the non-dimensional parameter as

$$B = \frac{\Delta\tau_{\mathrm{seis}} D}{\Delta T} \ , \tag{2.6}$$

where ΔT is the stress increase on the patch due to the rupture of the nearby VW segment integrated through the patch. We would expect the rupture to always propagate through the patch if $B \leq 1$. If $B > 1$, the rupture may still propagate through the patch after combined stress deposition due to several earthquakes, unless the stresses are released in the postseismic and interseismic periods. Hence for $B > 1$, we expect smaller percentage of earthquakes to propagate through the patch.

Let us estimate $\Delta\tau_{\mathrm{seis}}$. Prior to the arrival of coseismic rupture, the shear stress inside the patch is given by:

$$\tau_{\mathrm{vs}}^{\mathrm{i}} = \bar{\sigma}_{\mathrm{vs}} \left[f_0 + (a_{\mathrm{vs}} - b_{\mathrm{vs}}) \ln \left(V_{\mathrm{vs}}^{\mathrm{bg}} / V_0 \right) \right] \ , \tag{2.7}$$

where $V_{\mathrm{vs}}^{\mathrm{bg}}$ is the interseismic slip rate in the VS patch. During seismic slip with slip rate $V_{\mathrm{vs}}^{\mathrm{dyn}}$, shear stress in the patch can be approximated as

$$\tau_{\mathrm{vs}}^{\mathrm{d}} = \bar{\sigma}_{\mathrm{vs}} \left[f_0 + (a_{\mathrm{vs}} - b_{\mathrm{vs}}) \ln \left(V_{\mathrm{vs}}^{\mathrm{dyn}} / V_0 \right) \right] \ . \tag{2.8}$$

Hence

$$\Delta\tau_{\rm seis}D = \bar{\sigma}_{\rm vs}(a_{\rm vs} - b_{\rm vs})D \ln\left(V_{\rm vs}^{\rm dyn}/V_{\rm vs}^{\rm bg}\right) \ . \tag{2.9}$$

Now let us consider ΔT. From (2.2), shear stress distribution $\tau(x)$ during a seismic event can be written as

$$\tau(x) \ = \ \tau^{\rm before}(x) + f(x,t) - \frac{\mu}{2c_s}V(x) \ , \tag{2.10}$$

where $\tau^o(x)$ in (2.2) is taken to be shear stress before the event and $f(x,t)$ is redefined accordingly. Integrating (2.10) over the entire fault, we have

$$\int_x \tau(x)dx \ = \ \int_x \tau^{\rm before}(x)dx - \frac{\mu}{2c_s}\int_x V(x)dx \ , \tag{2.11}$$

since the integral over $f(x,t)$ is zero [*Zheng and Rice*, 1998]. The last term on the right-hand side is small compared to others, since slip velocity is appreciable only in relatively small regions next to the crack tips. Ignoring that term, we obtain

$$\int_x \left[\tau(x) - \tau^{\rm before}(x)\right] dx = 0 \ , \tag{2.12}$$

or

$$\int_{\rm vw} \left[\tau(x) - \tau^{\rm before}(x)\right] dx + \int_{\rm vs} \left[\tau(x) - \tau^{\rm before}(x)\right] dx = 0 \ . \tag{2.13}$$

Considering the situation where one of the VW segments has ruptured and transferred stress onto the surrounding VS regions, we get:

$$\Delta T = (1/2)\int_0^R \Delta\tau_{\mathrm{vw}}(x)dx = \overline{\Delta\tau_{\mathrm{vw}}}R/2 \ , \tag{2.14}$$

where $\Delta\tau_{\mathrm{vw}}$ and $\overline{\Delta\tau_{\mathrm{vw}}}$ are the coseismic stress drop and its average value over the velocity weakening segment, respectively. Equation (2.14) assumes that half of the shear stress is transferred to the central VS patch (with the other half being deposited onto the larger VS region on the other side of the ruptured segment) and that the velocity-strengthening patch is large enough to host most of stress concentration due to rupture.

To obtain an analytical expression for the average stress drop $\overline{\Delta\tau_{\mathrm{vw}}}$, we use the model of the Mode III quasi-static 2D shear crack with uniform prestress in an infinite elastic medium. The energy release rate $G = K_{III}^2/(2\mu_{\mathrm{vw}})$, where $K_{III} = \overline{\Delta\tau_{\mathrm{vw}}}\sqrt{\pi R/2}$ [e.g., *Broberg*, 1999], is balanced by the fracture energy G_c, giving

$$\overline{\Delta\tau_{\mathrm{vw}}} = \left(\frac{4\mu_{\mathrm{vw}}G_c}{\pi R}\right)^{1/2} . \tag{2.15}$$

For the rate and state friction with the aging form of state variable evolution as used in this work, the fracture energy G_c is given by *Rubin and Ampuero* [2005]

$$G_c = \frac{\bar{\sigma}_{\mathrm{vw}}b_{\mathrm{vw}}L_{\mathrm{vw}}}{2}\left[\ln(V_{\mathrm{vw}}^{\mathrm{dyn}}/V_{\mathrm{vw}}^{\mathrm{bg}})\right]^2 \ . \tag{2.16}$$

Then (2.15) becomes

$$\overline{\Delta\tau_{\mathrm{vw}}} = \left(\frac{2\mu_{\mathrm{vw}}\bar{\sigma}_{\mathrm{vw}}b_{\mathrm{vw}}L_{\mathrm{vw}}}{\pi R}\right)^{1/2}\ln(V_{\mathrm{vw}}^{\mathrm{dyn}}/V_{\mathrm{vw}}^{\mathrm{bg}}) \ . \tag{2.17}$$

Substituting the obtained estimates into (2.6), we obtain

$$B = \frac{(2\pi)^{1/2}\bar{\sigma}_{\rm vs}(a_{\rm vs}-b_{\rm vs})D\ln\left(V_{\rm vs}^{\rm dyn}/V_{\rm vs}^{\rm bg}\right)}{(\mu_{\rm vw}\bar{\sigma}_{\rm vw}b_{\rm vw}L_{\rm vw}R)^{1/2}\ln\left(V_{\rm vw}^{\rm dyn}/V_{\rm vw}^{\rm bg}\right)} \approx \frac{(2\pi)^{1/2}\bar{\sigma}_{\rm vs}(a_{\rm vs}-b_{\rm vs})D}{(\mu_{\rm vw}\bar{\sigma}_{\rm vw}b_{\rm vw}L_{\rm vw}R)^{1/2}}\,. \tag{2.18}$$

In our simulations, the factor $\ln\left(V_{\rm vs}^{\rm dyn}/V_{\rm vs}^{\rm bg}\right)/\ln\left(V_{\rm vw}^{\rm dyn}/V_{\rm vw}^{\rm bg}\right) \approx 0.7$, but we ignore this factor in (2.18) for simplicity. Figure 2.4 shows the correspondence between the simulated results and the parameter B for variations in the size and friction properties of the VS patch. Note that $B = 1$ corresponds to about 60% of ruptures propagating through the VS patch, not 100% as expected based on its definition, which is likely the result of the assumptions made in deriving B. However, the parameter is a good predictor of the model behavior, in the sense that the value of B predicts the percentage of ruptures that would propagate through as the model parameters are varied, as described in sections 2.4 and 2.10.

2.10 Appendix: Relation among the non-dimensional parameter *B*, the percentage of two-segment ruptures *P*, and interseismic coupling (ISC) over a range of parameters

To explore the usefulness of parameter B, we perform a series of simulations similar to the ones discussed in section 2.4 (Figure 2.4) but with variations in several parameters entering the expression (2.18). In each set of simulations, we change one model property from the case of Figure 2.4 and consider the influence of the size D and $(a-b)$ of the VS patch on

Table 2.1: The range of model parameters used to explore the correspondence between the non-dimensional parameter B and the model behavior (Figure 2.8).

Parameter	Symbol	Range
Shear modulus	μ	$30,\ 60$ GPa
Characteristic slip distance in vw	L_{vw}	$8,\ 24$ mm
Characteristic slip distance in vs	L_{vs}	$8,\ 24$ mm
Effective normal stress in vw	$\bar{\sigma}_{\text{vw}}$	$25,\ 50$ MPa
Effective normal stress in vs	$\bar{\sigma}_{\text{vs}}$	$25,\ 50$ MPa
The size of the vw segment	R	$30-100$ km
The size of the vs patch	D	$5-50$ km
Rate and state parameter a in vw	a_{vw}	$0.0025-0.025$
Rate and state parameter a in vs	a_{vs}	$0.010-0.020$
Rate and state parameter b in vw	b_{vw}	$0.0050-0.030$
Rate and state parameter b in vs	b_{vs}	$0-0.020$

percentage of two-segment ruptures. We find that the curves of constant B approximately correspond to the same color range in all cases we consider (e.g., in Figure 2.7, the curves with $B = 2$ correspond to light green to dark green), suggesting that B is a good predictor of the percentage of two-segment ruptures in cases with different parameters considered here.

In Figure 2.8, we quantify the goodness of the correspondence between the non-dimensional parameter B and the behavior of the model for the simulations shown in Figure 2.4, Figure 2.7, and additional simulations with model parameters given in Table 2.1. We find that the relation between B and the percentage of two-segment ruptures P is non-linear and can be fitted with the following function:

$$\begin{aligned} P_{\text{est}} &= 100(4-B)/(4+B) \quad \text{for} \quad B \le 4 \\ &= 0 \quad\quad\quad\quad\quad\quad\quad\quad \text{for} \quad B > 4\ . \end{aligned} \tag{2.19}$$

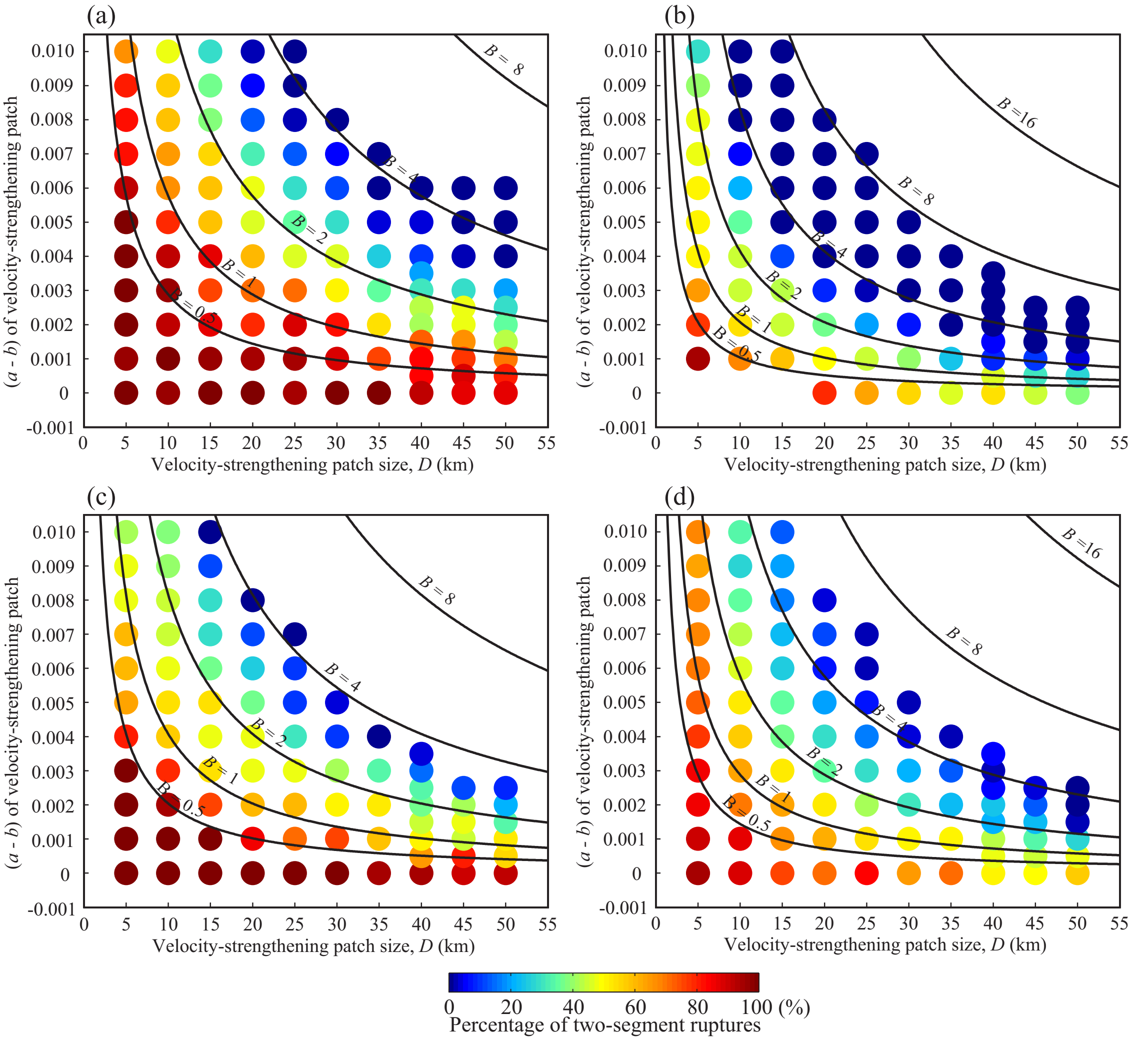

Figure 2.7: Phase diagrams similar to the one in Figure 2.4a, but for models with different parameters, to verify the usefulness of parameter B. The parameters in Figure 2.4 are $\bar{\sigma}_{\text{vw}}$ = $\bar{\sigma}_{\text{vs}}$ = 50 MPa, $a_{\text{vw}} = 0.010$, $b_{\text{vw}} = 0.015$, and R = 72.5 km. Panels (a)-(d) each show results for a set of simulations with one or two of these parameters modified. (a) Case with $\bar{\sigma}_{\text{vs}}$ = 25 MPa. (b) Case with R = 32.5 km. (c) Case with $a_{\text{vw}} = 0.025$ and $b_{\text{vw}} = 0.030$. (d) Case with $a_{\text{vw}} = 0.005$ and $b_{\text{vw}} = 0.015$.

where P_{est} would be the value of P estimated based on B. The value $B = 4$ corresponds to $P = 0$% (a permanent barrier). We also find that the empirical relation between B and the simulated ISC averaged over the patch is non-linear and given by

$$\text{ISC}_{\text{est}} = 1 - 0.085B^{0.62} \ , \tag{2.20}$$

where ISC_{est} would be the value of ISC estimated based on B. Combining (2.19) and (2.20), and rewriting P as a function of ISC, we obtain

$$\begin{aligned} P &= 100 \left[\frac{4 - \left(\frac{1-\text{ISC}}{0.085}\right)^{1/0.62}}{4 + \left(\frac{1-\text{ISC}}{0.085}\right)^{1/0.62}} \right] \quad \text{for} \quad \text{ISC} \geq 0.8 \\ &= 0 \qquad\qquad\qquad\qquad\qquad\quad \text{for} \ \ \text{ISC} < 0.8 \ . \end{aligned} \tag{2.21}$$

As expected, the relation between the percentage of two-segment ruptures P and ISC can be well approximated by (2.21) (Figure 2.8e). Note that a patch with only slightly reduced ISC (ISC $\approx$ 0.75) can systematically arrest coseismic ruptures.

We conclude that the non-dimensional parameter B is a good predictor of both coseismic and interseismic slip over a wide range of parameters.

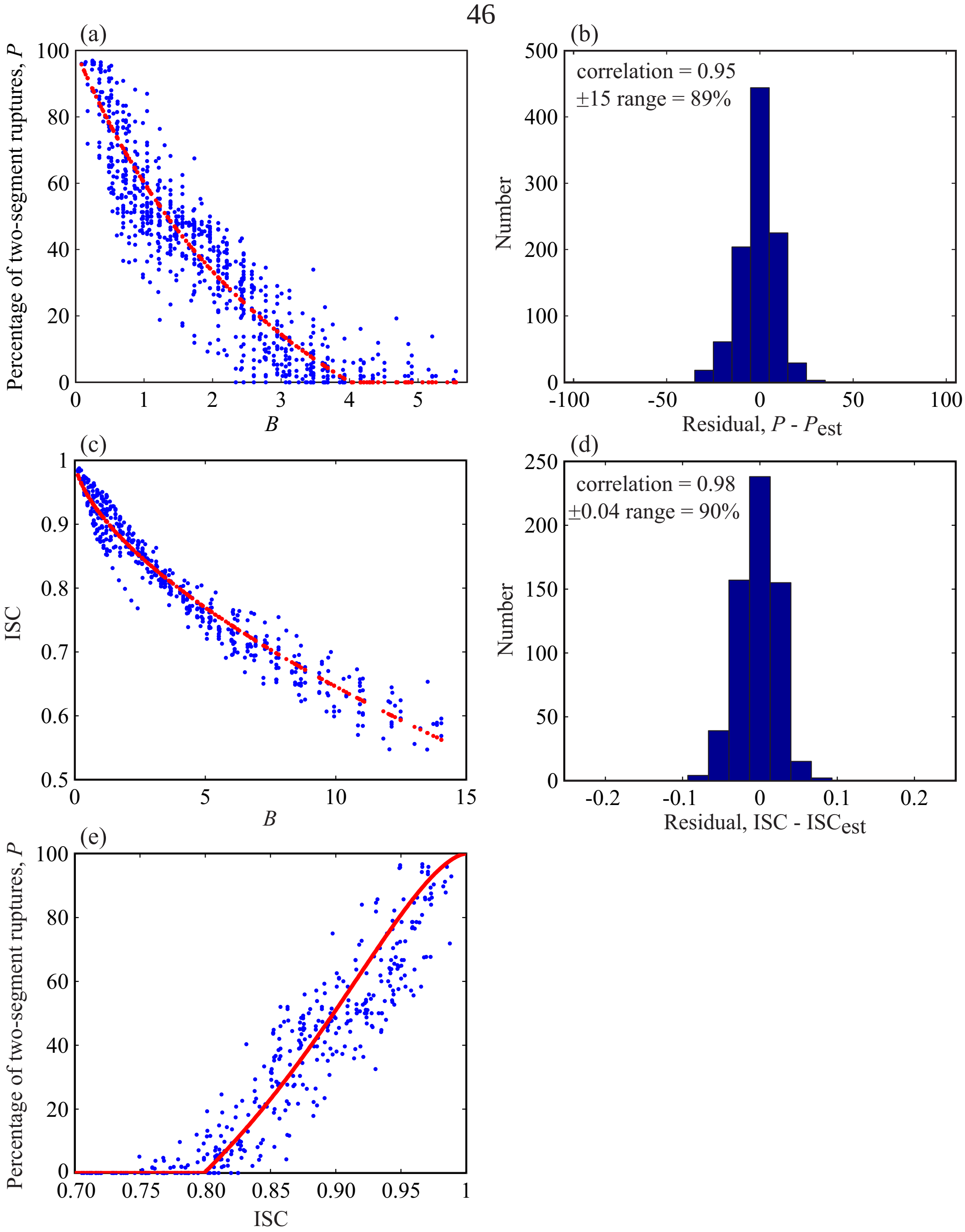

Figure 2.8: Relation between the non-dimensional parameter B and the percentage of two-segment ruptures P (panels a, b), and simulated ISC (panels c, d) over a range of parameters given by Table 2.1. (a) Each dot corresponds to simulated P with a different set of parameters. The red curve is a function $P = 100(4 - B)/(4 + B)$ for $B \leq 4$ and $P = 0$ for $B > 4$. Note that the set of parameters corresponding to velocity-neutral ($a_{\mathrm{vs}} = b_{\mathrm{vs}}$) cases are excluded. (b) A histogram that shows good agreement between the prediction and the simulated P. (c) Each dot corresponds to a simulated value of ISC averaged over the VS patch with a different set of model parameters. The red curve is a function ISC $= 1 - 0.085B^{0.62}$. (d) A histogram that shows good agreement between the prediction and the simulated ISC. (e) Relation between the percentage of two-segment ruptures P and simulated ISC of the VS patch. The red curve is the prediction based on formula (2.21).

Chapter 3

Variability of Earthquake Nucleation in Continuum Models of Rate and State Faults

In this Chapter, we simulate, in the context of earthquake sequences, several plausible scenarios of earthquake nucleation on faults embedded in an elastic medium and governed by rate and state friction, and explore variability in simulated earthquake nucleation due to fault heterogeneities and different loading conditions.

This Chapter is based on Sections 2-4 of the paper “Variability of earthquake nucleation in continuum models of rate-and-state faults and implications for aftershock rates” by Y. Kaneko and N. Lapusta (*J. Geophys. Res.*, 2008).

3.1 Previous theoretical studies of earthquake nucleation

Studies of earthquake nucleation have concentrated on a theoretically interesting and practically important topic: the nucleation size, i.e., the size of the slipping zone right before an earthquake. Several theoretical estimates h_{nucl} of the nucleation size have been proposed, all of them in the form:

$$h_{\mathrm{nucl}} = \frac{\eta G L}{\bar{\sigma} F}, \tag{3.1}$$

where η is a model-dependent parameter of order one, G is the shear modulus, and F is a function of rate and state parameters a and b. *Rice and Ruina* [1983], *Ruina* [1983], and *Rice et al.* [2001] considered linear stability of perturbations from steady-state sliding and determined that $F = b - a$. *Dieterich* [1992] assumed that nucleation processes accelerate fast enough for $V\theta/L \gg 1$ to hold and obtained $F = b$. The estimate of *Dieterich* [1992] was later confirmed in meter-scale rock friction experiments [*Dieterich and Kilgore*, 1996]. *Rubin and Ampuero* [2005] proposed that there are two regimes controlled by the ratio a/b. If $a/b \lesssim 0.37$, the nucleation proceeds in a fixed region of the size given by (3.1) with $F = b$, as in the estimate by *Dieterich* [1992]. If $a/b \gtrsim 0.5$, the nucleation process resembles an expanding crack and the nucleation size asymptotically approaches (3.1) with $F = (b - a)^2/b$. Note that all three estimates match, within factors of order 1, for $a \ll b$ which implies $b - a \approx b$. For a approaching b (friction properties close to velocity neutral), both Rice-Ruina and Rubin-Ampuero estimates predict increasingly larger nucleation sizes (although Rubin-Ampuero estimate increases significantly faster). This is consistent with the fact that velocity-strengthening regions cannot spontaneously produce unstable sliding, and hence the nucleation size for $a \geq b$ can be considered infinite.

3.2 2D continuum models of earthquake nucleation

We consider earthquake nucleation on a planar fault embedded into an elastic medium of homogeneous elastic properties with the shear wave speed $c_s = 3.0$ km/s, shear modulus $G = 30$ GPa, and Poisson's ratio $\nu = 0.25$. On the fault, a potentially seismogenic patch borders regions steadily moving with a prescribed slip rate $V_{\mathrm{L}} = 1$ mm/yr, as illustrated in Figure 3.1A. That steady motion provides loading in our models. The loading slip rate $V_{\mathrm{L}} = 1$ mm/yr is on the low end of typical plate rates but it could be representative of steady slip achieved locally on faults, especially in the case of secondary faults or multiple fault strands. The fault resistance to sliding is given by rate and state friction regularized at zero slip velocity [*Rice and Ben-Zion*, 1996; *Lapusta et al.*, 2000]. The value of characteristic slip L in simulations presented in Chapters 3 and 4 is 80 μm (unless noted otherwise), as laboratory-like values of L (of order 1-100 μm) are required to account for the presence of small ($M \sim 0$) earthquakes on natural faults [e.g., *Lapusta and Rice*, 2003].

Two simplified fault models that we use to create two conceptually different scenarios of earthquake nucleation are described in sections 3.2.1-3.2.2 and illustrated in Figure 3.1B. More details are given in appendix 3.6. The friction and stress parameters of the models are summarized in Table 3.1 and Figure 3.2. To simulate spontaneous slip accumulation in terms of earthquake sequences, we use the boundary integral method developed by *Lapusta et al.* [2000] and *Lapusta* [2001].

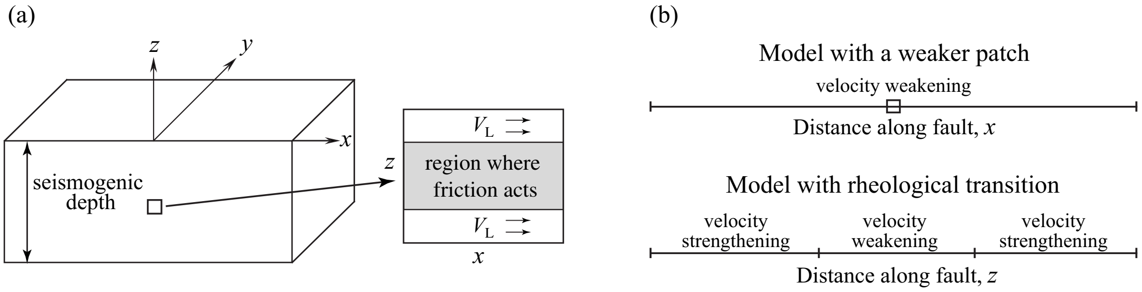

Figure 3.1: (A) 3D schematics of a planar fault in an elastic medium. This study employs simplified 2D models and focuses on a small region indicated by the square. The fault region governed by rate and state friction (shown in gray) is loaded by relative motion above and below the region with a prescribed slip rate V_{L}. (B) Schematics of fault properties in the simplified 2D continuum models. In the model with a weaker patch (top), the fault has steady-state velocity-weakening properties everywhere and contains a patch of lower effective normal stress indicated by a square. In the model with rheological transition (bottom), a steady-state velocity-weakening region is surrounded by steady-state velocity-strengthening regions.

Table 3.1: Friction-related parameters of both models. In the model with a weaker patch, $\bar{\sigma} = 50$ MPa in the patch and $\bar{\sigma} = 55.6$ MPa outside the patch. The indicated values of a and b are valid for the entire fault in the model with a weaker patch and for the part of the steady-state velocity-weakening region of the model with rheological transition where a and b are constant.

Parameter	Symbol	Value
Reference slip velocity	V_0	10^{-6} m/s
Reference friction coefficient	μ_0	0.6
Characteristic slip distance	L	80.0 μm
Effective normal stress	$\bar{\sigma}$	50.0 MPa
Rate and state parameter a	a	0.015 or 0.0015
Rate and state parameter b	b	0.019 or 0.0055

3.2.1 Model with a weaker patch

The first model incorporates a weaker patch of 10% lower effective normal stress. The model is based on the crustal-plane model [*Lapusta*, 2001]; it restricts the fault to motions parallel to the along-strike direction x, eliminates the fault depth by considering depth-averaged quantities, and retains variations only in the along-strike direction x. These modifications turn the 2D planar fault into a 1D along-strike analog (Figure 3.1B), with the fault behavior described by strike-parallel slip $\delta(x, t)$, slip velocity (or slip rate) $V(x, t) = \partial\delta(x, t)/\partial t$, and the relevant component of shear stress $\tau(x, t)$. Compressive effective normal stress $\bar{\sigma}(x)$ does not depend on time in the cases considered. At the ends of the fault, there are zones of zero initial shear stress to stop dynamic events (Figure 3.2). Hence the extent of the fault capable of sustaining dynamic events is 1000 m. A more physical approach would be to replace the zero-stress regions with regions of velocity-strengthening properties, but that would create alternative places for earthquakes to nucleate, and in this model we would like to avoid such complexities. By making earthquakes nucleate in the designated place, i.e., at the weaker patch in the middle of the fault, we can control how heterogeneous the imposed conditions are in the nucleation region.

We have done a number of simulations of earthquake sequences in this model, varying the values of parameters a (0.0015-0.015), b (0.0055-0.019), L (10-120 $\mu\mathrm{m}$), and the size of the weaker patch (2-200 m). We present results for three representative cases, all with $L = 80\ \mu\mathrm{m}$:

Case 1: The size of the weaker patch, 100 m, is much larger than the nucleation size, which is less than 30 m in this case. Hence there is no imposed heterogeneity within the

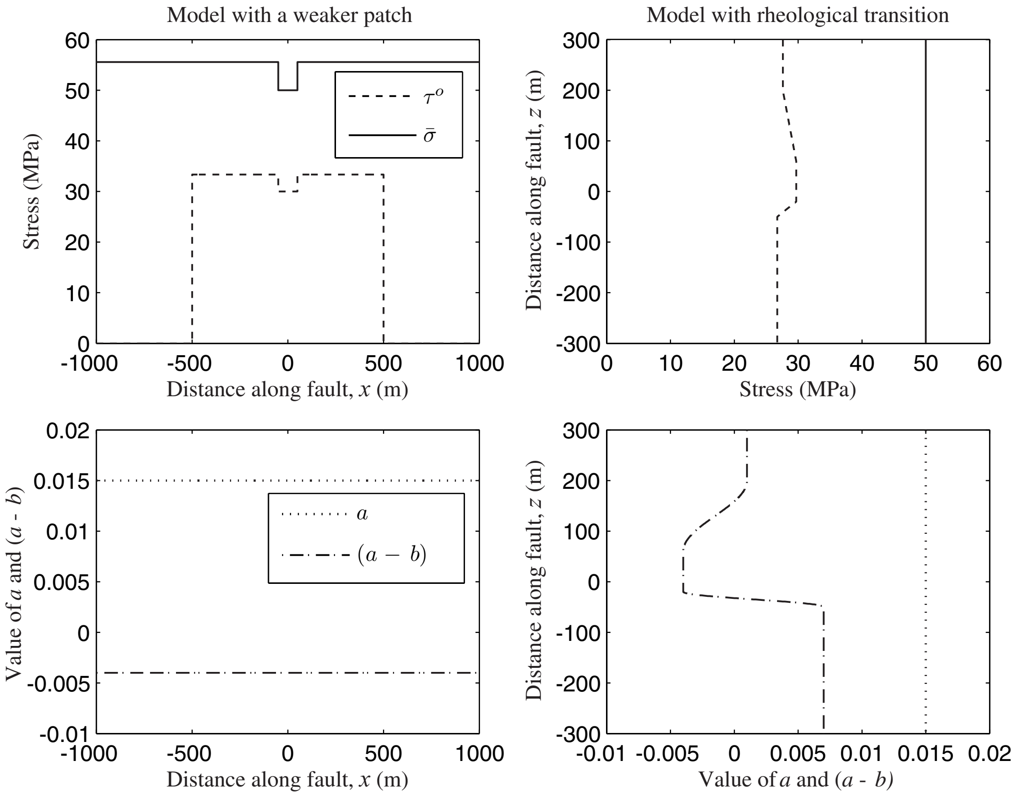

Figure 3.2: Top panels: Distributions of effective normal stress $\bar{\sigma}$ and initial shear stress τ^o in the two models. In the model with a weaker patch, the region of lower $\bar{\sigma}$ is introduced in the middle of the fault to encourage earthquake nucleation there. The size of the weaker region varies in different cases studied. Bottom panels: Examples of distributions of rate and state parameters a and $(a - b)$ in the two models. Locations with $a - b = 0$ correspond to rheological transitions from velocity-weakening to velocity-strengthening steady-state friction. We vary a and b in the presented cases but keep $(a - b)$ the same in all cases.

nucleation zone. Values $a = 0.015$ and $b = 0.019$ are used (Figure 3.2), which are typical of laboratory experiments. Nucleation proceeds under stress conditions that are relatively homogeneous compared to other cases. However, in this and all other cases, shear stress concentrations do develop, as expected, at the edges of the slowly varying zone of faster slip.

Case 2: The size of the weaker patch, 10 m, is a significant fraction of the nucleation zone that develops. Nucleation proceeds under imposed conditions of heterogeneous normal stress within the nucleation zone. The other parameters are the same as in Case 1.

Case 3: The value of $a = 0.0015$ is 10 times smaller than that of Cases 1 and 2. This value is representative of the ones inferred from aftershock observations based on the model of *Dieterich* [1994], assuming overburden normal stress minus hydrostatic pore pressure [*Gross and Kisslinger*, 1997; *Gross and Bürgmann*, 1998; *Toda et al.*, 1998, 2005]. The parameter $b = 0.0055$ is chosen to keep $(b - a)$ the same as in Cases 1 and 2, ensuring the same steady-state velocity-weakening properties. The size of the weaker region, 10 m, is a significant fraction of the nucleation zone, as in Case 2. Note that the ratio a/b is 0.27 in this Case, while $a/b = 0.79$ for Cases 1 and 2. According to the study of *Rubin and Ampuero* [2005], this represents a qualitative difference, as explained in section 3.1.

3.2.2 Model with rheological transition

The second model contains variations in steady-state friction properties that create rheological transitions. It is analogous to the depth-variable model of *Lapusta et al.* [2000]. The fault motion is still in the along-strike direction x, but only variations with depth z are considered, so that the fault behavior is described by strike-parallel slip $\delta(z,t)$, slip velocity (or slip rate) $V(z,t) = \partial\delta(z,t)/\partial t$, and the relevant component of shear stress $\tau(z,t)$. Unlike the model studied in *Lapusta et al.* [2000], the model here does not include the free surface. The effective normal stress $\bar{\sigma}$ is constant along the entire fault (Figure 3.2).

We have done a number of simulations in this model, varying the values of a and b in the velocity-weakening region (0.0015-0.015 and 0.0055-0.023, respectively) and L (20-160 $\mu\mathrm{m}$). We present results for two representative cases, both with $L = 80\ \mu\mathrm{m}$.

Case 4: $a = 0.015$ and $b = 0.019$ in the steady-state velocity-weakening region, as in Cases 1 and 2 of the model with a weaker patch. Full distributions of a and b are shown in Figure 3.2. This variation is qualitatively similar to the one in *Rice* [1993] and *Lapusta et al.* [2000]. The distributions of a and b are asymmetric with respect to the middle of the fault, so that simulated earthquakes nucleate at one of the rheological transitions.

Case 5: $a = 0.0015$ and $b = 0.0055$ in the steady-state velocity-weakening region, as in Case 3. Throughout the fault domain, this Case has 10 times smaller a than Case 4 and such b that the distribution of $(a - b)$ is the same in both Cases. The same distribution of $(a - b)$ ensures that rheological transitions are at the same locations in both cases.

3.3 Simulated nucleation processes

3.3.1 Nucleation processes due to weaker patches and importance of normal stress heterogeneity

As an example of fault slip simulated in the model with a weaker patch, consider the earthquake sequence for Case 1 (Figure 3.3A). Earthquakes nucleate in the middle of the fault, due to the weaker patch. The earthquakes then spread bilaterally along the strike of the fault; the dashed lines show slip accumulation every 0.01 s during the dynamic rupture. When the rupture reaches zero-stress barriers, it arrests. The interseismic period is 28 years. We take the nucleation process of the third event as the representative one for this Case; the corresponding part in Figure 3.3 is surrounded by a small rectangle.

To study nucleation sizes and aftershock rates, we need to define when the nucleation process ends and the dynamic event begins. In *Dieterich* [1992] and *Dieterich* [1994], quasi-static equations were used, and their solution ceased to exist (i.e., slip velocities became infinite) when inertial effects would have been important in the complete formulation. The time at which the solution ceased to exist was taken as the time of instability onset. Since our simulations fully account for inertial effects and capture the smooth transition between the quasi-static phase and dynamic rupture, defining the beginning of an earthquake is not so simple. We use the criterion based on rupture speed and take, as the onset of instability, the time at which a tip of the actively slipping zone moves with the speed that exceeds a fraction (10%) of the shear wave speed of the surrounding elastic medium. The tips of the actively slipping zone are found as the locations of shear stress concentra-

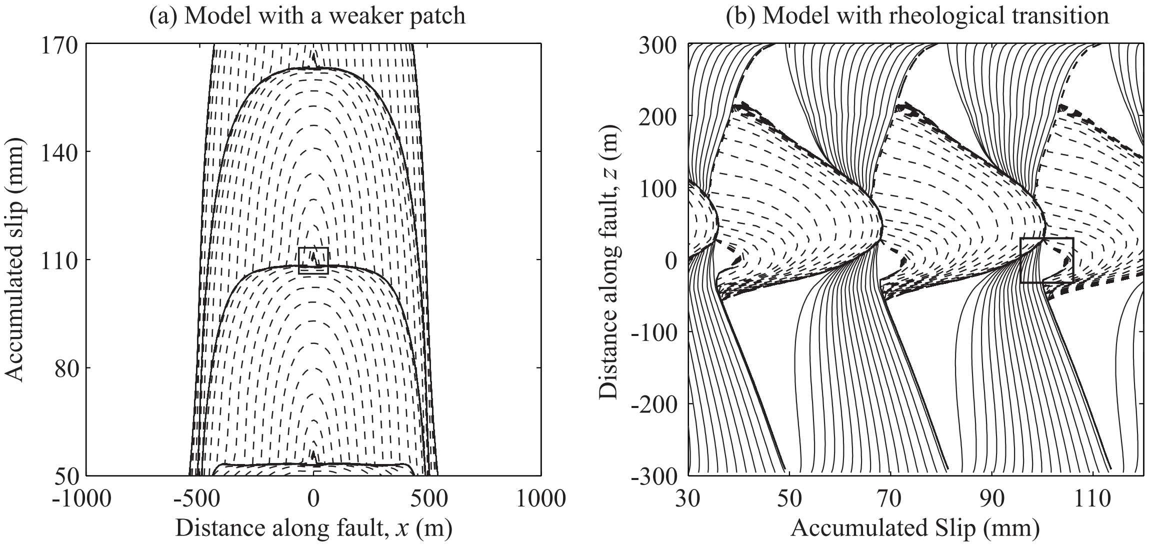

Figure 3.3: Examples of earthquake sequences simulated in the model with a weaker patch (panel A) and in the model with rheological transition (panel B). Solid lines show slip accumulation every 2 years. Dashed lines are intended to capture dynamic events and are plotted every 0.01 seconds during the simulated earthquakes. For each earthquake, the dashed lines are shown from 0.05 seconds before our definition of the onset of an earthquake (rupture speed reaching 10% of the shear wave speed) until the maximum slip velocity on the fault reduces to 1 mm/s. The nucleation process of a representative earthquake is indicated by a rectangle in both panels.

tion. The sliding region changes very slowly in space during the quasi-static deformation, and extends with rupture speeds comparable to the shear wave speed during the dynamic phase. Hence this rupture definition allows us to appropriately capture the transition. An alternative approach would be to define the beginning of an earthquake as the time when slip velocities reach a certain value, e.g., 0.1 m/s, either at a particular location or as a maximum on the fault. Note that the two criteria are related, as faster slip velocities correspond to larger rupture speeds.

Representative nucleation processes for Cases 1-3 are shown in Figure 3.4. The dashed lines in panels A-C show slip accumulation every 0.01 s starting with 0.05 s before our definition of the beginning of an earthquake. The first five dashed lines are almost on top of each other, signifying still relatively slow slip and slow expansion of the sliding region. The sixth line shows much faster slip and expansion, indicating the beginning of a dynamic event. The panels D-F illustrate the imposed distribution of effective normal stress and the approximate extent of the spontaneous nucleation zone.

The comparison of Cases 1 and 2 shows an interesting result. The presence of slight normal stress heterogeneity within the nucleation zone in Case 2 leads to 1.5 times larger nucleation size for that Case, 36 m vs. 24 m for Case 1. Average normal stress is larger in Case 2, with all other parameters being the same, and all existing estimates of earthquake nucleation sizes discussed in section 3.1 would predict that the nucleation size should be smaller in Case 2 than in Case 1, but the opposite is observed. The antiplane estimate of nucleation size by *Rubin and Ampuero* [2005] gives 36 m for the parameters of these cases. Since we use a depth-averaged model, the direction x is affected by a factor of

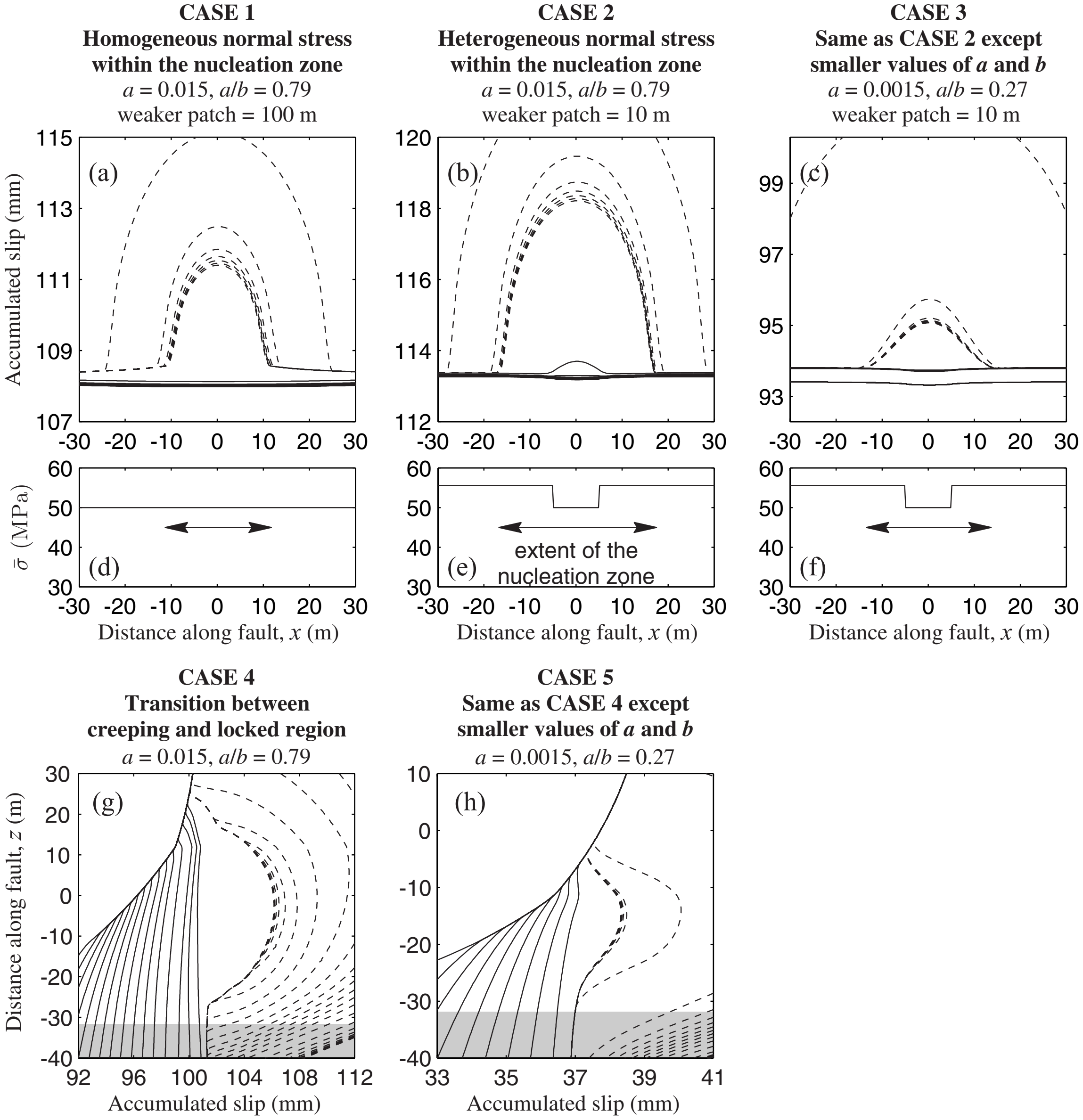

Figure 3.4: (A)-(C) Nucleation processes at weaker patches. Cases 1-3 correspond to either different sizes of the weaker patch or different constitutive parameters a and b. The other parameters are the same for all three cases. Panels D-F show the distribution of effective normal stress $\bar{\sigma}$ in a region that includes the nucleation zone. Double arrows indicate the extent of the nucleation zone for each case. (G)-(H) Nucleation processes at rheological transition. Cases 4 and 5 correspond to different constitutive parameters a and b. Solid and dashed lines in panels A-C and G-H have the same meaning as in Figure 3.3. Shaded areas correspond to velocity-strengthening regions.

$Z = 1/(1-\nu) = 4/3$ (appendix 3.6) and hence the estimate becomes 48 m. This is broadly consistent with the nucleation sizes in Cases 1 and 2, in the sense that the estimate gives a close upper bound. Note that the energy balance in the expanding-crack solution of *Rubin and Ampuero* [2005], when adopted to the normal-stress heterogeneity of Case 2, would be qualitatively consistent with the larger nucleation size for Case 2 (A. Rubin, personal communication, 2007). This result demonstrates that stress heterogeneities on faults can have significant, and sometimes counterintuitive, effect on nucleation processes.

Case 3, with a smaller value of a/b, behaves differently from Cases 1 and 2. The nucleation size in Case 3 is about 29 m. We simulated a number of cases similar to Case 3 but with different sizes of the weaker patch, including the case in which the weaker patch was much larger than the resulting nucleation size. In all those cases, the nucleation size changed very little compared to Case 3. This means that the effect of heterogeneity on the nucleation size is diminished for sufficiently small values of a/b. We also find that smaller values of a/b lead to shorter periods of interseismic deformation between two successive earthquakes. In Case 3, the interseismic period is 23.8 years, smaller than the interseismic period of 29.1 years in Case 2, despite the fact that $(b-a)$ is the same in the two cases.

3.3.2 Nucleation processes due to rheological transitions

An earthquake sequence simulated in the model with rheological transition is shown in Figure 3.3B, using Case 4 as an example. The solid lines are plotted every 2 years and show the continuous slow sliding (creep) of the steady-state velocity-strengthening regions. That slow slip creates stress concentration at its tip and penetrates into the velocity-weakening region. In due time, an earthquake nucleates close to the transition; its progression is shown by dashes lines. After an earthquake arrests, the velocity-strengthening region experiences accelerated sliding, or afterslip, due to the transferred stress. The interseismic period between two successive events is 32 years. We take the nucleation process of the forth event as the representative one for this Case; the relevant part of Figure 3.3 is surrounded by a small rectangle.

Representative nucleation processes for Cases 4 and 5 are shown in Figure 3.4. Nucleation of the simulated earthquakes occurs within the velocity-weakening region, but close to transition to velocity-strengthening friction (panels G and E; the transition is at $z = -32$ m in both cases). Due to interactions with the nearby creeping region, such nucleation proceeds under temporally and spatially non-uniform stress field. The different values for a and b (with the same value of $b-a$) in Cases 4 and 5 lead to notable differences in nucleation processes. The nucleation sizes in Cases 4 and 5 are different and approximately consistent with the estimates of *Rubin and Ampuero* [2005], which are $2\mu Lb/(\pi\bar{\sigma}(b-a)^2) = 36$ m for Case 4 and $2.74\mu L/(\bar{\sigma}b) = 24$ m for Case 5. Note that *Rubin and Ampuero* [2005] gave formulae for half of the nucleation size, but we use full nucleation sizes here. In our simulations, the nucleation sizes are 35 to 40 m for Case 4 and 18 to 24 m for Case 5, as can be estimated from Figure 3.4.

As in the model with a weaker patch, smaller values of a/b result in shorter interseismic periods, but the effect is much stronger in the model with rheological transition. In Case 5, the interseismic period is 18 years, almost twice shorter than the interseismic period of 32 years in Case 4. In the model with a weaker patch, the interseismic period is dictated

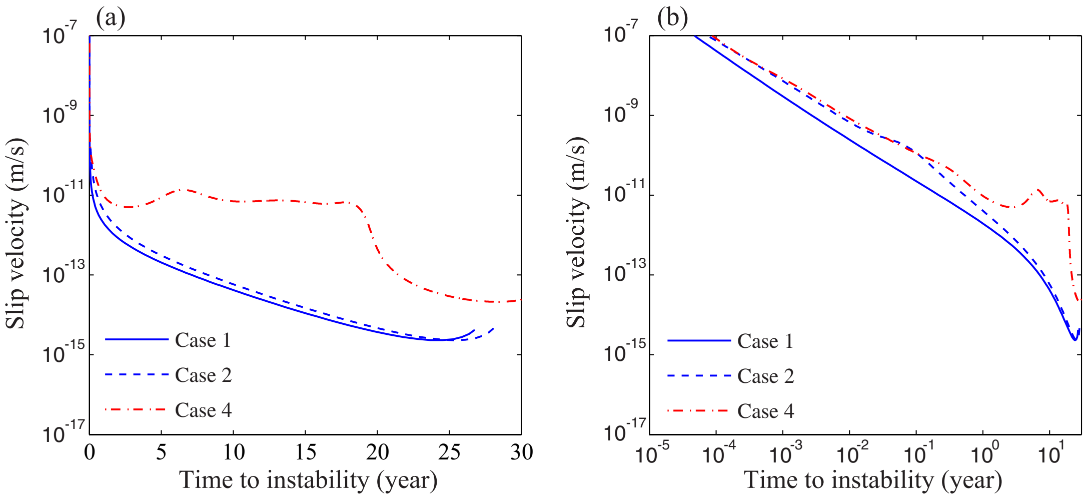

Figure 3.5: Slip-velocity evolution during one earthquake cycle for representative points inside nucleation zones, on linear (panel A) and logarithmic (panel B) time scales. Time to instability T is given by $T = t_2 - t$, $t_1 < t < t_2$, where t_1 and t_2 are the occurrence times of two consecutive earthquakes. For each case, slip velocity for times $t_1 + 1 < t < t_2$ is shown. Slip velocity at $x = 0$ km is plotted for Cases 1 and 2, and slip velocity at $z = 0$ is plotted for Case 4. Note that slip-velocity evolution for nucleation processes at rheological transition is non-monotonic.

by the loading time necessary to rebuild the stress relieved during a dynamic event and hence depends on the static stress drop, which is similar in Cases 1 and 3. In the model with rheological transition, the interseismic period is controlled by the time it takes for the slow slip penetrating from the velocity-strengthening region to create a slipping zone comparable to the nucleation size. Since the nucleation size is almost twice smaller in Case 5 than in Case 4, the interseismic period is also almost twice smaller.

3.3.3 Different time evolution of nucleation in the two models

The nucleation sizes in both models are comparable for a given set of rate and state parameters (Figure 3.4). The question arises whether the time evolution of the nucleation processes in the two models is also similar. In Figure 3.5, we compare slip-velocity evolution for representative points inside the nucleation zones at weaker patches (Cases 1 and 2) and at rheological transitions (Case 4). In the model with a weaker patch, slip velocity gradually increases through the interseismic period, and this behavior is qualitatively consistent with that of spring-slider models [*Dieterich*, 1994; *Gomberg et al.*, 2000]. Still, slip velocity in Cases 1 and 2 is slightly different, especially for the period from 10^{-3} to 10^{0} years before an earthquake (Figure 3.5B). This can only be caused by normal-stress heterogeneity within the nucleation zone, as this is the only difference between Cases 1 and 2. Nucleation in the model with rheological transition (Case 4) is significantly different: slip velocity increases first, then stays relatively constant for about 20 years, with some oscillations, and later increases further. This complex non-monotonic behavior is due to penetration of slip from the nearby slowly slipping region. The creeping region concentrates stress at its edge, causing slip there and expanding itself. This process moves the stress concentration along the fault and results in time-dependent heterogeneity of shear stress within the nucleation zone. We find the corresponding fluctuations of slip velocity in all cases we have studied in the model with rheological transition. Note that variations in slip velocity are linked to variations of $V\theta/L$, the quantity important in the aftershock model of *Dieterich* [1994].

Hence we find that earthquake nucleation in the two models proceeds differently, as demonstrated by slip-velocity evolution of points within the nucleation zone. The differences are caused by spatial and temporal stress heterogeneity within the nucleation zone and result in significant consequences for aftershock rates (section 4.1).

3.4 Dependence of nucleation processes and sizes on loading history

As discussed in section 3.1, several simple analytical estimates $h_{\text{nucl}} = \eta GL/(\bar{\sigma}F)$ for the nucleation size have been proposed. In particular, $F = b$ was advocated by *Dieterich* [1992]. *Rubin and Ampuero* [2005] found that $F = b$ is valid in a certain parameter regime, $a/b \lesssim 0.37$, while $F = b/(b-a)^2$ holds for $a/b \gtrsim 0.5$. This is because, for $a/b, \gtrsim 0.5$ the condition $V\theta/L \gg 1$ adopted by *Dieterich* [1992] breaks down in the middle of the nucleation zone under quasi-static tectonic loading. The Dieterich and Rubin-Ampuero estimates are quite different for the values of a close to b. *Rubin and Ampuero* [2005] mentioned that "the loading conditions play a role, and could potentially place nucleation in the regime $V\theta/L \gg 1$ even for large a/b," citing a stress step and the associated instantaneous change in slip velocity as an example.

We find that nucleation evolution and size are indeed strongly controlled by loading history. Our simulations of nucleation under slow tectonic loading result, for both models, in nucleation sizes consistent with the estimates of *Rubin and Ampuero* [2005] (section 3.3). However, other reasonable loading histories can make the nucleation size closer to the estimate of *Dieterich* [1992] even for the parameter range $a/b \gtrsim 0.5$. As an example, consider a nucleation process in the model with a weaker patch for a case conceptually similar to Case 1 of section 3.3, but with $L = 20\ \mu\text{m}$, $a/b = 0.94$, $b = 0.016$, and the weaker patch size of 200 m. If we use the model-dependent constants η from antiplane models ($\eta = 2.5$ for Dieterich, $\eta = 2/\pi$ for Rubin and Ampuero) multiplied by parameter

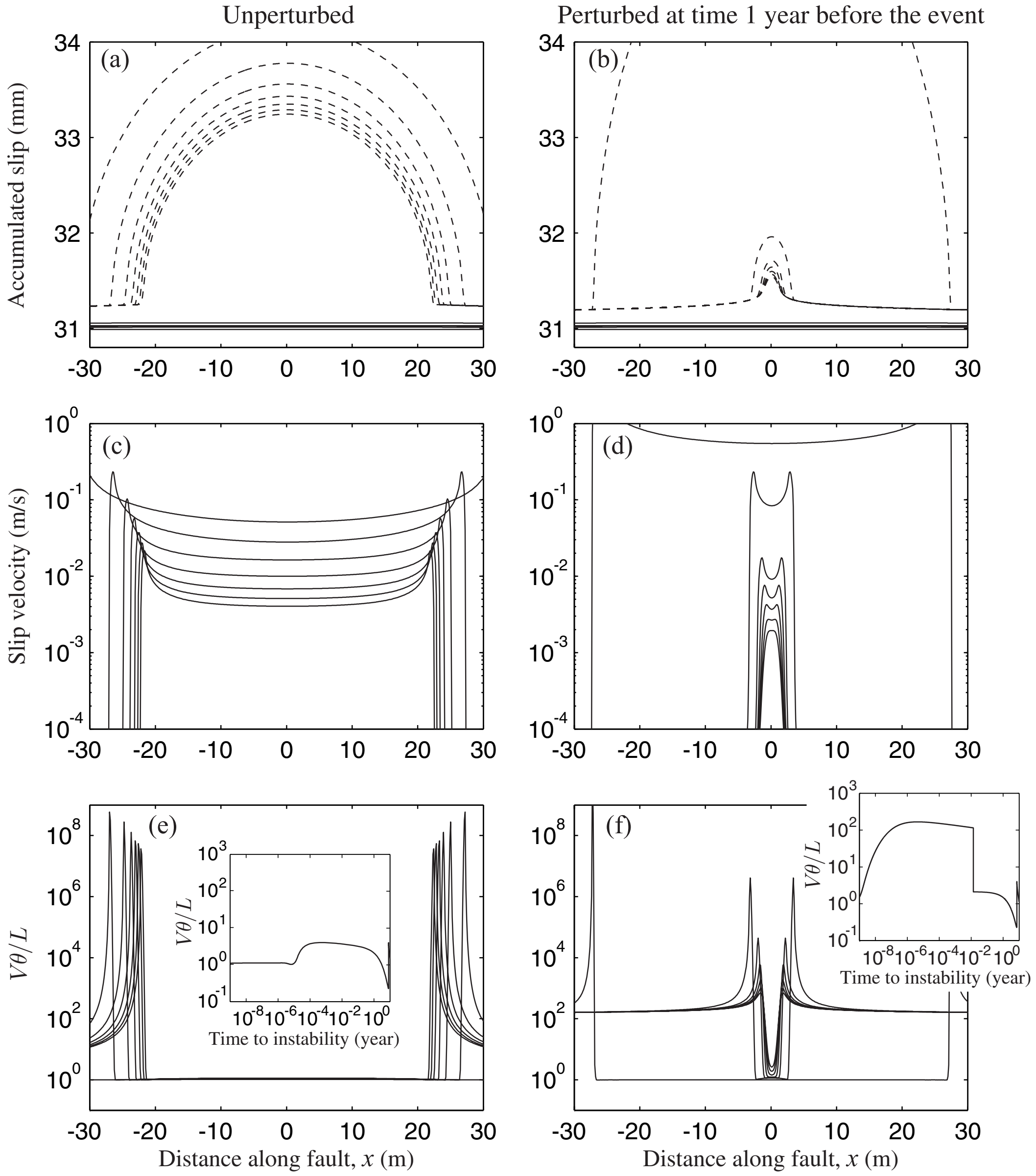

Figure 3.6: Dependence of nucleation processes on loading history. Panels A, C, and E correspond to an unperturbed nucleation process in a model with a weaker patch and a = 0.015, a/b = 0.94, L = 20 $\mu\mathrm{m}$ and the weaker patch size of 200 m. The same nucleation process but perturbed with $\Delta\tau$ = 3.0 MPa at one year before the original instability is shown in panels B, D, and F. The dashed lines in panels A and B are plotted every 0.01 seconds staring with 0.05 seconds before our definition of the onset of instability. The solid lines in the rest of the panels correspond to the times of dashed lines from panels A and B. The first 5 lines cluster, indicating the spatial extent of the nucleation zone. The insets show the evolution of $V\theta/L$ at $x = 0$ m. The nucleation sizes in these two cases differ by an order of magnitude.

$Z = 4/3$ (appendix 3.6), the two estimates are 2.5 m and 162 m, respectively, with the Rubin-Ampuero estimate 65 times larger than that of Dieterich. We consider two cases: nucleation proceeding under slow tectonic loading (panels A, C, and E of Figure 3.6) and nucleation that experiences, in addition to slow tectonic loading, a positive shear stress step one year before the original time to instability (panels B, D, and F of Figure 3.6). We find that the perturbed case has a much smaller nucleation size than the unperturbed case, 5.5 m vs. 53 m. The new time to instability is 0.014 years.

The difference between the two scenarios can be explained by the evolution of $V\theta/L$ in the nucleation zone, shown in panels E and F. The unperturbed scenario is consistent with the study of *Rubin and Ampuero* [2005] and follows the evolution typical for values of $a/b \gtrsim 0.5$, with $V\theta/L$ of order 1 in the middle of the nucleation zone for times close to instability (panel E). In the perturbed case, $V\theta/L$ becomes, after the shear stress step, much larger than one throughout the nucleation zone and $V\theta/L$ reduces to one in the nucleation region only after tips of the rupture start to expand dynamically (inset in panel F). Hence, due to the stress perturbation, the condition $V\theta/L \gg 1$ becomes valid throughout the nucleation zone and stays valid until the dynamic event, leading to a much smaller nucleation size more consistent with the estimate of *Dieterich* [1992].

This example demonstrates how different loading conditions can change the nucleation process and, in particular, cause order-of-magnitude differences in nucleation sizes. In laboratory experiments, slow loading over tectonic time scales is not feasible, and much faster loading must be used, rapidly increasing V and potentially leading to $V\theta/L \gg 1$ everywhere within the nucleation region even for $a/b \gtrsim 0.5$. This may explain why experiments of *Dieterich and Kilgore* [1996] were consistent with the results of *Dieterich* [1992], even though laboratory values of a/b often fall into the range $a/b \gtrsim 0.5$.

3.5 Conclusions

Using two different fault models, we have simulated several plausible scenarios of spontaneous earthquake nucleation. The nucleation processes have been simulated in continuum models as a part of long-term slip history that involves rapid dynamic events (simulated earthquakes) as well as pre-, inter-, and postseismic slip.

We find significant differences among the simulated nucleation processes. Nucleation processes at weaker patches behave similarly to theories based on spring-slider models, with some notable deviations, whereas nucleation processes at rheological transitions behave differently, producing complex slip-velocity histories. In particular, nucleation sizes are affected by normal-stress heterogeneity in the nucleation zone. Nucleation processes due to rheological transitions originate as the extension of creep in the nearby velocity-strengthening region, producing non-monotonic evolution of slip velocity at the rheological transition. These differences suggest that nucleation processes depend on the conditions under which nucleation occurs on natural faults, and have important implications for aftershock phenomena as discussed in Chapter 4.

Nucleation processes simulated with different loading histories can have nucleation sizes that differ by an order of magnitude and cannot be predicted by a single existing theoretical estimate. Nucleation sizes obtained with slow tectonic-like loading are consistent with the estimates of *Rubin and Ampuero* [2005]. For models with $a/b \gtrsim 0.5$, loading histories that involve positive shear stress steps can result in significantly smaller nucleation sizes, closer to the estimate of *Dieterich* [1992]. The behavior can be explained by the evolution of $V\theta/L$ in the nucleation zone and implies that final nucleation stages of aftershocks and other triggered events may be different from those of events nucleating under slow tectonic loading. In particular, nucleation sizes of aftershocks may be significantly smaller.

3.6 Appendix: Elastodynamic equations and numerical parameters

The model with a weaker patch is based on the crustal-plane model described in *Lapusta* [2001]. The only non-zero component of the displacement is in the along-strike direction x and it is averaged over the depth H_{seismic} of the fault. The elastodynamic equation for the depth-averaged displacement $\bar{u}(x,y,t)$ is [*Lehner et al.*, 1981; *Lapusta*, 2001]:

$$Z^2\frac{\partial^2\bar{u}}{\partial x^2}+\frac{\partial^2\bar{u}}{\partial y^2}+\frac{1}{H_{\text{eff}}^2}\left(\frac{1}{2}\text{sign}(y)V_{\text{L}}t-\bar{u}\right)=\frac{1}{c_s^2}\frac{\partial^2\bar{u}}{\partial t^2}\ , \tag{3.2}$$

where $H_{\text{eff}}=(\pi/4)H_{\text{seismic}}$, $Z=1/(1-\nu)$, ν is Poisson’s ratio, and c_s is the shear wave speed. We use $H_{\text{seismic}}=150$ m. The third term on the left-hand side of the equation represents coupling to regions that are steadily moving with slip velocity V_{L}. The crustal-plane model in *Lapusta* [2001] incorporated a free surface and loading from a deeper region. In the model with a weaker patch, the seismogenic region is loaded by two regions and there is no free surface (Figure 3.1A). This leads to a factor of two in front of V_{L} in equation

(3.2). The effective shear wave speed in the direction of the strike is $Zc_s = 4$ km/s for values $\nu = 0.25$ and $c_s = 3$ km/s used in this study. The along-strike slip is given by $\delta(x,t) = \bar{u}(x, y = 0^+, t) - \bar{u}(x, y = 0^-, t)$. Using the same notation as in *Lapusta et al.* [2000] and *Lapusta* [2001], the typical numerical parameters are as follows. There are $N_{\text{ele}} = 8192$ spatial elements along the simulated fault domain $\lambda = 2000$ m. The ratio $h^*/h = 50.1$ of the critical cell size h^* to the cell size $h = 0.244$ m ensures well-resolved simulations [*Lapusta et al.*, 2000]. Time t is discretized into variable time steps, with the minimum value of $0.25h/c_s = 15$ μs and the maximum value of 0.2 years. In the mode-dependent convolution truncation, $T_w(1) = \lambda/c_s$ and $q_w = 4$.

The elastodynamic equations and simulation methodology for the model with rheological transition are the same as in *Lapusta et al.* [2000]. The simulated fault domain $\lambda = 1200$ m is composed of the 600-m region where friction is applied, and the 600-m loading region of the prescribed slip rate. In *Lapusta et al.* [2000], domain λ also included a mirror fault image to simulate the effects of a free surface, but the model here does not contain a free surface. The domain λ is discretized into $N_{\text{ele}} = 4096$ equal spatial elements, each with the size $h = 0.29$ m, so that $h^*/h = 32.2$. For time discretization and convolution computation, we use the same parameters as in the model with a weaker patch.

Chapter 4

Aftershock Rates Due to Static Triggering in Continuum Models of Rate and State Faults

In Chapter 3, we have considered five representative cases of earthquake nucleation, compared them in terms of their slip-velocity evolution, and discussed the effects of heterogeneity in normal stress, heterogeneity in friction properties, and variations in loading (sections 3.3 and 3.4). We find significant differences among the simulated nucleation processes. Since their spatial extent varies with time and their slip and slip velocity vary with space, it is not obvious how to make the direct comparison of the nucleation processes with each other and the ones in spring-slider models. To facilitate such comparison, we study the response of the simulated nucleation processes to static stress changes and the resulting aftershock rates, compare them with the results of *Dieterich* [1994], and explain the observed similarities and differences (sections 4.1-4.4).

In computing the aftershock rates, we assume, following previous approaches [*Dieterich*, 1994; *Gomberg et al.*, 2000; *Gomberg*, 2001], that the aftershock-producing nucleation sites are all governed by the same nucleation process, albeit time shifted for each nucleation site. On natural faults, different nucleation sites may have different friction properties, stress conditions, stressing rates, etc., and one would need to consider, in general, a combination of nucleation models of the kind studied in this Chapter to make meaningful comparisons with aftershock observations. Our results on aftershock rates may be useful for explaining observations in special cases, as we show in section 4.2 for a cluster of aftershocks located at rheological transition. However, the main purpose of the study is to determine whether the response of rate and state faults to static stress perturbations changes if one uses models of faults in elastic continuum rather than spring-slider models.

This Chapter is based on Sections 5-8 of the paper “Variability of earthquake nucleation in continuum models of rate-and-state faults and implications for aftershock rates” by Y. Kaneko and N. Lapusta (*J. Geophys. Res.*, 2008).

4.1 Comparing nucleation processes by their response to static stress changes and resulting aftershock rates

4.1.1 Procedure for determining aftershock rates

Following *Dieterich* [1994], we consider a preexisting population of rate and state nucleation sites distributed in the volume of a prospective aftershock region (Figure 4.1A). Just prior to the time of the mainshock, each site is at a different stage in the nucleation process so that the population of nucleation sites would result in a constant background earthquake rate if left unperturbed. The mainshock perturbs the nucleation sites, causing the nucleation to proceed differently and resulting in a nonconstant rate, which can be called the

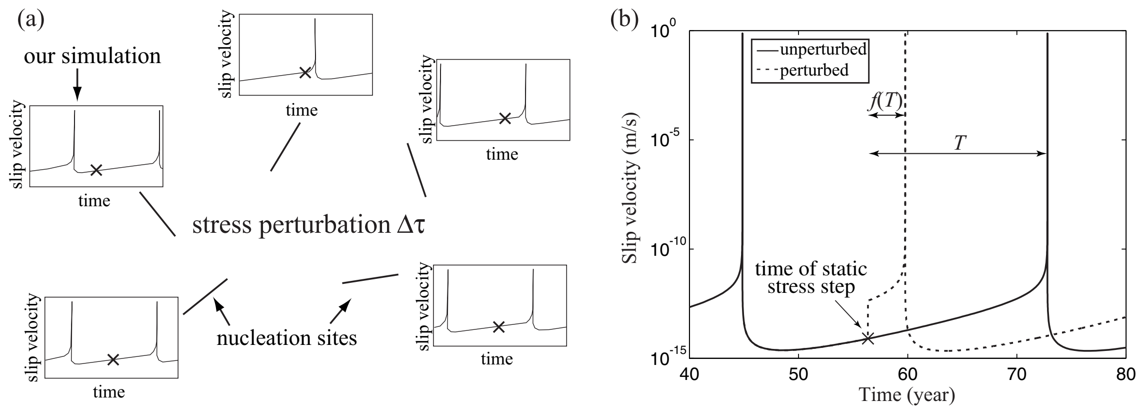

Figure 4.1: (A) A cartoon illustrating a population of nucleation sites just before a stress perturbation due to a mainshock. Each nucleation site follows nucleation behavior simulated in a continuum fault model. At the time of the perturbation (shown by ’$\times$’), nucleation sites are at different stages of the nucleation process, with the stages selected in such a way that the population would produce a constant (background) earthquake rate if left unperturbed. After stress step $\Delta\tau$ due to the mainshock, the population produces a nonconstant earthquake rate (aftershock rate). (B) Nucleation process of each site and its perturbation are illustrated using slip velocity at a representative point. The solid and dashed lines show the unperturbed and perturbed response, respectively. A static stress step is applied at the time indicated by ’$\times$’. T and $f(T)$ denote the original time to instability and the new time to instability, respectively. This example shows slip velocity at the middle of the nucleation zone for Case 1. The model is perturbed at $T = 16.4$ years before instability with a stress step $\Delta\tau = 3.0$ MPa; the new time to instability is $f(T) = 3.4$ years.

aftershock rate. We consider the situation when the population experiences a static stress change in the form of a uniform positive shear stress step, except in section 4.2 where a case with nonuniform stress step is studied.

To compute the aftershock rate, we need to know how the rate and state nucleation at each site reacts to such change in stress. Let us denote by T the time from the application of the stress perturbation to the unperturbed failure time. We call T the original time to instability. Let us denote by $f(T)$ the new time to instability, i.e., the changed time to instability due to the stress perturbation. To compute the aftershock rate, we only need to know $f(T)$ for all T of interest. For monotonic $f(T)$, the aftershock rate R is given by

(*Gomberg et al.* [2000], appendix 4.7)

$$\frac{R}{r} = \frac{dT}{df} \; . \tag{4.1}$$

For non-monotonic $f(T)$, which arise in one of the models, the inverse dependence $T(f)$ is multivalued, and equation (4.1) cannot be used. The approach we developed for that situation is described in appendix 4.7.

For each nucleation example described in section 3.3, we find $f(T)$ numerically by the following procedure. Each stage of a given nucleation process can be labeled by its time to instability T (Figure 4.1B). We select many values of T and, for each of them, we conduct a simulation in which we perturb the nucleation process by imposing a static stress step in the fault model at time T before the instability. In the simulation with the perturbation, the instability occurs at a different time, giving us the new time to instability $f(T)$. This numerically constructed $f(T)$ is used to compute the aftershock rate.

One of the important differences between our computation of aftershock rates and the model of *Dieterich* [1994] is that the original time to instability T in our model cannot be longer than the simulated interseismic period, whereas in the model of *Dieterich* [1994], the population of preexisting nucleation sites can include sites with any original (or unperturbed) times to instability T. However, for any non-zero stressing rate $\dot{\tau}$, the assumption that nucleation processes can be arbitrarily long is not physically plausible. If τ_{fail} is an upper bound of failure stress, then the nucleation site would have to fail within the time of the order of $\tau_{\mathrm{fail}}/\dot{\tau}$. That consideration imposes a physical limit on how large the times to instability T can be in the preexisting population even in the model of *Dieterich* [1994], although, mathematically, analytical expression (4.12) that relates the time to instability and slip velocity of each nucleation site can be used for any T.

Our method of computing aftershock rates can be used to find aftershock rates due to perturbations of any time-dependent nucleation process. In addition, this approach can be readily extended to dynamic perturbations and to more complex scenarios in terms of the initial nucleation population and spatial distribution of stress change. One such combined scenario, with spatially varying stress changes, is considered in section 4.2.

4.1.2 Aftershock rates based on nucleation processes at weaker patches: Overall similarity to spring-slider models, effects of heterogeneous normal stress

Nucleation processes in the model with a weaker patch lead to response functions $f(T)$ and aftershock rates shown as dotted lines in panels A-C and D-F of Figure 4.2. Each dot in panels A-C corresponds to a separate simulation. Note that a nucleation site with the new time to instability f will contribute to aftershock rates at the time f after the mainshock, and that links the horizontal axes of panels A-C with those of panels D-F. For Cases 1-2, the static stress step $\Delta\tau = 3.0$ MPa is used; for Case 3 of ten times smaller a, $\Delta\tau = 0.30$ MPa is used, to have the same value of $\Delta\tau/(a\bar{\sigma})$. The analytical solutions of *Dieterich* [1994], computed from equations (4.16) and (4.12) of appendix 4.6, are shown for comparison as dashed lines. To compute the analytical solutions, we take the value of effective normal stress $\bar{\sigma}$ corresponding to the average over the nucleation zone. The stressing rate $\dot{\tau}$ is computed in our simulations by taking the time derivative of shear stress outside the nucleation zone (i.e., in the locked region). We find that $\dot{\tau}$ is constant before and after the perturbation and equal to 0.255 MPa/yr.

The numerically computed response function $f(T)$ and the corresponding aftershock rates nearly coincide with the analytical solution of *Dieterich* [1994] for Case 1 (panels A and D) of homogeneous $\bar{\sigma}$ within the nucleation zone. A small deviation occurs only for times after the mainshock smaller than 10^{-7} years, as shown in the inset of panel D. For heterogeneous $\bar{\sigma}$ within the nucleation zone, $f(T)$ and aftershock rates clearly deviate from the results of *Dieterich* [1994] (Case 2, panels B and E): The aftershock rates are higher right after the mainshock, and there is a peak in the aftershock rates (panel E). This is consistent with the differences in slip velocities for unperturbed nucleation processes discussed in section 3.3 (Figure 3.5). New times to instability smaller than 10^{-2} years, for which the aftershock rates in Case 2 are higher than in the model of *Dieterich* [1994] and higher than in Case 1, correspond to original times to instability smaller than about 10^0 years, which is when unperturbed slip velocities of Cases 1 and 2 develop more substantial differences (Figure 3.5B). Case 3 (panels C and F) shows that decreasing the ratio a/b, while keeping the same value of $\Delta\tau/(a\bar{\sigma})$, the same value of $(b-a)$, and the same heterogeneity in normal stress, nearly eliminates the difference between the resulting aftershock rates and the analytical solution. For all three cases, the aftershock duration agrees with the prediction $t_a = a\bar{\sigma}/\dot{\tau}$ of *Dieterich* [1994], as do the aftershock rates for times close to t_a. These results and their relation to the time evolution of slip velocity and the validity of the assumption $V\theta/L \gg 1$ are further analyzed in sections 4.3 and 4.4.

Aftershock rates exhibit a nearly constant value right after the stress step (panels D-F),

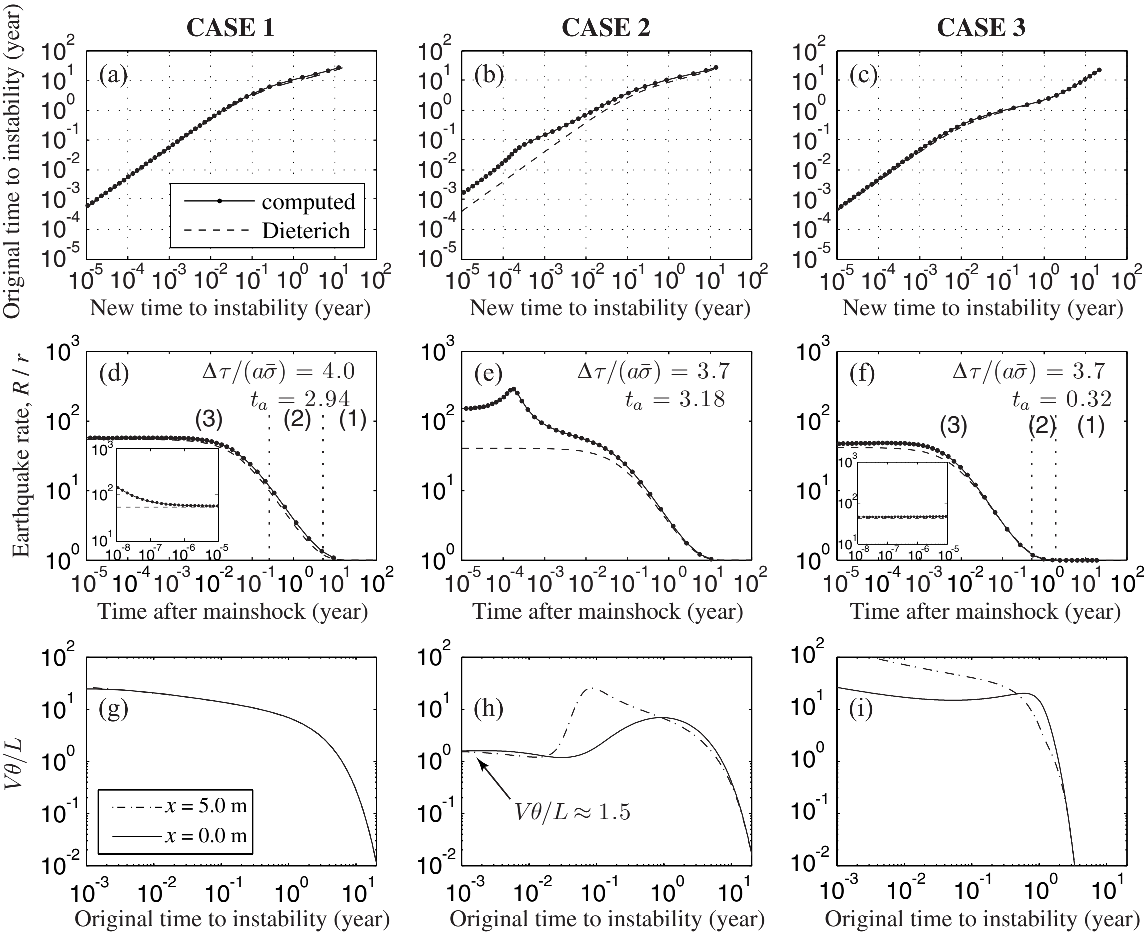

Figure 4.2: Response to static stress steps and the resulting aftershock rates for Cases 1-3 of nucleation at a weaker patch. Panels A-C show the simulated response to stress steps (dotted solid lines) and compare it with the analytical results of *Dieterich* [1994] (dashed lines). In the text, the original time to instability is referred to as T and the new time to instability is referred to as $f(T)$. Panels D-F depict aftershock rates computed based on panels A-C (dotted solid lines) and compare them with Dieterich's analytical result (dashed lines). The new time to instability in A-C corresponds to the time after the mainshock in D-F. The normalized stress step $\Delta\tau/(a\bar{\sigma})$ and the aftershock duration $t_a = a\bar{\sigma}/\dot{\tau}$ for each Case are indicated. Panels G-I show evolution of $V\theta/L$ before the dynamic event for unperturbed simulations at two locations inside the nucleation region.

which lasts for about 3 days in Case 1. This plateau is consistent with the prediction of spring-slider models. The plateau duration can be shortened by increasing the value of $\Delta\tau/(a\bar{\sigma})$ (appendix 4.6). In Case 1, $\Delta\tau/(a\bar{\sigma}) = 4.0$ with $\Delta\tau = 3.0$ MPa, $\bar{\sigma} = 50$ MPa, and $a = 0.01$. Since $\Delta\tau = 3.0$ MPa is already a high value for a static stress change, one can shorten the plateau duration only by using either smaller $\bar{\sigma}$, or smaller a, or both. That is why interpretations of aftershock observations using the model of *Dieterich* [1994] typically result in values of $a\bar{\sigma}$ one to two orders of magnitude smaller than the one we use in Case 1 [*Gross and Kisslinger*, 1997; *Gross and Bürgmann*, 1998; *Toda et al.*, 1998, 2005]. Note that introduction of slight normal-stress heterogeneity in the nucleation region (Case 2) results in higher aftershock rates after the mainshock followed by a peak, and that behavior effectively shortens the duration of the plateau.

4.1.3 Aftershock rates based on nucleation processes at rheological transitions: Aftershock peaks and seismic quiescence

Figure 4.3 shows aftershock rates computed using nucleation processes from the model with rheological transition and compares them with the analytical rates computed based on *Dieterich* [1994] (equation (4.12)). Cases 4 and 5 are defined in section 3.2.2. In Case 4, we apply shear stress step $\Delta\tau$ such that $\Delta\tau/(a\bar{\sigma}) = 0.4$. In Case 5, we use the same $\Delta\tau$ that results in $\Delta\tau/(a\bar{\sigma}) = 4.0$. Case 6 is based on the nucleation process of Case 4 but perturbed with a higher shear stress step corresponding to $\Delta\tau/(a\bar{\sigma}) = 4.0$. For the analytical solution of *Dieterich* [1994], we use $\bar{\sigma} = 50$ MPa and $\dot{\tau} = 0.087$ MPa/year; the value of the stressing rate is computed in our simulations by taking the time derivative of

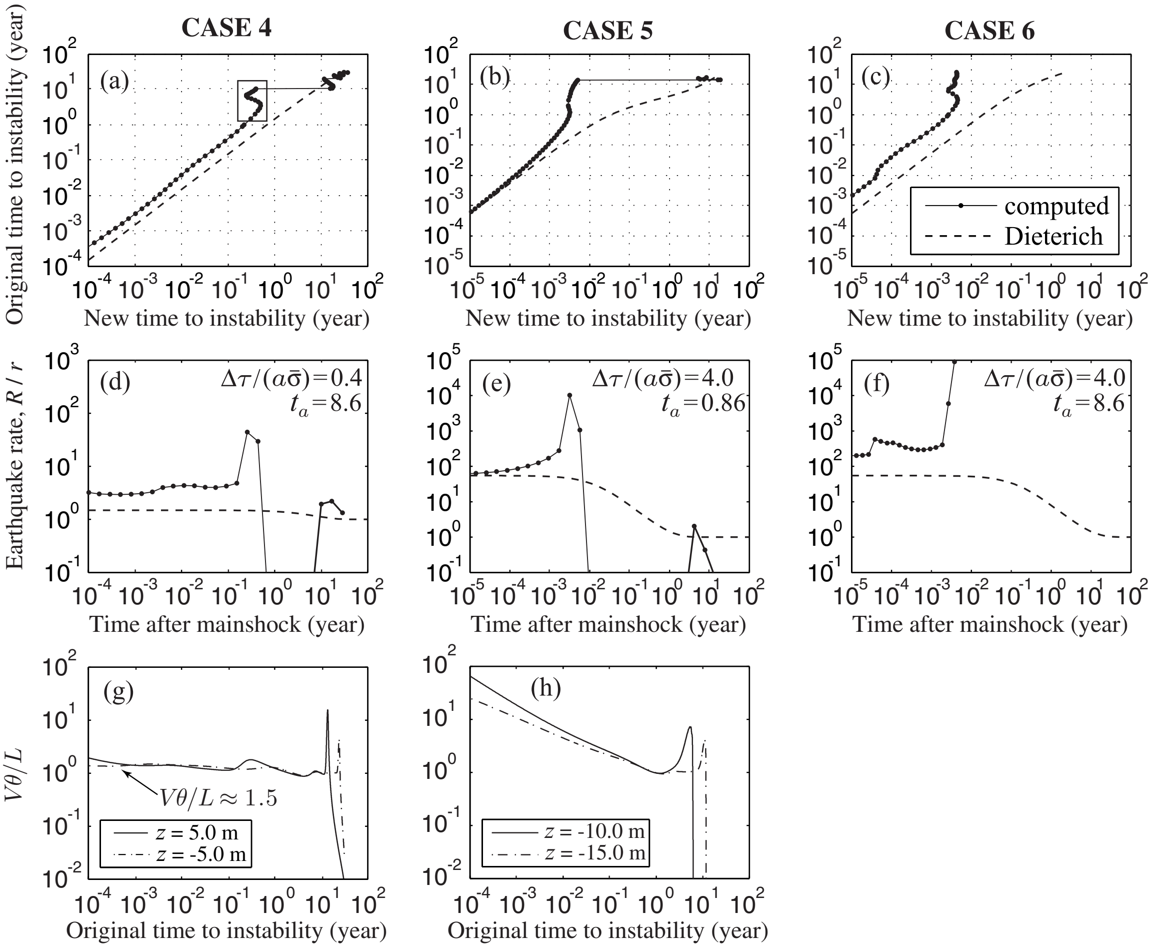

Figure 4.3: Response to static stress steps and the resulting aftershock rates for Cases 4 and 5 of nucleation at rheological transitions. Panels and lines have the same meaning as in Figure 4.2. Note that response $f(T)$ to static stress changes and the resulting aftershock rates are non-monotonic and qualitatively different from the analytical results of *Dieterich* [1994]. The box in panel A indicates the part of $f(T)$ shown in Figure 4.10.

shear stress within the locked region close to the nucleation zone (at $z = 50$ m).

In contrast to the behavior of nucleation processes due to weaker patches, nucleation processes due to rheological transitions give rise to complex non-monotonic response $f(T)$ (Figure 4.3, panels A-C). To understand the origin of the complexity, let us consider the effect of a static stress step applied to the nucleation process of Case 4 at several different times. Panels A-F of Figure 4.4 give time histories of maximum slip velocity within a part

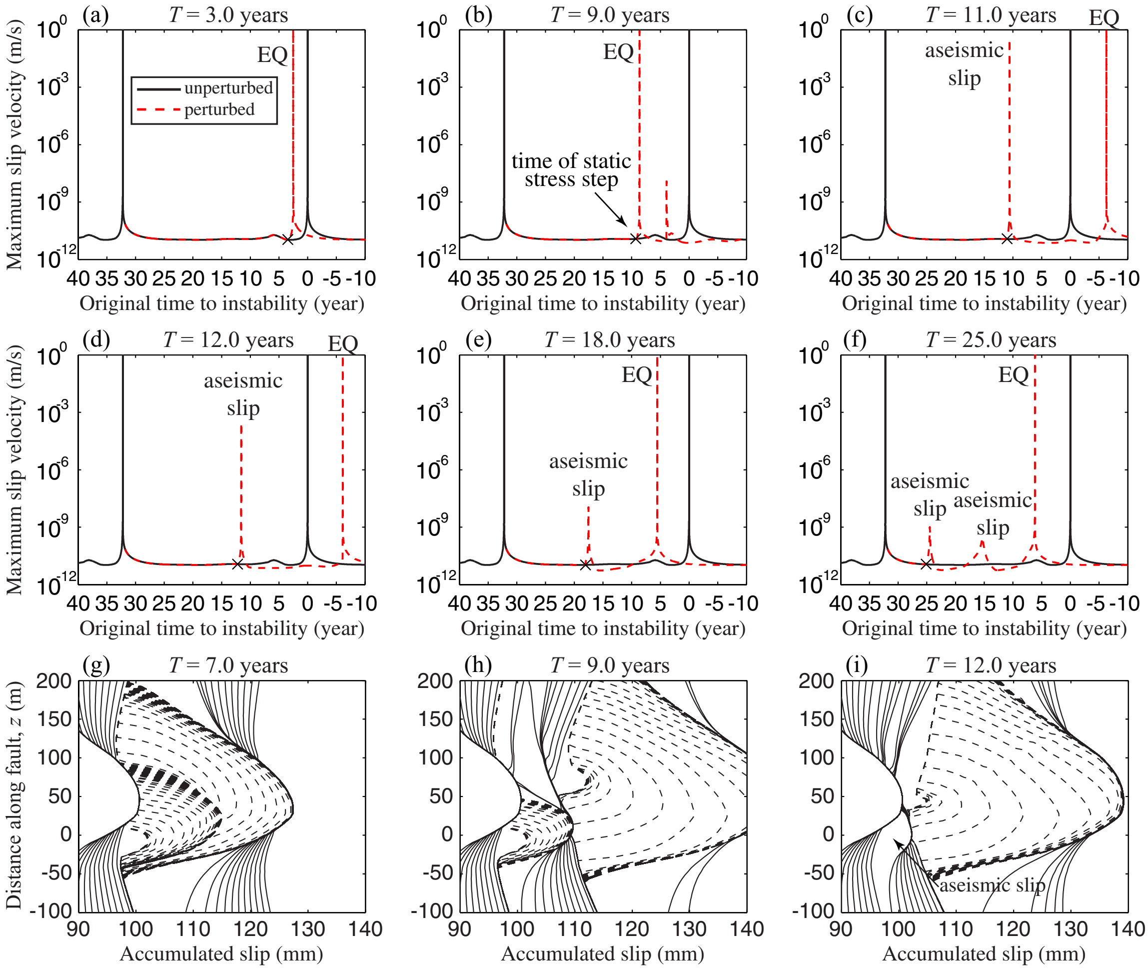

Figure 4.4: Response to static stress steps in the model with rheological transition (Case 4). Panels A-F: Solid lines show the unperturbed evolution of maximum slip velocity within a part of the velocity-weakening region (-32 m $\leq z \leq$ 50 m) that contains the nucleation zone. Times of the stress perturbation are given on the top of each panel and marked by ’×’. Red dashed lines indicate the resulting perturbed behavior. Panels G-I: The effect of stress perturbations on the pattern of slip accumulation. The comparison between the panels is discussed in the text. Note that a positive shear stress step can delay the timing of the subsequent earthquake by inducing an seismic transient (panels C, D, I).

of the velocity-weakening region, -32 m $\leq z \leq 50$ m, for both unperturbed and perturbed simulations. If the stress step is applied to the nucleation process when its original (unperturbed) time to instability T is 1 to 10 years, the triggered earthquake occurs in about 0.4 to 0.5 years (i.e., $f(T) = 0.4$ to 0.5 years), as illustrated in panels A-B. That is why the aftershock rate for Case 4 has a pronounced peak at about 0.4 to 0.5 years after the mainshock (Figure 4.3, panel D). However, stress perturbation at $T = 11$ years results in a very different value of $f(T) = 16$ years (panel C), actually postponing the dynamic event. This is because the immediate consequence of the stress step is to induce more rapid slip but, for the perturbation at $T = 11$ years, this more rapid slip fails to accelerate all the way to instability, relieving the elevated stress in the nucleation region aseismically and decreasing slip velocities throughout the nucleation zone (from the maximum of about 10^{-11} m/s to 10^{-14} m/s). That aseismic response postpones the next acceleration to dynamic instability and makes the new time to instability larger than the original time to instability.

This behavior demonstrates how a positive shear stress step can delay the time to instability, inducing an aseismic slip transient instead of nucleating unstable slip sooner. The change in slip behavior is actually gradual for different T, with the size of the triggered earthquakes decreasing as the stress step is applied at values of T from 1 to 10 years, until, for $T \gtrsim 10$ years, the stress step only causes transient acceleration of aseismic slip that fails to directly initiate a dynamic event. This is illustrated in panels G-I of Figure 4.4. For a stress step applied at $T = 7.0$ years (panel G), the triggered earthquake is of comparable size to events in the unperturbed simulation (Figure 3.3, panel B) but the triggered event almost arrests halfway through, as evidenced by dense spacing of dashed lines, due to insufficient level of shear stress at locations from z = 60 to z = 100 m. For $T = 9.0$ years (panel H), the triggered dynamic event is noticeably smaller than the unperturbed one; this is because shear stress further along the fault is not yet ready to support a larger event. Panel H also shows a larger event that occurs 20 years later. For $T = 12.0$ years (panel I), a stress step fails to induce dynamic instability and results in aseismic transient. The next seismic event occurs in 18 years (panels D, I), which means that the stress step replaced the original time to instability of 12 years with the *longer* new time to instability of $f(T) = 18$ years. For larger T, the triggered aseismic slip decreases in magnitude and area, relieving less of the accumulated stress and allowing the next dynamic event to initiate sooner, until the new time to instability is shorter than the original time to instability (panel E). The smaller and smaller immediate impact of the stress step for larger values of T makes intuitive sense, since the model is farther from generating unstable slip. For stress steps at even larger values of T, the nucleation process exhibits even more complex response, trying to accelerate twice before finally producing a dynamic event (panel F).

This response to static stress changes is more complex than the one found by *Perfettini et al.* [2003] in a similar model with rheological transition. *Perfettini et al.* [2003] concluded that the time advance of rate and state nucleation due to a static stress perturbation is similar to the one predicted by the Coulomb-failure model for most of the earthquake cycle. This is similar to the conclusion we draw for some cases in the model with a weaker patch (section 4.4, scenario 1) but not for the model with the rheological transition. Simulations in *Perfettini et al.* [2003] used quasi-dynamic methodology that does not fully account for inertial effects as we do here, which may have diminished the slip response to abrupt stress changes. However, the main difference seems to be the selection of rate and state parameters and the resulting nucleation size. For the parameter selections in our models, nucleation sizes are several times smaller than the seismogenic region and nucleation occurs close to the rheological transition. Hence the expanding slow-slip region enters the zone of the eventual acceleration towards a dynamic event very early in the earthquake cycle, and the time- and space-dependent stress concentration at the tip of the slow-slip region constitutes a significant part of the nucleation zone. In *Perfettini et al.* [2003], parameter choices led to much larger nucleation zone in the middle of the seismogenic zone, which formed after the slow-slip regions from both sides of the seismogenic region merged. That is likely why in the work of *Perfettini et al.* [2003], for most of the interseismic period, stress steps could only create an effect similar to Coulomb-failure models, as described by scenario 1 of section 4.4.

The aftershock rates computed based on the complex non-monotonic functions $f(T)$ do not have power-law decay and do not match the analytical solution of *Dieterich* [1994] (Figure 4.3, panels D-F), exhibiting a pronounced delayed peak followed by the period of very low or even zero aftershock rates (depending on whether one treats the changes in $f(T)$ discussed above as continuous or discontinuous during interpolations). Note that the smaller value of a/b in Case 5 does not eliminate the significant differences between the numerically constructed aftershock rates and the analytical results of *Dieterich* [1994], as we have observed in the model with a weaker patch. In the model with rheological transition, the complex interplay of seismic and aseismic processes and the resulting complex aftershock response occur for all values of a/b, as the complexity is caused by the vicinity of rheological transition.

The periods of zero or near-zero aftershock rates correspond to seismic quiescence. In Case 4, all new times to instability are either larger than 11 years or smaller than 0.5 years. This means that there are no stages of the nucleation process that, when perturbed, result in new times to instability between 0.5 to 11 years. That is why there is quiescence of aftershocks in that time period (Figure 4.3, panel D). Using spring-slider models, *Gomberg et al.* [2005] showed that quiescence at the end of the aftershock sequence can be explained by the absence of nucleation sites that are sufficiently far from instability. That is consistent with our results in Case 6 (Figure 4.3, panel F), where all available nucleation sites produce earthquakes in the first 10^{-2} years after the stress perturbation, and there are no nucleation sites left to contribute to aftershock rates at later times. We emphasize that there is a different kind of quiescence in this model, one that originates not from the lack of nucleation sites but rather from the non-monotonic response of nucleation processes to static stress changes.

4.1.4 Dependence of aftershock rates on constitutive parameters *b* and *L*

Aftershock rates in the model of *Dieterich* [1994] do not depend on the rate and state parameter b and the characteristic slip L. In the continuum models presented here, aftershock rates show some dependence on parameters b and L for cases that exhibit deviations from Dieterich's model. For nucleation processes due to weaker patches, aftershock rates depend on the ratio a/b and on the size of the weaker patch. Changing b while keeping a

fixed would change the ratio a/b, while changing L would change the size of the nucleation zone and hence its relation to the size of the weaker region. For nucleation processes due to rheological transitions, the value of b affects the height of the delayed peak in aftershock rates, while decrease in L results in a shorter average time interval between earthquake nucleation at the same location, which can lead to more rapid initiation of seismic quiescence after a period of aftershocks.

4.2 Aftershock rates due to nonuniform stress changes in the model with rheological transition

How would the delayed peaks in aftershock rates that we observe for the model with rheological transition superimpose for nonuniform stress changes due to the distance from the mainshock? To answer this question, let us consider a population of nucleation sites uniformly distributed along the rheological transition and perturbed by shear stress change due to slip at a circular asperity (i.e., an area of large coseismic slip) located just above the transition (Figure 4.5). The population of nucleation sites along the transition experiences nonuniform stress step $\Delta\tau$ that can be approximated by [*Dieterich*, 1994]:

$$\Delta\tau \;=\; -\Delta\tau_{\mathrm{drop}}\left[\left(1-\frac{c^3}{[(c+h)^2+d^2]^{3/2}}\right)^{-1/2}-1\right] , \tag{4.2}$$

where $\Delta\tau_{\mathrm{drop}}$ is the stress drop in the asperity, c is the asperity radius, h is the distance from the asperity edge to the transition, and d is the distance along the transition, with $d = 0$ corresponding to the point directly below the hypocenter. In our example, $\Delta\tau_{\mathrm{drop}} = 10$

MPa, $c = 0.70$ km, and $h = 0.15$ km.

We would like to determine aftershock rates due to a population of nucleation sites uniformly distributed along the segment $[-A/2, A/2]$ of the transition. Each nucleation site is governed by the nucleation process of Case 4. We divide the segment into subsegments A_i, $i = 1, 2, ...$, such that the change of the stress step within each subsegment is 0.25 MPa. We assume that the stress step within each subsegment is constant and equal to the stress step at the center of the subsegment. The aftershock rate R_i/r for each subsegment A_i is determined using the approach developed in this Chapter. The overall aftershock rate can then be obtained as the weighted sum:

$$\frac{R}{r} = \sum_i \frac{R_i}{r} \frac{A_i}{A} \,. \tag{4.3}$$

In our example, $A/2 = 1.4$ km, which corresponds to selecting nucleation sites located approximately within one asperity radius from the edge of the mainshock. The computed aftershock rate shows a power-law decay with time for about one year, and then quiescence (Figure 4.6A, dotted line). Evidence of turnoff of aftershock activity was found at the base of the seismogenic zone near the M6.2 1984 Morgan Hill earthquake [*Tian and Rubin*, 2005; *Y. Tian, personal communication*, 2005]. In that case, aftershocks followed Omori's law for several months and then disappeared (Figure 4.6B,C). This is qualitatively similar to our computed aftershock rate (Figure 4.6A). We emphasize that the correspondence is only qualitative; for example, we use a vastly simplified model of the mainshock. Stress changes due to a realistic mainshock may be quite heterogeneous locally, and direct quantitative comparison between models and observations would require a more detailed analysis.

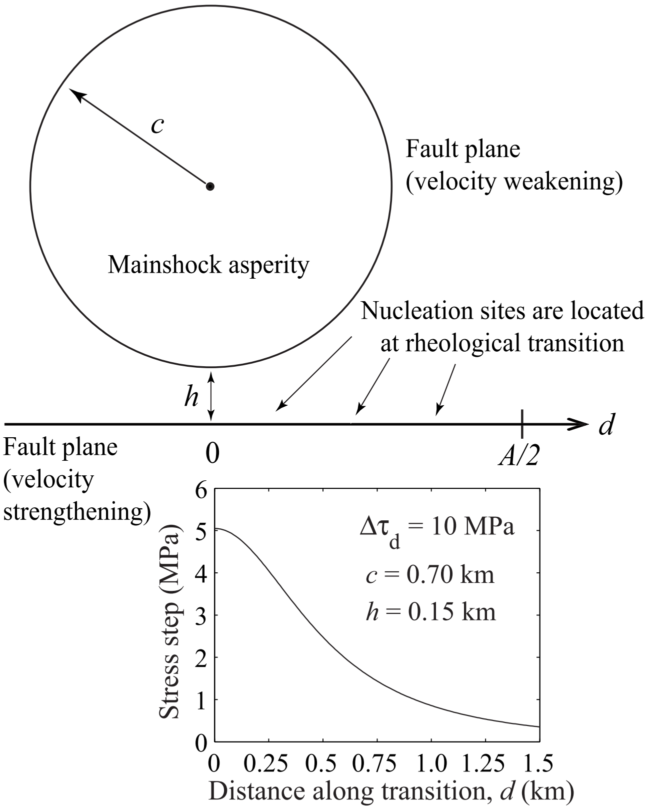

Figure 4.5: Model for estimating aftershock rates due to a population of nucleation sites located along a segment of rheological transition perturbed by a mainshock asperity. Due to the distance from the asperity, the nucleation sites along the segment experience a nonuniform stress step. The top panel illustrates the fault plane with a circular asperity of radius c and stress drop $\Delta\tau_d$ that imposes a variable static stress step on the nucleation sites located along the transition shown by the horizontal axis. d measures the distance along the transition. Variation of static stress change with d for c = 0.70 km, h = 0.15 km, and $\Delta\tau_d$ = 10 MPa is shown in the bottom panel. The segment $[-A/2, A/2]$ over which aftershock rates are sought is separated into sub-regions of approximately constant stress steps as discussed in the text.

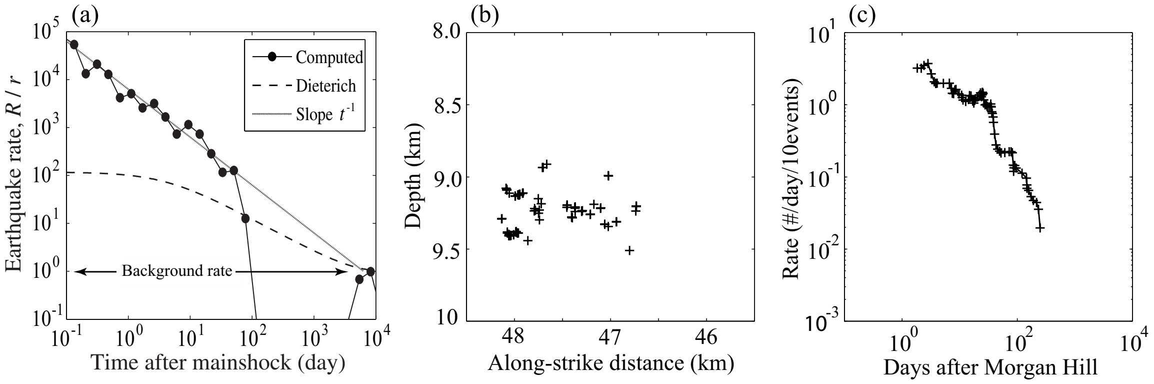

Figure 4.6: (A) Aftershock rates computed for the nonuniform static stress change and a population of nucleation sites located along the rheological transition (Figure 4.5). Dots represent the aftershock rates based on the model with rheological transition. The aftershock rate based on *Dieterich* [1994], for the same friction and stress parameters, is shown by the dashed line. The slope of t^{-1} is plotted for reference. This model produces Omori's law in a limited time period followed by seismic quiescence. For the period of the power-law decay of aftershocks, this model produces much higher aftershock rates than predicted by the model of *Dieterich* [1994]. (B) and (C) From *Tian and Rubin* [2005], courtesy of Y. Tian. A cluster of the 1984 Morgan Hill aftershocks occurred at a depth appropriate for rheological transition. The cross-sectional view of one multiplet of aftershocks is shown in panel B. Panel C gives the observed seismicity rate vs. time. The multiplet approximately followed Omori's law, but seismicity terminated about one year after the Morgan Hill earthquake. This behavior is qualitatively similar to that of the computed aftershock rates in panel A.

If the aftershock rate in our model were interpreted using the results of *Dieterich* [1994], the parameter $a\bar{\sigma}$ would be significantly underestimated. To find the aftershock rate based on *Dieterich* [1994], we use the weighted sum (4.3) with R_i/r given by the analytical formula (4.12), which results in much smaller rates *Dieterich* [1994] (Figure 4.6A, dashed line). To match the numerically computed aftershock rate, we need to use 10 times smaller $a\bar{\sigma}$ in (4.12) (and also 20 times smaller stressing rate $\dot{\tau}$, to match the slope). While this does not fully close the gap between the expected and observed values of $a\bar{\sigma}$, it is a step in the right direction. This example shows that application of spring-slider solutions to earthquakes that potentially have more complex nucleation processes, such as the ones occurring at rheological transitions, may lead to errors in estimating rate and state parameters.

Similar superposition of aftershock peaks, leading to Omori's law in a limited time period, should arise in a situation with a constant stress step $\Delta\tau$ but applied to a population of nucleation sites with varying values of $a\bar{\sigma}$. For example, Cases 4 and 5 have the same $\Delta\tau$ but Case 5 has ten times smaller $a\bar{\sigma}$, and, as a result, the aftershock rate peak is much larger in Case 5 and occurs much earlier. These results suggest that it might be difficult to observe distinct peaks in aftershock rates on natural faults, because they would be obscured by nonuniform stress changes and/or variable values of $a\bar{\sigma}$. However, the model with rheological transition and the associated complex aftershock response may explain deviations from Omori's law in appropriately chosen subsets of aftershocks.

4.3 The link between aftershock rates and slip-velocity history of unperturbed nucleation processes

The unperturbed slip-velocity evolution in our models can be used to qualitatively capture the numerically computed aftershock rates. Let us denote slip velocity in a given nucleation process by $V_g(T)$. Each point of the nucleation zone in a continuum model has its own slip-velocity evolution, so $V_g(T)$ denotes a characteristic measure. For example, for the model with a weaker patch, we take slip velocity in the middle of the nucleation zone as $V_g(T)$. Let us assume that, after the perturbation, $V_g\theta/L \gg 1$ in the nucleation zone for all subsequent times. Then the new time to instability can be found from the analysis of *Dieterich* [1994]:

$$f(T) \; = \; t_a \ln\left(\frac{\dot{\tau}}{H\bar{\sigma}V_g(T)\exp\left(\Delta\tau/(a\bar{\sigma})\right)} + 1\right) \text{ for } \dot{\tau} \neq 0, \tag{4.4}$$

where $H = -k/\bar{\sigma} + b/L$ and k is the effective stiffness of the nucleation zone. With each original time to instability T, we can associate slip velocity $V_D(T)$ that the nucleation process from *Dieterich* [1994] needs to have in order to nucleate an instability in time T:

$$T \; = \; t_a \ln\left(\frac{\dot{\tau}}{H\bar{\sigma}V_D} + 1\right) \text{ for } \dot{\tau} \neq 0. \tag{4.5}$$

Combining (4.4) and (4.5), we can eliminate H and get:

$$f(T) = t_a \ln\left(\frac{\exp\left(\dfrac{T}{t_a}\right) - 1}{\dfrac{V_g(T)}{V_D(T)}\exp\left(\dfrac{\Delta\tau}{a\bar{\sigma}}\right)} + 1\right) \text{ for } \dot{\tau} \neq 0. \tag{4.6}$$

Similarly, one obtains

$$f(T) = \frac{T}{\dfrac{V_g(T)}{V_D(T)} \exp\left(\dfrac{\Delta\tau}{a\bar{\sigma}}\right)} \text{ for } \dot{\tau} = 0. \tag{4.7}$$

Equations (4.6)-(4.7) give an analytical approximation of $f(T)$ that can be used to approximately compute aftershock rates. For $V_g(T) = V_D(T)$, we have a nucleation process that follows the model of *Dieterich* [1994], and in that case we recover (4.10).

Figure 4.7 shows comparison, for Cases 2, 4, and 5, between the aftershock rates computed based on numerous calculations with stress perturbations and the aftershock rates obtained based on the approximate formula (4.6). We use the following unperturbed slip-velocity histories as $V_g(T)$: at the center of the nucleation zone for Case 2, at $z = -5$ m for Case 4, and at $z = -20$ m for Case 5. Since Case 1 has the same friction parameters as Cases 2 and 4, Case 3 has the same friction parameters as Case 5, and the aftershock rates for Cases 1 and 3 generally agree very well with those based on *Dieterich* [1994], we use the unperturbed slip velocity at the center of the nucleation zone in Cases 1 and 3 as $V_D(T)$. Note that Cases 1 and 3 have about three times higher stressing rate (0.255 MPa/yr) than Cases 4 and 5 (0.087 MPa/yr); hence we rerun the simulations for Cases 1 and 3 with the correspondingly smaller value of the loading rate V_{L}.

The semianalytical aftershock approximation qualitatively captures the computed aftershock rates for both models, for different stress steps and rate and state parameters (Figure 4.7). The overall agreement for the model with a weaker patch (Figure 4.7A) is better than for the model with rheological transition (Figure 4.7B). This is not surprising,

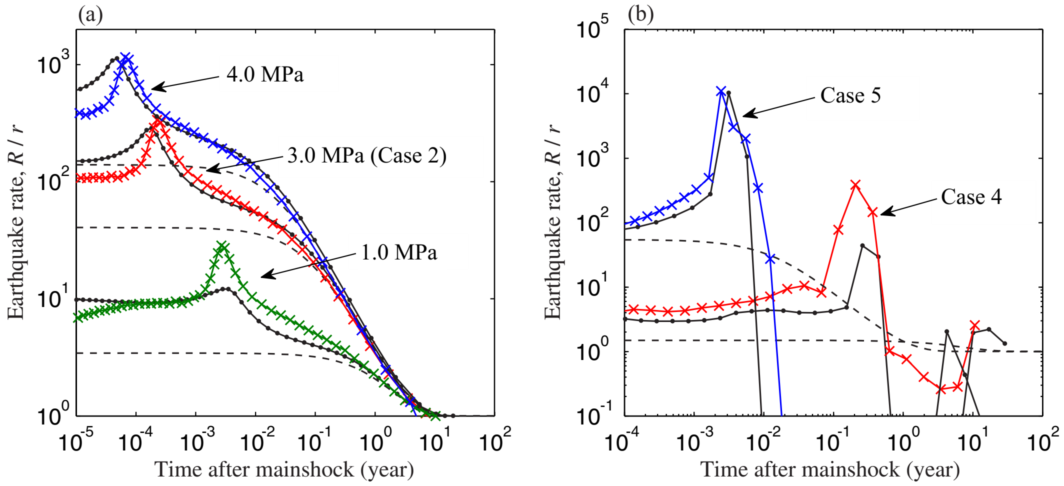

Figure 4.7: Comparison of the aftershock rates computed using (i) simulations with stress perturbations (solid dotted lines), (ii) the semi-analytical estimate based on equation (4.6) (lines with crosses), and (iii) analytical results of *Dieterich* [1994] (dashed lines). Panel A: Aftershock rates for Case 2 and three different values of the stress step ($\Delta\tau = 1.0$, 3.0, 4.0 MPa). Panel B: Aftershock rates for Cases 4 and 5. In all cases, the semi-analytical estimate qualitatively matches the main features of the computed aftershock rates. The analytical results of *Dieterich* [1994] are significantly different.

as the semianalytical procedure is constructed assuming that the nucleation behavior after perturbation is well approximated by spring-slider models, and the model with a weaker patch compares much better with the results of spring-slider models than the model with rheological transitions (sections 3.3 and 4.1). Moreover, it is difficult to choose a representative slip velocity V_g for nucleation processes in the model with rheological transition: the nucleation zone is connected to the creeping region, and hence its middle of extent is not easy to define, plus slip velocity within the nucleation region varies with distance in a non-symmetric way. While slip velocity of most points gave qualitatively similar results, reproducing a pronounced peak and the following quiescence, the agreement in terms of timing and amplitude of those features was not as good for most points as shown in Figure 4.7B.

The results suggest that (i) aftershock rates are linked to the unperturbed evolution of slip velocity, and (ii) once the differences in slip-velocity history are accounted for, the spring-slider approximation can qualitatively match the aftershock rates, at least for the cases considered in this Chapter. To use the semi-analytical procedure predictively, i.e., without having the computed aftershock rates for comparison, one needs to establish an independent way of determining a representative slip velocity of a nucleation process. Whether this is possible to do for any nucleation process remains a question for future study.

4.4 The relation between aftershock rates and the validity of the state-evolution assumption

The aftershock model of *Dieterich* [1994] is based on nucleation processes governed by rate and state friction with the state-evolution assumption $V\theta/L \gg 1$. Let us consider the validity of the assumption for nucleation processes in our models and how it relates to similarities and differences between our numerically computed aftershock rates and the results of *Dieterich* [1994].

4.4.1 Model with a weaker patch

Panels G-I in Figure 4.2 show $V\theta/L$ as a function of the original time to instability T for two representative points within the nucleation zone. In this model, $V\theta/L$ varies for different locations within the nucleation zone but we find that a large part of the nucleation zone around its middle behaves similarly. In the following, we take the behavior of the middle point of the nucleation zone as being representative of the entire nucleation process. The temporal correspondence between $V\theta/L$ in panels G-I and aftershock rates in panels D-F can be established by using the panels A-C: the horizontal axis in panels G-I corresponds to the vertical axis in panels A-C, and the horizontal axis in panels A-C corresponds to the horizontal axis in panels D-F.

The first important observation is that some of the nucleation sites considered in our aftershock rate calculations are characterized by $V\theta/L < 1$ and even $V\theta/L \ll 1$, not $V\theta/L \gg 1$ as assumed in *Dieterich* [1994]. As an example, consider Case 3. Panel I shows that all nucleation sites with original times to instability larger than 2 years have $V\theta/L < 1$, and, for most of them, $V\theta/L \ll 1$. Nonetheless, panel F shows that these rates match very well the model of *Dieterich* [1994], which assumes $V\theta/L \gg 1$ at all times. This observation is consistent with the findings of *Gomberg et al.* [2000] for spring-slider models. To understand why the formulae of *Dieterich* [1994] still work in this situation, let us consider the aftershock behavior of nucleation zones that are far from failure. A shear stress step increases slip velocities by a factor of $\exp\left[\Delta\tau/(a\bar{\sigma})\right]$. Two scenarios can be distinguished in terms of the resulting aftershock rates.

Scenario 1: Slip velocities in the nucleation zone are small enough before the stress step so that the condition $V\theta/L \ll 1$ holds both before and after the stress step. In this situation, the effect of stress step $\Delta\tau$ on the nucleation site is approximately equivalent to the effect of gradual loading $\dot{\tau}$ over time $\Delta t = \Delta\tau/\dot{\tau}$ (appendix 4.8, section 4.8.1), with Δt independent of T. Hence we approximately have $T - f(T) = \Delta\tau/\dot{\tau} =$ constant (or "constant clock advance", in the terminology of *Gomberg et al.* [1998] who also identified this scenario) and $R/r = dT/df = 1$. This explains the origin of the aftershock rates equal to the background rate for Case 3 (time period marked (1) in panel F). Note that Cases 1 and 2 (panels D and E) do not have time periods during which the rates are equal to the background rate. For those Cases, the nucleation processes at all times have such slip velocities that $V\theta/L \gg 1$ after the stress step.

Scenario 2: Slip velocities in the nucleation zone are such that $V\theta/L \ll 1$ before the stress step but $V\theta/L \gg 1$ after the stress step and until the instability. The analysis of this scenario (appendix 4.8, section 4.8.2) predicts $R/r = 1/[1 - \exp(-f/t_a)]$. For $f \ll t_a$, one has $R/r = t_a/f$, which shows a power law decay of the aftershock rate with the time f after the mainshock. For $f \gg t_a$, one gets $R/r = 1$ and the aftershock rate is equal to the background rate. The corresponding parts of the aftershock rates in panels D and F are marked as time periods (2).

For nucleation zones close to failure, which we define as those zones that have reached $V\theta/L \gg 1$, subsequent deviations of $V\theta/L$ from the condition $V\theta/L \gg 1$ create significant discrepancies in aftershock rates relative to the results of *Dieterich* [1994]. This is because such deviations reflect significant differences in slip-velocity histories, and the importance of differences in slip velocity has already been shown (section 4.3). As an example, let us consider Case 2 of heterogeneous effective normal stress within the nucleation zone. Panel E of Figure 4.2 shows differences between the computed aftershock rates and the prediction (4.12) of *Dieterich* [1994] for times shortly after the mainshock. The nucleation zones that contribute to these differing aftershock rates have new times to instability

$f(T) < 10^{-2}$ years (panel E) and original times to instability $T < 1$ years (panel B), with the corresponding values of $V\theta/L$ in the middle of the nucleation zone that change from being much larger than 1 to the value of about 1.5. A value of $V\theta/L$ close to 1 violates the assumption $V\theta/L \gg 1$ and causes the corresponding deviation in aftershock rates. Case 1 has a similar deviation in aftershock rates from the analytical solution (4.12), for times after mainshock smaller than 10^{-7} years (the inset in panel D). That deviation is also related to values of $V\theta/L$ being close to 1 in the middle of the nucleation zone during the very end of the nucleation process, for original times to instability that are outside of the time range shown in panel G of Figure 4.2. In Case 3, however, as the end of the unperturbed nucleation is approached, the condition $V\theta/L \gg 1$ stays valid. As the result, the corresponding aftershock rates (panel F) show close agreement with the model of *Dieterich* [1994]. Note that the behavior of $V\theta/L$ for times close to instability is consistent with the study of *Rubin and Ampuero* [2005].

The discrepancy between the computed aftershock rates and the ones based on the model of *Dieterich* [1994] right after the mainshock can be estimated using appropriate assumptions in the spring-slider model (appendix 4.8, section 4.8.3). For Cases 1 and 2 (panels D and E of Figure 4.2), the simulated aftershock rates are 3.2 and 3.8 times larger than those predicted by the model of *Dieterich* [1994], while the two estimates derived in section 4.8.3 give factors of 2.7 and 3.5, matching the discrepancy relatively well.

4.4.2 Model with rheological transition

Panels G-H in Figure 4.3 illustrate the time evolution of $V\theta/L$ for the unperturbed nucleation processes of Cases 4 and 5 (Case 6 uses the unperturbed process of Case 4, but with a different stress step). The panels show that condition $V\theta/L \gg 1$ becomes valid and then violated relatively early in the earthquake cycle relative to the model with a weaker patch. Consistently, the aftershock rates are significantly different from the model of *Dieterich* [1994] (panels D-F, Figure 4.3). The variations in $V\theta/L$ are due to penetration of slow slip from the nearby velocity-strengthening region. Note that the variations in $V\theta/L$ make scenarios 1 and 2 of section 4.4.1 inapplicable to this model, as condition $V\theta/L \ll 1$ holds for some points in the nucleation zone but not others, even for nucleation zones with large original times to instability; in particular, $V\theta/L \gg 1$ at the tip of the propagating slow slip.

Hence, in both models, similar behavior of $V\theta/L$ causes similar effects in terms of aftershock rates. However, the history and spatial distribution of $V\theta/L$ is different in the two models, resulting in qualitatively different aftershock behavior.

4.5 Conclusions

Using two different fault models, we have simulated several plausible scenarios of spontaneous earthquake nucleation (Chapter 3), investigated their response to static shear stress steps, and inferred the corresponding aftershock rates. Overall, nucleation processes at weaker patches are characterized by slip-velocity evolution and aftershock rates similar to spring-slider models, although there are notable deviations. Nucleation processes at rheological transitions and the corresponding aftershock rates are significantly different.

For both models, unperturbed slip-velocity history of nucleation zones and the resulting aftershock rates are closely linked. In the model with a weaker patch, slip velocity in nucleation zones is very low for most of the interseismic period, increasing approximately exponentially in response to the approximately constant stressing rate due to tectonic loading. This is similar to the behavior of spring-slider models and, in particular, to the analytical solution of *Dieterich* [1994]. Aftershock rates created by such far-from-failure nucleation zones closely follow the model of *Dieterich* [1994], despite the fact that the condition $V\theta/L \gg 1$ is violated for such zones. Nucleation processes due to rheological transitions behave very differently in the interseismic period, due to penetration of slow slip from the nearby velocity-strengthening region and the associated time- and space-dependent variations in slip velocity and shear stress. As the result, neither $V\theta/L \gg 1$ (as in *Dieterich* [1994]) nor $V\theta/L \ll 1$ (as in the model with a weaker patch) holds throughout the nucleation zone in the interseismic period. That is why the model with rheological transition results in qualitatively different aftershock rates. Another type of deviation of aftershock rates from the model of *Dieterich* [1994], evident in both models, occurs due to nucleation zones close to instability for the parameter range $a/b \gtrsim 0.5$, consistently with the analysis of *Rubin and Ampuero* [2005].

In the model with rheological transition, the response of nucleation processes to static stress changes is complex and non-monotonic. For example, it is commonly assumed that favorable static stress changes should lead to earthquakes occurring sooner. We find that positive shear stress steps can *delay* the time to instability by inducing aseismic transients that relieve stress in the nucleation zone and postpone seismic slip. Recent observations have documented complex interactions of seismic and aseismic slip [*Schwartz and Rokosky*, 2007, and references therein], and our findings provide one more instance where such interactions may be important. If such behavior is common on natural faults, at least in certain environments, it may partially explain the cases of poor correlation between static stress changes and aftershock occurrence.

Aftershock rates based on nucleation processes at rheological transitions exhibit pronounced peaks and seismic quiescence. This behavior is qualitatively different from that of nucleation processes due to weaker patches, from Omori's law, and from the results for spring-slider models. The behavior may explain faster decay of aftershock activity than that given by Omori's law with $p = 1$ and delayed seismic quiescence reported in several observational studies [e.g., *Daniel et al.*, 2008, and references therein]. We have shown that superposition of such responses for spatially variable stress steps can result in Omori's law for a certain period of time followed by seismic quiescence, the behavior supported by observations [*Tian and Rubin*, 2005]. If this computed aftershock rate were interpreted using the model of *Dieterich* [1994], the inferred values of $a\bar{\sigma}$ would be an order of magnitude smaller than the ones used in the simulations. The result suggests that complexity of rate and state nucleation processes may be partially responsible for the discrepancy between the values of $a\bar{\sigma}$ predicted based on laboratory studies and inferred from aftershock observations based on the model of *Dieterich* [1994].

The differences in nucleation processes and aftershock rates between the continuum and spring-slider models arise due to the presence of heterogeneity, either in normal stress or in friction properties. Hence the effect of fault heterogeneity on aftershock phenomena needs to be systematically examined. Note that the heterogeneity discussed here is the local one that affects nucleation processes at individual aftershock sites. Aftershock sequences are undoubtedly affected by another kind of heterogeneity, where different nucleation sites may have different friction properties, stress conditions, stressing rates, etc., and hence follow different nucleation processes. Our approach can be used to study certain aspects of such “global” heterogeneity by simulating a number of nucleation processes with different desired friction properties and stress conditions, determining their responses to stress perturbations, and combining those responses into one aftershock rate.

This study employs the aging form of the state-variable evolution equation. Other formulations have been proposed, as discussed in Chapter 1. Based on preliminary results with the slip law, we predict that the main findings of this work would be qualitatively similar for other rate and state formulations, in the following sense. Nucleation in relatively homogeneous situations would still produce aftershock rates largely consistent with spring-slider models. Nucleation at rheological transitions would still exhibit peaks in aftershock activity followed by quiescence, since this response mostly comes from the slow slip penetrating from the nearby creeping region, the feature that would not qualitatively change for other rate and state formulations.

Following earlier studies, we have assumed a population of nucleation sites that would result in a uniform background rate if left unperturbed. That assumption implies a certain distribution of initial conditions over the population at the time of the stress step and affects the resulting aftershock rates. But parts of aftershock sequences may result from nucleation sites created by coseismic processes such as bulk damage. Such nucleation sites would not have contributed to the background rate, and it may be possible to account for them by considering a different distribution of initial conditions over the population of nucleation sites in the developed approach.

The qualitative differences we find between the presented models indicate that more studies are needed to understand which nucleation scenarios dominate on natural faults, how they respond to static stress changes, and whether spring-slider models can provide an adequate interpretation of that response. Natural faults may contain rate and state nucleation zones developing under a number of conditions, in which case the response of faults to static stress changes would combine a number of models of the kind considered in this work.

Given that rate and state friction laws have been successfully used to explain a number of earthquake phenomena and that mainshocks cause static stress changes, it is reasonable to assume that at least some, and perhaps most, of aftershocks are caused by static triggering of rate-and-state nucleation processes. At the same time, a number of studies have proposed models of aftershocks based entirely on other mechanisms, as discussed in Chapter 1. The developed approach enables us to study the combined effect of two or more mechanisms on aftershock rates. For example, the response of rate-and-state nucleation to static stress changes can be combined in our models with the effect of increased loading rate due to aseismic processes, through prescribed variations in the loading rate. Such combined models would help investigate the relative importance of different aftershock-producing mechanisms.

4.6 Appendix: The model of aftershocks in *Dieterich* [1994]

In the study of *Dieterich* [1994], each nucleation site was assumed to proceed through the slip-stress history that would occur in a spring-slider system with the aging form (1.1-1.2) of rate and state friction. In that model, frictional sliding occurs on the block-substrate interface, which serves as the model of a fault. The spring of stiffness k provides elastic interactions. The governing equation for slip $\delta(t)$ is given by

$$\tau^o + \dot{\tau} t - k\delta \ = \ \bar{\sigma} \left[\mu_0 \ + \ a \ln\left(\frac{V}{V_0}\right) \ + \ b \ln\left(\frac{V_0\,\theta}{L}\right)\right] \ , \tag{4.8}$$

where the left-hand side gives shear stress on the interface with inertial effects ignored, the right-hand side gives the rate and state frictional resistance of the interface, τ^o is shear stress that would act on the interface if it were constrained against slip and $\dot{\tau}$ is the stressing rate applied directly to the interface. The rate and state formulation is simplified by assuming that, during nucleation, slip accelerates fast enough for the state variable to be significantly larger than its steady-state value, so that $V\theta/L \gg 1$. The assumption $V\theta/L \gg 1$ leads to the following state evolution:

$$\frac{d\theta}{d\delta} = -\frac{\theta}{L} \quad \text{and thus } \theta = \theta_{\text{ref}} \exp\left(-\frac{\delta - \delta_{\text{ref}}}{L}\right) \ , \tag{4.9}$$

where δ_{ref} and θ_{ref} are reference values.

In this model, the time to instability T can be obtained analytically [*Dieterich*, 1994]:

$$T = \frac{a\bar{\sigma}}{\dot{\tau}} \ln\left(\frac{\dot{\tau}}{H\bar{\sigma}V} + 1\right) \ , \quad \text{for } \ \dot{\tau} \neq 0 \ , \tag{4.10}$$

$$T = \frac{a}{HV} \ , \quad \text{for } \ \dot{\tau} = 0 \ , \tag{4.11}$$

where $H = -k/\bar{\sigma} + b/L$. A population of nucleation sites that results in a uniform background rate r is created by assigning the appropriate distribution of initial slip velocity V to the population. A positive shear stress step $\Delta\tau$ increases the initial slip velocity by a factor of $\exp[\Delta\tau/(a\bar{\sigma})]$, changing the time to instability for each nucleation site and resulting in a different earthquake rate R (aftershock rate) given by:

$$\frac{R}{r} = \frac{1}{[\exp\left(-\Delta\tau/(a\bar{\sigma})\right) - 1] \exp\left(-t/t_a\right) + 1} \ , \tag{4.12}$$

where $t_a = a\bar{\sigma}/\dot{\tau}$ and constant stressing rate $\dot{\tau}$ is assumed before and after the stress step. *Dieterich* [1994] also considered scenarios with variable stress steps and stressing rates.

From expression (4.12), this model has two parameters: $\Delta\tau/(a\bar{\sigma})$ and $t_a = a\bar{\sigma}/\dot{\tau}$. Figure 4.8 illustrates the resulting aftershock rates and shows that t_a is related to the aftershock duration, since the earthquake rate becomes close to the background rate for $t \geq t_a$. From (4.12), $R/r = 1$ for $t \gg t_a$. For $t \ll t_a$, $\exp(-t/t_a) \approx (1 - t/t_a)$ and from (4.12):

$$R = \frac{K}{(c+t)^p} \ , \quad p = 1, \tag{4.13}$$

$$K = \frac{rt_a}{1 - \exp\left(-\Delta\tau/(a\bar{\sigma})\right)} \ , \quad c = \frac{t_a}{\exp\left(\Delta\tau/(a\bar{\sigma})\right) - 1} \ . \tag{4.14}$$

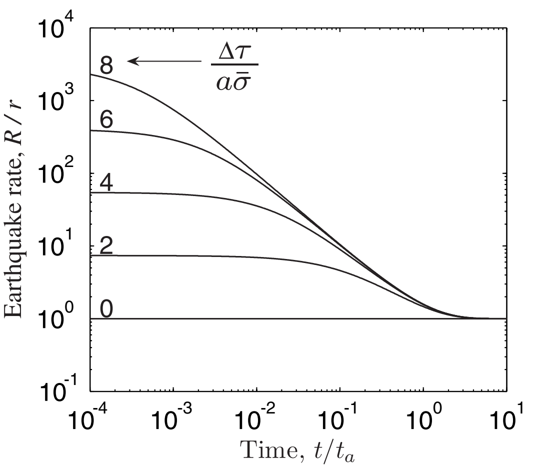

Figure 4.8: Aftershock rates for the analytical solution of *Dieterich* [1994] given by equation (4.12). The aftershock rate R is normalized by the background rate r, and the time t after the mainshock is normalized by the aftershock duration t_a. Each curve is computed for a normalized stress step, $\Delta\tau/(a\bar{\sigma})$, with the indicated value. Adapted from Figure 2 of *Dieterich* [1994].

Hence the model of *Dieterich* [1994] interprets parameters K and c of Omori's law, which were originally introduced as empirical constants. The time interval in which the aftershock rates in this model follow the power law decay of aftershocks depends on the values of $\Delta\tau/(a\bar{\sigma})$ and t_a. For times right after the instability, we have $\exp(-t/t_a) \approx 1$ and $R/r = \exp[\Delta\tau/(a\bar{\sigma})]$. This "plateau" or constant aftershock rate right after the mainshock is shorter for larger values of $\Delta\tau/a\bar{\sigma}$ (Figure 4.8).

Since static stress changes $\Delta\tau$ due to earthquakes are relatively well constrained, aftershock observations can be used to constrain the product $a\bar{\sigma}$. For the model to be consistent with observations, $a\bar{\sigma}$ has to be of the order of 0.01-0.1 MPa [*Toda et al.*, 1998; *Belardinelli et al.*, 1999]. Larger values of $a\bar{\sigma}$, of order 1 MPa, are predicted by laboratory values of a (of order 0.01) and $\bar{\sigma}$ comparable to overburden minus hydrostatic pore pressure at typical seismogenic depths (of order 100 MPa). If aftershock production is dominated by static

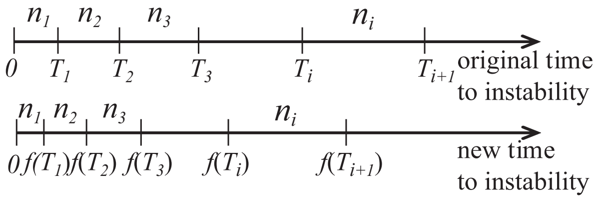

Figure 4.9: Schematics showing how the time to instability for each nucleation site in the population changes due to a stress step for a monotonic function $f(T)$. The top arrow represents the (original) time to instability T_i for the ($\sum_{k=1}^{i} n_k$)th nucleation site in the absence of perturbation, where n_i is the number of earthquakes between T_{i-1} and T_i. The bottom arrow shows the (new) time to instability $f(T_i)$ after the static stress step at time zero. The time to instability of each nucleation site changes, resulting in a different earthquake rate (aftershock rate).

stress triggering of preexisting nucleation sites, then, at least on parts of faults where aftershocks nucleate, either the direct effect coefficient a is much smaller than in the laboratory, or effective normal stress $\bar{\sigma}$ is abnormally low.

The dependence $f(T)$ for the model of *Dieterich* [1994] can be derived using the time-to-instability expression (4.11). With $V \exp\left[\Delta\tau/(a\bar{\sigma})\right]$ in (4.10) instead of V, we obtain:

$$f = \frac{a\bar{\sigma}}{\dot{\tau}} \ln\left(\frac{\dot{\tau}}{H\bar{\sigma}V\exp\left(\Delta\tau/(a\bar{\sigma})\right)} + 1\right) \ . \tag{4.15}$$

Solving (4.10) for $\dot{\tau}/(H\bar{\sigma}V)$ and substituting this quantity into (4.15), we find

$$f(T) = t_a \ln\left(\frac{\exp\left(T/t_a\right) - 1}{\exp\left(\Delta\tau/(a\bar{\sigma})\right)} + 1\right) \ . \tag{4.16}$$

where $t_a = a\bar{\sigma}/\dot{\tau}$. We use (4.16) for comparison with our simulations.

4.7 Appendix: Aftershock rate calculations

4.7.1 For monotonic response *f(T)*

We compute aftershock rates based on function $f(T)$ that gives the perturbed (or new) time to instability for a nucleation site with the unperturbed (or original) time to instability T (Figure 4.1B). Without the perturbation, the population of rate and state nucleation sites should produce earthquakes at a constant background rate r. Hence, if one considers discrete time intervals $[T_{i-1}, T_i], T_0 = 0, T_i \geq T_{i-1}, i = 1, 2, 3, ...$, with each of the intervals containing n_i earthquakes (Figure 4.9), then T_i and n_i have to satisfy the following relations:

$$r \;=\; \frac{n_1}{T_1 - T_0} \;=\; \frac{n_2}{T_2 - T_1} \;=\; ... \;=\; \frac{n_i}{T_i - T_{i-1}} \; . \tag{4.17}$$

If $f(T)$ is monotonic, then n_i earthquakes that would have occurred in the time interval $[T_{i-1}, T_i]$ before the perturbation occur in the time interval $[f(T_{i-1}), f(T_i)]$ after the perturbation (Figure 4.9). Hence the new earthquake rate R in each time interval is given by $R\,[f(T_{i-1}), f(T_i)] \;=\; n_i/(f(T_i) - f(T_{i-1}))$. Using (4.17), we obtain the normalized aftershock rate R/r as

$$\frac{R\,[f(T_{i-1}), f(T_i)]}{r} \;=\; \frac{T_i - T_{i-1}}{f(T_i) - f(T_{i-1})} \; , \tag{4.18}$$

or, in the limit of infinitely small lengths $(T_i - T_{i-1})$ of the time bins,

$$R/r \;=\; dT/df \; . \tag{4.19}$$

This procedure for computing the aftershock rate R/r for monotonic $f(T)$ is analogous to the one in *Gomberg et al.* [2000]. Using equation (4.19) with $f(T)$ for the model of *Dieterich* [1994], given by (4.16), provides an alternative way of deriving the analytical aftershock rates (4.12).

4.7.2 For nonmonotonic response *f*(*T*)

Expression (4.19) is valid only for monotonic functions $f(T)$, as it requires the existence of the inverse function $T(f)$. For nucleation processes at rheological transition, however, functions $f(T)$ turn out to be non-monotonic for all cases we have considered. As an illustration, consider $f(T)$ given in Figure 4.10. Aftershocks occurring in the time interval Δf come from nucleation sites that, without perturbation, would have produced earthquakes in *three* time intervals ΔT_1, ΔT_2, and ΔT_3. Thus, the aftershock rate in the time interval Δf in Figure 4.10 is given by

$$\frac{R}{r} = \left|\frac{\Delta T_1}{\Delta f}\right| + \left|\frac{\Delta T_2}{\Delta f}\right| + \left|\frac{\Delta T_3}{\Delta f}\right| . \tag{4.20}$$

To compute aftershock rates for a non-monotonic $f(T)$, we create time bins Δf equally spaced on the logarithmic scale. That is, we choose $\Delta f_j = f_j - f_{j-1}$, where $\log(f_j) - \log(f_{j-1}) = \log(f_j/f_{j-1})$ is the same for all j. For each f_j, we find the corresponding values of T_j by linearly interpolating discretely specified correspondence $T(f)$. Each f_j may have more than one corresponding T_j, or equivalently, each interval Δf_j may have several corresponding intervals $\Delta T_{j(k)}$. The aftershock rates can be obtained by adding the contribution of each $\Delta T_{j(k)}$ to the corresponding time bin Δf_j:

$$\left.\frac{R}{r}\right|_{\Delta f_j} = \sum_k \left|\frac{\Delta T_{j(k)}}{\Delta f_j}\right| . \tag{4.21}$$

This procedure allows us to compute aftershock rates for complicated non-monotonic responses that we observe in the model with rheological transition.

4.8 Appendix: Aftershock rates for simplified scenarios

In the model of *Dieterich* [1994] (appendix 4.6), it is assumed that zones nucleating earthquakes always satisfy the condition $V\theta/L \gg 1$. In our simulations, nucleation zones that contribute to aftershock response do not always satisfy that condition (section 4.4). To understand the contribution of such zones to aftershock rates, we consider here several simplified scenarios motivated by our simulations, using the spring-slider model (4.8).

4.8.1 Scenario 1: Nucleation zones with $V\theta/L \ll 1$ before and after the perturbation

Our simulations in the model with a weaker patch show that, for much of the interseismic period, $V\theta/L \ll 1$ in the nucleation zone because of the near-zero slip velocities V. Let us consider such a nucleation site at a time t_{ref}, approximating it as a spring-slider system with slip δ_{ref}, slip velocity V_{ref}, state variable θ_{ref}, and loading stress τ^o_{ref} so that

$$\tau^o_{\text{ref}} - k\delta_{\text{ref}} = \bar{\sigma}\left[\mu_0 + a\ln\left(V_{\text{ref}}/V_0\right) + b\ln\left(V_0\theta_{\text{ref}}/L\right)\right] . \tag{4.22}$$

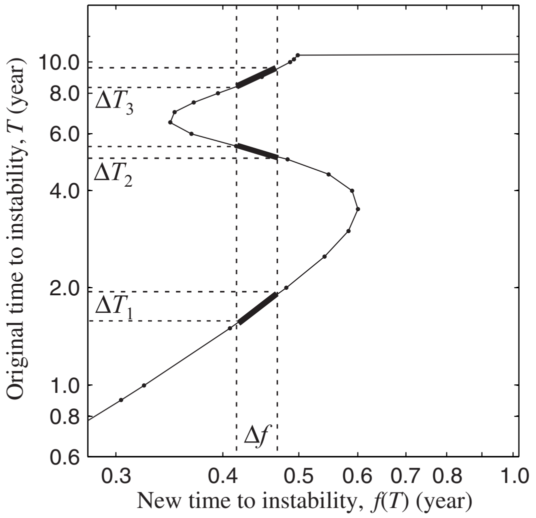

Figure 4.10: An example of a non-monotonic $f(T)$. This is an actual response observed in the model with rheological transition for Case 4. The data shown here is taken from the rectangle in panel A of Figure 4.3. The bold lines on the curve represent three time intervals ΔT_1, ΔT_2 and ΔT_3 that contribute to the aftershock rate in the interval Δf.

Since $V\theta/L \ll 1$, the evolution of state variable can be simplified to $\theta(t) = \theta_{\text{ref}} + (t - t_{\text{ref}})$, and near-zero slip velocities V imply that we can approximately write $\delta(t) = \delta_{\text{ref}}$. The governing equation (4.8) becomes

$$\begin{aligned} &\tau^o_{\text{ref}} - k\delta_{\text{ref}} + \dot{\tau}(t - t_{\text{ref}}) \\ &= \bar{\sigma}\left[\mu_0 + a\ln\left(\frac{V}{V_0}\right) + b\ln\left(\frac{V_0\left(\theta_{\text{ref}} + (t - t_{\text{ref}})\right)}{L}\right)\right] \ . \end{aligned} \tag{4.23}$$

From the last two equations, we find the following time evolution of slip velocity:

$$V(t) = V_{\text{ref}} \exp\left(\frac{t - t_{\text{ref}}}{t_a} - \frac{b}{a}\ln\left[1 + \frac{t - t_{\text{ref}}}{\theta_{\text{ref}}}\right]\right) \ . \tag{4.24}$$

In (4.24), slip velocity increases approximately exponentially with time, which is the same functional dependence as in the model of *Dieterich* [1994] for times far from instability.

The behavior is similar because, for times far from instability, slip velocities and hence slip accumulation are very small, the state variable evolves slowly, and the assumption regarding $V\theta/L$ does not make much difference.

After positive static stress step $\Delta\tau$ at time $t > t_{\mathrm{ref}}$, slip velocity V abruptly increases to $V\exp\left[\Delta\tau/(a\bar{\sigma})\right]$. In the nucleation process without perturbation, such larger slip velocity would be achieved only after time Δt such that $V(t)\exp\left[\Delta\tau/(a\bar{\sigma})\right] = V(t+\Delta t)$. Using equation (4.24) (which is applicable both before and after the perturbation, due to the assumption that $V\theta/L \ll 1$ holds for both stages), with the logarithmic term under the exponential ignored in comparison with the linear term, this leads to $\Delta t = \Delta\tau/\dot{\tau}$, consistently with the time advance for Coulomb-like behavior [*Gomberg et al.*, 2000; *Perfettini et al.*, 2003]. In the same time period, the state variable would change as well but if we ignore that (since the change in state variable is linear with time while the change of slip velocity is exponential), then the effect of the stress step is to essentially advance the nucleation process by a constant time $\Delta\tau/\dot{\tau}$. Using $R/r = dT/df$ with $f(T) = T - \Delta\tau/\dot{\tau}$, we find $R/r = 1$. Hence nucleation sites considered in this scenario, taken by themselves, result in the aftershock rate equal to the background rate. Their time to instability is advanced, but by the same amount, so there is no pileup of the resulting earthquakes.

4.8.2 Scenario 2: Nucleation zones with $V\theta/L \ll 1$ before the perturbation but $V\theta/L \gg 1$ after the perturbation

In this scenario, equations (4.22)-(4.24) continue to be valid. Let T_{ref} be the time to instability corresponding to time t_{ref} and T be the time to instability corresponding to time

$t > t_{\text{ref}}$. Then $t - t_{\text{ref}} = T_{\text{ref}} - T$ and equation (4.24) can be rewritten as:

$$V(T) = V_{\text{ref}} \exp\left(\frac{T_{\text{ref}} - T}{t_a} - \frac{b}{a}\ln\left[1 + \frac{T_{\text{ref}} - T}{\theta_{\text{ref}}}\right]\right) . \tag{4.25}$$

Due to stress step $\Delta\tau$ at time $t > t_{\text{ref}}$, slip velocity abruptly increases to $V(T)\exp\left[\Delta\tau/(a\bar{\sigma})\right]$ and, in this scenario, $V\theta/L$ becomes much larger than 1. The new time to instability can be found from equation (4.10):

$$\begin{aligned} f(T) = t_a \ln\Biggl(1 + \frac{\dot{\tau}}{H\bar{\sigma}V_{\text{ref}}} \\ \exp\Biggl(\frac{\dot{\tau}(T - T_{\text{ref}}) - \Delta\tau}{a\bar{\sigma}} + \frac{b}{a}\ln\left[1 + \frac{T_{\text{ref}} - T}{\theta_{\text{ref}}}\right]\Biggr)\Biggr) . \end{aligned} \tag{4.26}$$

Keeping only the term linear in T under the exponential, one can solve for T and calculate dT/df to obtain

$$\frac{R}{r} = \frac{1}{1 - \exp\left(-f/t_a\right)} . \tag{4.27}$$

For $f \ll t_a$, one has $R/r = t_a/f$, which shows a power law decay of the aftershock rate with the normalized time f/t_a. For $f \gg t_a$, one gets $R/r = 1$ and the aftershock rate becomes the background rate.

4.8.3 Scenario 3: Nucleation zones close to failure with $V\theta/L \sim 1$ before the perturbation and $V\theta/L \gg 1$ after the perturbation

In simulations with $a/b \gtrsim 0.5$, the value of $V\theta/L$ becomes close to 1 for a large part of the nucleation zone shortly before the instability (section 4.1.2), consistently with the study of *Rubin and Ampuero* [2005]. This results in elevated aftershock rates in comparison to Dieterich's estimate (e.g., Case 2 in Figure 4.2).

4.8.3.1 Approach I

To approximately estimate the impact of $V\theta/L \sim 1$ on aftershock rates, let us consider a nucleation process in the spring-slider model with $V\theta/L = 1$ before the stress step. The governing equation becomes

$$\tau^o_{\mathrm{ref}} - k\delta \;=\; \bar{\sigma}\left[\mu_0 \;+\; (a-b)\ln\left(\frac{V}{V_0}\right)\right] \;. \tag{4.28}$$

Here we ignore the loading term $\dot{\tau}t$, considering a nucleation process that is so close to failure that it is beyond the influence of slow tectonic loading. Taking into account that $\tau^o_{\mathrm{ref}} - k\delta_{\mathrm{ref}} = \bar{\sigma}\left[\mu_0 + (a-b)\ln\left(V_{\mathrm{ref}}/V_0\right)\right]$ and solving for V, we obtain

$$V(t) \;=\; \frac{d\delta}{dt} \;=\; \frac{V_{\mathrm{ref}}}{V_{\mathrm{ref}}\hat{k}(t - t_{\mathrm{ref}}) + 1} \;, \tag{4.29}$$

where $\hat{k} = k/((a-b)\bar{\sigma})$. As in section (4.8.2), we can rewrite this expression in terms of the original time to instability T (using $t - t_{\mathrm{ref}} = T_{\mathrm{ref}} - T$), get slip velocity after the stress step as $V(T)\exp\left[\Delta\tau/(a\bar{\sigma})\right]$, and find the new time to instability corresponding to this slip velocity using equation (4.11):

$$f(T) \;=\; \frac{a(V_{\mathrm{ref}}\hat{k}(T_{\mathrm{ref}} - T) + 1)}{HV_{\mathrm{ref}}\exp\left(\Delta\tau/(a\bar{\sigma})\right)} \;. \tag{4.30}$$

Solving for T and calculating dT/df, we obtain

$$\frac{R}{r} = \left(\frac{(b-a)b\bar{\sigma}}{aLk} - \frac{(b-a)}{a}\right)\exp\left(\frac{\Delta\tau}{a\bar{\sigma}}\right) \ . \tag{4.31}$$

In equation (4.31), aftershock rates right after the mainshock are different from the model of *Dieterich* [1994] by the factor of $[(b-a)b\bar{\sigma}/(aLk) - (b-a)/a]$. To compare this result with our computed aftershock rates, we need to estimate the effective stiffness k of the simulated nucleation process which changes with time. Since we are considering the final stages of nucleation in this scenario, we set $k = \eta G/h_{\text{nucl}}$, where h_{nucl} is the nucleation size right before instability. Using expression (3.1) for h_{nucl} with $F = (b-a)^2/b$ and $\eta = 2/\pi$ found by *Rubin and Ampuero* [2005] for a/b close to 1, we get

$$\frac{R}{r} = \left(\frac{b^2}{2a(b-a)} - \frac{(b-a)}{a}\right)\exp\left(\frac{\Delta\tau}{a\bar{\sigma}}\right) \ . \tag{4.32}$$

For Case 2 (Figure 4.2), the simulated aftershock rates are larger by a factor of 3.8 relative to the model of *Dieterich* [1994], while the estimate (4.32) predicts a factor of 2.7.

4.8.3.2 Approach II

Instead of using the unperturbed slip-velocity history (4.29), let us assume that the nucleation process follows the behavior given by equation (44) of *Rubin and Ampuero* [2005] for quasi-static nucleation with a/b close to 1:

$$T = \frac{2}{\pi}\frac{bL}{(b-a)V} \ . \tag{4.33}$$

Continuing with the same steps as in Approach I, we obtain:

$$\frac{R}{r} = \left(\frac{2b^2}{\pi a(b-a)} - \frac{4(b-a)}{\pi a} \right) \exp\left(\frac{\Delta\tau}{a\bar{\sigma}} \right) . \tag{4.34}$$

For Case 2 (Figure 4.2), this estimate gives 3.5 for the factor of aftershock rate increase relative to the model of *Dieterich* [1994], which is very close to the actual factor of 3.8.

Chapter 5

Spectral Element Modeling of Spontaneous Earthquake Rupture on Rate and State Faults: Effect of Velocity-Strengthening Fault Friction at Shallow Depths on Dynamic Rupture

In this Chapter, we develop a spectral element method (SEM) for simulating dynamic rupture on rate-and-state faults and use it to study how the rupture is affected by a shallow fault region of steady-state velocity-strengthening friction. In particular, we identify different outcomes in two dynamic rupture scenarios on a fault embedded in homogeneous elastic media: with and without a shallow velocity-strengthening fault patch (section 5.4). We then simulate dynamic rupture scenarios on a fault embedded in a layered bulk structure and study how the peak ground motion at on- and off-fault sites is affected by the bulk structure combined with different fault rheologies (section 5.5).

This Chapter is based on the paper “Spectral element modeling of spontaneous earthquake rupture on rate-and-state faults: Effect of velocity-strengthening friction at shallow depths” by Y. Kaneko, N. Lapusta, and J.-P. Ampuero (*J. Geophys. Res.*, 2008).

5.1 Spectral element method (SEM) for simulations of dynamic ruptures

SEMs have been used to simulate single-earthquake scenarios, mostly with linear slip-weakening (LSW) friction [e.g., *Oglesby et al.*, 1998; *Aagaard et al.*, 2001; *Ampuero*, 2002; *Festa and Vilotte*, 2006; *Madariaga et al.*, 2006]. The application of SEM to wave propagation problems is well developed [*Komatitsch and Vilotte*, 1998; *Komatitsch and Tromp*, 1999] and has been recently reviewed by *Komatitsch et al.* [2005] and *Chaljub et al.* [2007]. SEMs combine the flexibility of FEMs with high numerical accuracy due to the use of higher-order Lagrange interpolants on Gauss-Lobatto-Legendre (GLL) points that mimic the behavior of the Legendre basis [*Komatitsch and Vilotte*, 1998; *Komatitsch and Tromp*, 1999]. Furthermore, the SEMs with a diagonal mass matrix reduce computational costs associated with solving a large linear system and result in relatively simple parallel implementation. The method is well suited for describing surfaces of displacement discontinuity with mixed traction-displacement interface conditions (e.g., faults) by the split-node technique, as in FEMs [*Oglesby et al.*, 1998; *Aagaard et al.*, 2001] and some finite difference methods [*Andrews*, 1999; *Day et al.*, 2005]. Fault surfaces with the split-node technique have been implemented in 2D SEMs [*Ampuero*, 2002; *Vilotte et al.*, 2006], and SEMs with the split-node technique have been successfully applied to wave propagation across compliant faults [*Haney et al.*, 2007] and to earthquake source dynamics [*Festa and Vilotte*, 2005; *Madariaga et al.*, 2006].

The 3D SEM we use was originally developed for wave propagation by *Komatitsch and*

Tromp [1999]; our work is an extension of the study by *Ampuero* [2002] that incorporated a linear slip-weakening (LSW) fault boundary into that SEM framework. We have extended the formulation to RS faults. To validate the developed SEM approach, we have conducted detailed comparison of SEM and BIM simulation results obtained for an antiplane problem (section 5.3). Incorporating RS faults into a SEM formulation requires a semi-implicit numerical scheme which makes the implementation more challenging than that for LSW friction.

5.2 A SEM algorithm for simulations of dynamic rupture on rate and state (RS) faults

5.2.1 Discretized elastodynamic relations

In SEM, the geometry of the mesh elements is represented by the product of low-degree Lagrange polynomials like in the classical FEM, while the field-approximation function is represented by the product of high-degree Lagrange polynomials defined on the Gauss-Lobatto-Legendre (GLL) points. The choice of coincident nodes for interpolation and numerical integration results in a diagonal mass matrix of the discretized domain, reducing the computational costs associated with solving a large linear system and making its parallel implementation relatively simple.

The discretization of the weak form of the equation of motion leads to the matrix equation:

$$\mathbf{M}\ddot{\mathbf{u}} = -\mathbf{K}\mathbf{u} + \mathbf{B}\boldsymbol{\tau} \ , \tag{5.1}$$

where $\mathbf{M}$ and $\mathbf{K}$ are the mass and stiffness matrix respectively, given by *Komatitsch et al.* [2005] (equation (57) and (59)), the fault-boundary matrix $\mathbf{B}$ is described in appendix A, $\boldsymbol{\tau} = \mathbf{T} - \boldsymbol{\tau}_o$ is the relative traction vector on the fault, $\mathbf{T}$ is the total traction, and $\boldsymbol{\tau}_o$ is the traction on the fault that corresponds to the reference zero-displacement state. Vectors $\mathbf{u}$, $\dot{\mathbf{u}}$, and $\ddot{\mathbf{u}}$ collect the values of displacements, particle velocities, and accelerations, respectively, of all the computational nodes of the bulk mesh.

Our time discretization scheme is based upon the explicit acceleration Newmark scheme:

$$\begin{aligned}
\mathbf{u}_{n+1} &= \mathbf{u}_n + \Delta t \dot{\mathbf{u}}_n + \frac{\Delta t^2}{2} \ddot{\mathbf{u}}_n \ , && (5.2) \\
\mathbf{M}\ddot{\mathbf{u}}_{n+1} &= -\mathbf{K}\mathbf{u}_{n+1} + \mathbf{B}\boldsymbol{\tau}_{n+1} \ , && (5.3) \\
\dot{\mathbf{u}}_{n+1} &= \dot{\mathbf{u}}_n + \Delta t \frac{\ddot{\mathbf{u}}_n + \ddot{\mathbf{u}}_{n+1}}{2} \ , && (5.4)
\end{aligned}$$

where the subscripts "n" and "$n + 1$" refer to the number of the time step. Given all the quantities at the nth time step, we would like to obtain the quantities at the $(n + 1)$th time step. The non-trivial advance is to obtain $\boldsymbol{\tau}_{n+1}$ in (5.3) on the fault simultaneously with fault constitutive relations. Combining (5.3) and (5.4), one obtains

$$\dot{\mathbf{u}}_{n+1} = \dot{\mathbf{u}}^{\text{free}}_{n+1} + \frac{\Delta t}{2} \mathbf{M}^{-1} \mathbf{B} \boldsymbol{\tau}_{n+1} \ , \qquad (5.5)$$

where

$$\dot{\mathbf{u}}^{\text{free}}_{n+1} = \dot{\mathbf{u}}_n + \frac{\Delta t}{2} \left(\ddot{\mathbf{u}}_n - \mathbf{M}^{-1} \mathbf{K} \mathbf{u}_{n+1} \right) \qquad (5.6)$$

is the "free velocity" that would prevail if the traction on the fault suddenly vanished,

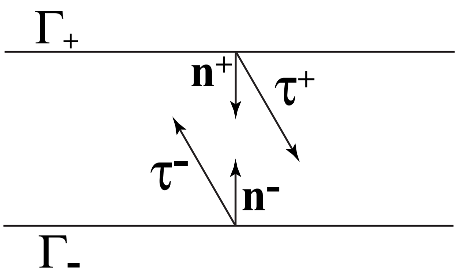

Figure 5.1: The fault divided into two non-overlapping surfaces $\Gamma_\pm$.

creating free-boundary conditions. We now write relation (5.5) for the fault nodes with the ± signs indicating the values of field variables on the two sides of the fault (Figure 5.1):

$$\dot{\mathbf{u}}^{\pm}_{n+1} = \dot{\mathbf{u}}^{\mathrm{free}\pm}_{n+1} + \frac{\Delta t}{2}\mathbf{M}_{\pm}^{-1}\mathbf{B}_{\pm}\boldsymbol{\tau}^{\pm}_{n+1} \ . \tag{5.7}$$

Subtracting the minus side from the plus side, and using the sign convention $\boldsymbol{\tau} = -\boldsymbol{\tau}^+ = \boldsymbol{\tau}^-$, where $\boldsymbol{\tau}^\pm$ are defined with respect to the outward normal from the fault boundary $\Gamma_\pm$ (Figure 5.1), we obtain

$$\dot{\boldsymbol{\delta}}_{n+1} = \dot{\boldsymbol{\delta}}^{\mathrm{free}}_{n+1} - \mathbf{Z}^{-1}\boldsymbol{\tau}_{n+1} \ , \tag{5.8}$$

where vectors $\boldsymbol{\delta}$, $\dot{\boldsymbol{\delta}}$, and $\ddot{\boldsymbol{\delta}}$ refer to the slip, slip velocity, and slip acceleration, defined as the difference between values of displacement, velocity, and acceleration, respectively, of corresponding split nodes across the fault plane (e.g., $\boldsymbol{\delta} = \mathbf{u}^+ - \mathbf{u}^-$ and $\dot{\boldsymbol{\delta}}^{\mathrm{free}} = \dot{\mathbf{u}}^{\mathrm{free}+} - \dot{\mathbf{u}}^{\mathrm{free}-}$), and $\mathbf{Z}$ is the fault impedance matrix given by

$$\mathbf{Z}^{-1} \equiv \frac{\Delta t}{2}\left(\mathbf{M}_{+}^{-1}\mathbf{B}_{+} + \mathbf{M}_{-}^{-1}\mathbf{B}_{-}\right) \ . \tag{5.9}$$

Note that for cases we consider in this study, the fault-normal component of traction $\mathbf{T}$ remains unchanged, and hence the fault-normal components of $\boldsymbol{\tau}$ and $\dot{\boldsymbol{\delta}}$ are zero. The matrices $\mathbf{M}$ and $\mathbf{Z}^{-1}$ are diagonal, and $\mathbf{B}_{+} = \mathbf{B}_{-}$ for conformal meshes. Solving (5.8) for $\boldsymbol{\tau}_{n+1}$ gives

$$\boldsymbol{\tau}_{n+1} = \mathbf{Z}\, \dot{\boldsymbol{\delta}}_{n+1}^{\text{free}} - \mathbf{Z}\, \dot{\boldsymbol{\delta}}_{n+1}\ . \tag{5.10}$$

The expression (5.10) is a local relation which can be solved node by node on the fault. It is convenient to rewrite (5.10) in terms of total traction, $\mathbf{T} = \boldsymbol{\tau} + \boldsymbol{\tau}_o$:

$$\begin{aligned} \mathbf{T}_{n+1} &= \boldsymbol{\tau}_o + \mathbf{Z}\, \dot{\boldsymbol{\delta}}_{n+1}^{\text{free}} - \mathbf{Z}\, \dot{\boldsymbol{\delta}}_{n+1} \\ &\equiv \tilde{\mathbf{T}}_{n+1} - \mathbf{Z}\, \dot{\boldsymbol{\delta}}_{n+1}\ , \end{aligned} \tag{5.11}$$

where $\tilde{\mathbf{T}}$ is the “stick traction” that would prevail if there were a sudden slip arrest.

5.2.2 Rate and state (RS) friction laws

Rate- and state-dependent friction laws were developed to incorporate observations of rock friction experiments at relatively low sliding rates of 10^{-8} to 10^{-3} m/s [*Dieterich*, 1978, 1979; *Ruina*, 1983; *Blanpied et al.*, 1995, 1998; *Marone*, 1998]. In the situations with constant effective normal stress $\bar{\sigma}$, the shear strength $\mathcal{T}$ is often expressed as

$$\begin{aligned} \mathcal{T} &= \psi(\dot{\delta}, \theta) \\ &= \bar{\sigma} \left[f_0 \;+\; a \ln\left(\frac{\dot{\delta}}{\dot{\delta}_0}\right) \;+\; b \ln\left(\frac{\dot{\delta}_0 \theta}{L}\right) \right]\ , \end{aligned} \tag{5.12}$$

where $a > 0$ and b are RS constitutive parameters with magnitudes of the order of 0.01, $\dot{\delta}$ is the magnitude of slip velocity, f_0 is a reference friction coefficient corresponding to a reference slip velocity $\dot{\delta}_0$, θ is a state variable which is typically interpreted as the average age of the population of contacts between two surfaces, and L is the characteristic slip for state evolution [*Dieterich*, 1978, 1979; *Rice and Ruina*, 1983; *Ruina*, 1983; *Dieterich and Kilgore*, 1994]. Two types of state-variable evolution laws are commonly used in modeling:

$$\frac{d\theta}{dt} = 1 - \frac{\dot{\delta}\theta}{L} \quad \text{(aging law)} \ , \tag{5.13}$$

$$\frac{d\theta}{dt} = -\frac{\dot{\delta}\theta}{L} \ln\left(\frac{\dot{\delta}\theta}{L}\right) \quad \text{(slip law)} \ . \tag{5.14}$$

The parameter combination $a - b < 0$ corresponds to steady-state velocity-weakening friction and can lead to unstable slip, whereas $a - b > 0$ corresponds to steady-state velocity-strengthening and leads to stable sliding [*Rice and Ruina*, 1983; *Ruina*, 1983].

In expression (5.12), shear frictional strength $\mathcal{T}$ is undefined for slip velocities $\dot{\delta} = 0$, which is unphysical. To regularize (5.12) near $\dot{\delta} = 0$, we follow the approach of *Rice and Ben-Zion* [1996], *Ben-Zion and Rice* [1997], and *Lapusta et al.* [2000] in using a thermally activated creep model of the direct effect term $a \ln\left(\dot{\delta}/\dot{\delta}_0\right)$ to obtain

$$\begin{aligned}\mathcal{T} &= \psi(\dot{\delta}, \theta) \\ &= a\bar{\sigma} \ \text{arcsinh}\left[\frac{\dot{\delta}}{2\dot{\delta}_0} \exp\left(\frac{f_0 + b\ln(\dot{\delta}_0\theta/L)}{a}\right)\right] \ .\end{aligned} \tag{5.15}$$

This regularization is used in our simulations. It produces a negligible change from (5.12) in the range of slip velocities explored by laboratory experiments; the difference in $\dot{\delta}$ at

$\dot{\delta} \sim \dot{\delta}_0$ is of the order of $\exp(-2f_0/a)$ or less, and the typical value of f_0/a in this study is 40.

5.2.3 Updating scheme: advancing one evolution time step

We have developed an updating scheme, based upon the explicit Newmark method described in section 5.2.1, appropriate for the RS fault boundary condition. Here, we discuss how values of field variables are updated over one evolution time step. Suppose that the discretized values of particle displacement $\mathbf{u}$, particle velocity $\dot{\mathbf{u}}$, and particle acceleration field $\ddot{\mathbf{u}}$ are known at the nth time step. To find the values of the field variables at the $(n+1)$th time step, we perform the following steps.

1. Update the values of displacements, based on the known values at the nth time step:

$$\mathbf{u}_{n+1} = \mathbf{u}_n + \Delta t\ \dot{\mathbf{u}}_n + \frac{1}{2}(\Delta t)^2\ \ddot{\mathbf{u}}_n\ . \tag{5.16}$$

2. Perform the partial update of the particle velocity field in (5.4) by computing

$$\dot{\mathbf{u}}^*_{n+1} = \dot{\mathbf{u}}_n + \frac{1}{2}\Delta t\ \ddot{\mathbf{u}}_n\ . \tag{5.17}$$

3. Compute the “stick” traction in (5.11):

$$\begin{aligned} \dot{\mathbf{u}}^{\text{free}}_{n+1} &= \dot{\mathbf{u}}^*_{n+1} - \frac{\Delta t}{2}(\mathbf{M}^{-1}\mathbf{K}\mathbf{u}_{n+1}) \\ \tilde{\mathbf{T}}_{n+1} &= \boldsymbol{\tau}_o + \mathbf{Z}\ \dot{\boldsymbol{\delta}}^{\text{free}}_{n+1}\ . \end{aligned} \tag{5.18}$$

4. Determine the first prediction of the state variable, θ^*_{n+1}. By integrating the evolution law (5.13) or (5.14) with the constant magnitude $\dot{\delta}_n$ of slip velocity $\dot{\boldsymbol{\delta}}_n = \mathbf{u}^+_n - \mathbf{u}^-_n$ during the time step, we obtain

$$\theta^*_{n+1} = \theta_n \exp\left(-\frac{\dot{\delta}_n \Delta t}{L}\right) + \frac{L}{\dot{\delta}_n}\left(1 - \exp\left(-\frac{\dot{\delta}_n \Delta t}{L}\right)\right) \tag{5.19}$$

for the aging law, and

$$\theta^*_{n+1} = \frac{L}{\dot{\delta}_n}\left(\frac{\dot{\delta}_n \theta_n}{L}\right)^{\exp\left(-\dot{\delta}_n \Delta t / L\right)} \tag{5.20}$$

for the slip law. This approach for updating the state variable is different from the one in *Lapusta et al.* [2000]. We compare the state-variable updating schemes in section 5.3.

5. Find the first prediction of slip velocity, $\dot{\boldsymbol{\delta}}^*_{n+1}$, by equating the magnitude of shear stress in (5.11) and strength in (5.15). The directions of shear traction vector $\mathbf{T}_{n+1}$ and slip velocity vector $\dot{\boldsymbol{\delta}}_{n+1}$ have to coincide. From (5.11), the stick traction $\tilde{\mathbf{T}}_{n+1}$ has the same direction because the fault impedance matrix **Z** is isotropic (appendix 5.7). By projecting (5.11) onto that direction and equating the shear stress magnitude with frictional strength, we obtain the following relation:

$$T^*_{n+1} = \tilde{T}_{n+1} - Z_{\mathrm{x}} \dot{\delta}^*_{n+1} = \psi(\dot{\delta}^*_{n+1}, \theta^*_{n+1}) \ , \tag{5.21}$$

where T and $\tilde{T}$ denote the magnitudes of $\mathbf{T}$ and $\tilde{\mathbf{T}}$, respectively. We find $\dot{\delta}^*_{n+1}$ using the Newton-Raphson search with $\dot{\delta}_n$ as the first guess. Once $\dot{\delta}^*_{n+1}$ are obtained, the traction T^*_{n+1} can be readily found.

6. Calculate the final prediction of state variable, θ^{**}_{n+1}, at the $(n+1)$th time step by replacing $\dot{\delta}_n$ in equation (5.19) or (5.20) with $\left(\dot{\delta}_n + \dot{\delta}^*_{n+1}\right)/2$.

7. Find the final predictions $\dot{\delta}^{**}_{n+1}$ and T^{**}_{n+1} by repeating step 5 with θ^{**}_{n+1} instead of θ^*_{n+1}.

8. Declare the value of T_{n+1} to be equal to the predictions with the superscript double asterisks. Using the directional cosines constructed from the components of $\tilde{\mathbf{T}}_{n+1}$, we obtain the components of $\mathbf{T}_{n+1}$ and relative traction $\boldsymbol{\tau}_{n+1}$.

9. Solve for acceleration of the entire medium:

$$\ddot{\mathbf{u}}_{n+1} = \mathbf{M}^{-1}[-\mathbf{K}\mathbf{u}_{n+1} + \mathbf{B}\;\boldsymbol{\tau}_{n+1}]\;. \tag{5.22}$$

10. Complete the update of $\dot{\mathbf{u}}_{n+1}$ by adding the term containing $\ddot{\mathbf{u}}_{n+1}$:

$$\dot{\mathbf{u}}_{n+1} = \dot{\mathbf{u}}^*_{n+1} + \frac{1}{2}\Delta t\;\ddot{\mathbf{u}}_{n+1}\;. \tag{5.23}$$

This scheme includes two iterations for the update of the state variable. Its accuracy, for a given space grid, is comparable to that of BIM, as discussed in section 5.3. Note that if the second iteration in the state-variable update is omitted, the accuracy significantly decreases in comparison to BIM that also includes two iterations for the update of the state variable.

5.3 Comparison of numerical results obtained with 2D SEM and 2D BIM

5.3.1 2D antiplane problem and comparison criteria

To assess the accuracy of numerical results based on the developed SEM approach, we have conducted detailed comparison of simulation results obtained using SEM and BIM. For simplicity and efficiency, we set up an anti-plane (2D) test problem. The BIM model used for comparison is based on the BIM spectral formulation of *Lapusta et al.* [2000]. Figure 5.2 illustrates the geometry of the anti-plane SEM and BIM models. In SEM, a 15 km by 45 km rectangular domain is used, with four boundaries. The SEM model domain is large enough to avoid any wave reflections from the boundaries during the simulated time. The domain is replicated using periodic boundary conditions on both sides of the domain (Figure 5.2). The fault boundary obeys rate and state (RS) friction with the aging law of state variable evolution. By symmetry consideration, the medium across the fault boundary has equal and opposite motion. In the analogous BIM model, wave propagation is analytically accounted for by boundary-integral expressions. The fault in the BIM model is repeated periodically, as in the SEM model.

The parameters used in the simulations are listed in Table 5.1, and the distribution of initial shear stress on the fault is shown in Figure 5.3A. We make our test problem similar to the SCEC code validation of dynamic rupture [*Harris et al.*, 2009] and the study of *Day et al.* [2005], in terms of bulk properties and cohesive-zone properties, but we use RS friction and consider a 2D scenario. Within the 3-km nucleation region, we use an integer

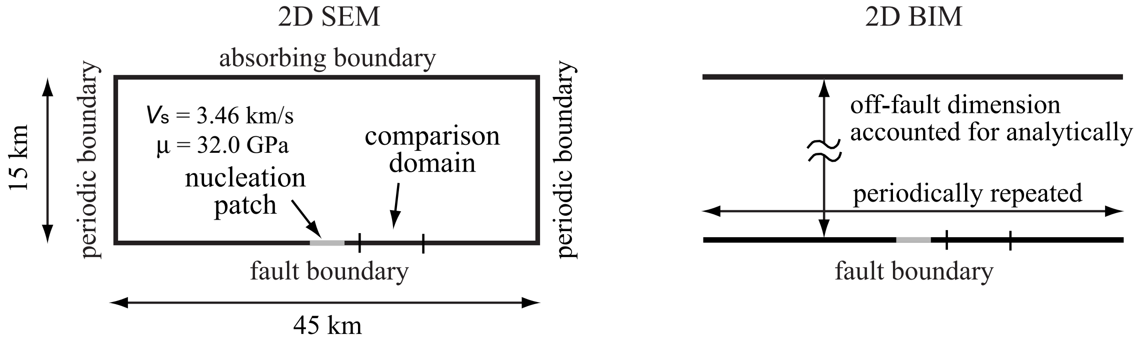

Figure 5.2: A cartoon illustrating the antiplane test problem for 2D SEM (left) and 2D BIM (right). By symmetry consideration, the medium across the fault boundary in both models has equal and opposite motion.

number of spectral elements for SEM and an odd number of computational cells for BIM. We select the polynomial degree to be 4 in SEM throughout the comparison.

Table 5.1: Friction-related parameters used in 2D and 3D simulations. In 2D, the value of θ_{in} within the rupture domain (Figure 5.3) is given. In 3D, the values of $\bar{\sigma}$, a, and b in the region of constant $(a-b)$ in the velocity-weakening area (Figure 5.7) are given.

Parameter	Symbol	Value in 2D	Value in 3D
Reference slip velocity	$\dot{\delta}_0$	10^{-6} m/s	10^{-6} m/s
Reference friction coefficient	f_0	0.60	0.60
Characteristic slip distance	L	0.0370 m	0.0135 m
Effective normal stress	$\bar{\sigma}$	120.0 MPa	80.0 MPa
Initial slip velocity	$\dot{\delta}_{\text{in}}$	10^{-3} m/s	10^{-12} m/s
Initial state variable	θ_{in}	92.7 s	34.38 years
Constitutive parameter a	a	0.0125	0.0080
Constitutive parameter b	b	0.0172	0.0120

At the nucleation patch in the center of the fault, slip velocity increases abruptly due to the difference between the initial shear stress imposed and initial shear strength given by the RS friction. (Note that the initial bulk particle velocity is uniform and equal to half of initial slip velocity on the fault outside the nucleation patch.) The resulting dynamic rupture propagates bilaterally from the nucleation patch. On the RS fault, friction strength is not known in advance as it depends on the current values of slip velocity and state variable. The RS parameters we use (Table 5.1) result in effective slip weakening similar to the LSW friction of the SCEC code validation (Figure 5.3B).

To quantify differences between solutions, we use a quantity analogous to the rupture arrival time. For problems with spontaneous dynamic rupture, the rupture arrival time has been shown to be a sensitive indicator of numerical precision that reflects the nonlinearity of the problem [*Day et al.*, 2005]. In the SCEC code validation [*Harris et al.*, 2009] and the study of *Day et al.* [2005], rupture arrival time was defined as the time when slip velocity first exceeds 1 mm/s. In this study, we use the arrival time of peak slip velocity (PSV), an analogous quantity. This quantity is more convenient for RS faults as it does not require choosing a particular value of slip-velocity threshold and can be used in a wider context, for example, for comparing rupture arrival times in velocity-strengthening regions, which may not achieve slip velocity of 1 mm/s. To compare two solutions, we use root-mean-square (RMS) difference of PSV arrival times, interpolated with the spacing of 0.1 km, over the fault region Ω given by 3.0 km $\leq x \leq$ 9.0 km.

The numerical accuracy critically depends on the ratio $N_c = \Lambda/\Delta x$ or the number of fault node points (with average spacing Δx) within the cohesive (or slip-weakening) zone size Λ [e.g., *Day et al.*, 2005]. We indicate the average cohesive-zone resolution $\bar{N}_c$ over the fault domain Ω in the comparisons that follow. Note that the value of Λ for the quasi-stationary crack [e.g., *Rice*; *Day et al.*, 2005] is 0.62 km for this problem. By comparing simulations with different spatial and temporal resolution, we find, consistently with *Day et al.* [2005], that locations of the highest error correspond to fault regions far from the

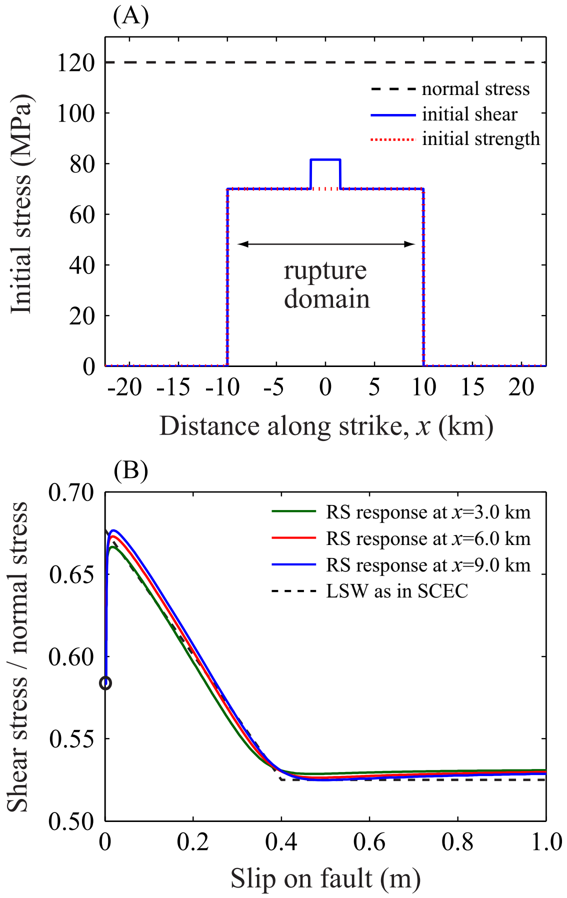

Figure 5.3: (A) Initial stress distribution, similar to that of the SCEC code validation. (B) The effective slip dependence of rate and state (RS) friction. With the parameters listed in Table 5.1, the resulting effective slip dependence of the RS interface (solid lines) over the comparison domain matches very closely the LSW friction in the SCEC validation problem (dashed line). The open circle corresponds to the coefficient of friction associated with the initial strength of the comparison domain.

nucleation patch, because the cohesive-zone size gradually shrinks as rupture accelerates along a homogeneously pre-stressed fault. Hence differences in PSV arrival time at a point close to the end of the ruptured region (e.g., $x = 9$ km) would be a more sensitive indicator of the accumulated error than the RMS difference over the domain. However, RMS values are more indicative of the overall error and help avoid the error scatter through averaging.

5.3.2 Convergence of SEM and BIM solutions with grid reduction

SEM and BIM simulations with high resolution (i.e., large $\bar{N}_c$) result in virtually identical solutions, in the sense that the difference in PSV arrival times and in peak slip velocities is negligible compared to their absolute values. As an example, consider our highest-resolution SEM and BIM simulations, which result in $\bar{N}_c$ of about 22. (The average node spacing of the highest-resolution simulations is 0.0093 km in SEM and 0.0074 km in BIM). At one of the most computationally demanding locations, $x = 9$ km, the difference in the PSV arrival times is $3 \cdot 10^{-4}$ s or 0.01% of the PSV arrival time and the difference in peak velocity is $5 \cdot 10^{-3}$ m/s or 0.05% of the peak velocity. The nearly identical slip velocity histories are shown in Figure 5.4A. Note that the slip velocity history has a pulse-like shape due to the stopping phase arriving from the rupture arrest at $x =$ 10 km.

The convergence of SEM and BIM solutions with grid reduction is shown in Figure 5.4B. The quantity plotted is the root-mean-square (RMS) difference of PSV arrival times relative to the highest-resolution runs; the result is expressed as a percentage of the RMS arrival time of the highest-resolution run. To determine PSV arrival times, we use interpolation of near-peak slip velocity history by piecewise cubic splines with time inter-

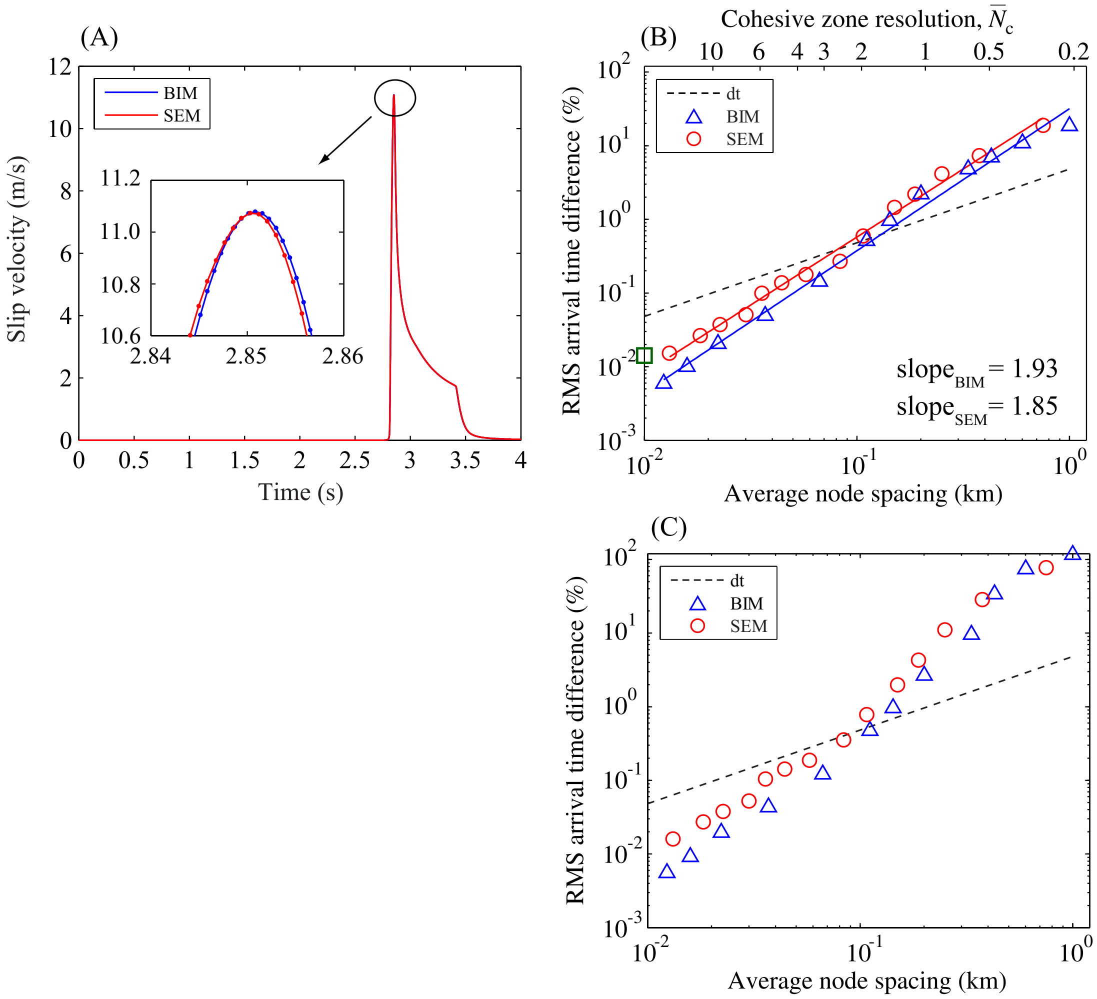

Figure 5.4: (A) Slip-velocity histories at x = 9.0 km, for the highest-resolution simulations of SEM and BIM. The slip-velocity histories are nearly identical as quantified in the text. (B) Differences in arrival time of peak slip velocity (PSV), relative to the highest-resolution runs, shown as a function of average node spacing. Differences are given as RMS averages over the domain 3.0 km $\leq x \leq$ 9.0 km normalized by the RMS arrival time of the highest-resolution runs. Circles are SEM solutions, relative to the highest-resolution run of SEM, and triangles are BIM solutions, relative to the highest-resolution run of BIM. The square on the vertical axis corresponds to the difference between the SEM and BIM highest-resolution runs. The dashed line shows the dependence of time step Δt, set to be equal for both SEM and BIM, on average node spacing, normalized by the RMS arrival time of the highest-resolution runs. The top axis gives the average cohesive-zone resolution $\bar{N}_c$. (C) Errors of BIM and SEM solutions with the alternative state-variable updating scheme (5.24). Comparison with panel B shows that, for discretizations above 10^{-1} km, the errors of both SEM and BIM solutions are higher for this updating scheme.

vals much smaller than the time step of the highest-resolution simulations. Open circles in Figure 5.4B show RMS difference of PSV arrival times as a function of average node spacing for SEM calculations, using the SEM highest-resolution simulation as the reference. Open triangles show the same quantity for BIM, using the BIM highest-resolution simulation as the reference. The differences in PSV arrival times approximately follow a power law in the average node spacing, with the estimated exponents of 1.85 for SEM and 1.93 for BIM. Note that the convergence exponent is similar for SEM and BIM. The estimated cohesive-zone size Λ averaged over the comparison domain is 0.21 km, and the numerical accuracy depends on the cohesive-zone resolution $\bar{N}_c$, consistently with the study by *Day et al.* [2005].

The results show that the highest-resolution solutions, convergence rates, and errors for both SEM and BIM are nearly identical, validating our SEM algorithm.

5.3.3 Evaluation of state-variable updating schemes

The results in section 5.3.2 are obtained using the state-variable updating scheme (5.19). An alternative way of updating the state variable is to use the following relations in the updating scheme (section 5.2.3):

$$\begin{aligned} \theta^*_{n+1} &= \theta_n + \Delta t \dot{\theta}_n \;\; \text{at step } 4 \;, \\ \theta^{**}_{n+1} &= \theta_n + \frac{\Delta t}{2}(\dot{\theta}_n + \dot{\theta}^*_{n+1}) \;\; \text{at step } 6 \;, \end{aligned} \tag{5.24}$$

where $\dot{\theta}_n$ is obtained from the state-variable evolution laws (5.13) or (5.14) with $\dot{\delta} = \dot{\delta}_n$ and $\theta = \theta_n$. This approach was used in *Lapusta et al.* [2000]. Since θ^*_{n+1} in (5.24) is the first-order expansion of (5.19) and (5.20) with respect to Δt for a constant slip velocity, one would expect the state-variable updating scheme (5.24) to be less accurate. We verify this expectation by numerical simulations (Figure 5.4B, C). While the two updating schemes are comparable for fine discretizations ($N_c \gtrsim 2$), the errors for the updating scheme (5.24) are higher in the case of coarser discretizations ($N_c \lesssim 2$), for both SEM and BIM. The error difference for coarser discretizations may be important in 3D simulations, which tend to require marginal discretizations due to their demand on computational resources.

5.3.4 Comparison of simulations with linear slip-weakening (LSW) and rate and state (RS) friction

LSW friction laws are widely used to simulate dynamic rupture. Several dynamic rupture codes for LSW faults have been compared in the SCEC code validation [*Harris et al.*, 2009]. LSW laws incorporate discontinuities in derivatives, such as the abrupt change from weakening to a constant dynamic friction level. RS laws, on the contrary, are smooth. Hence, it is reasonable to hypothesize that RS laws would lead to simulations with better numerical accuracy than LSW laws. Since the aging form of RS laws can match the overall shape of LSW laws quite well, we can use our simulations to test that conjecture. We use the same LSW friction as in the SCEC code comparison, and the parameters of RS friction are chosen to match that LSW friction during dynamic rupture (Figure 5.3).

Figure 5.5A shows that the two laws result in SEM simulations with comparable accuracy. However, there are important differences. For the node spacing larger than ∼0.1 km, the errors of solutions with LSW friction are 33% higher on average than those with

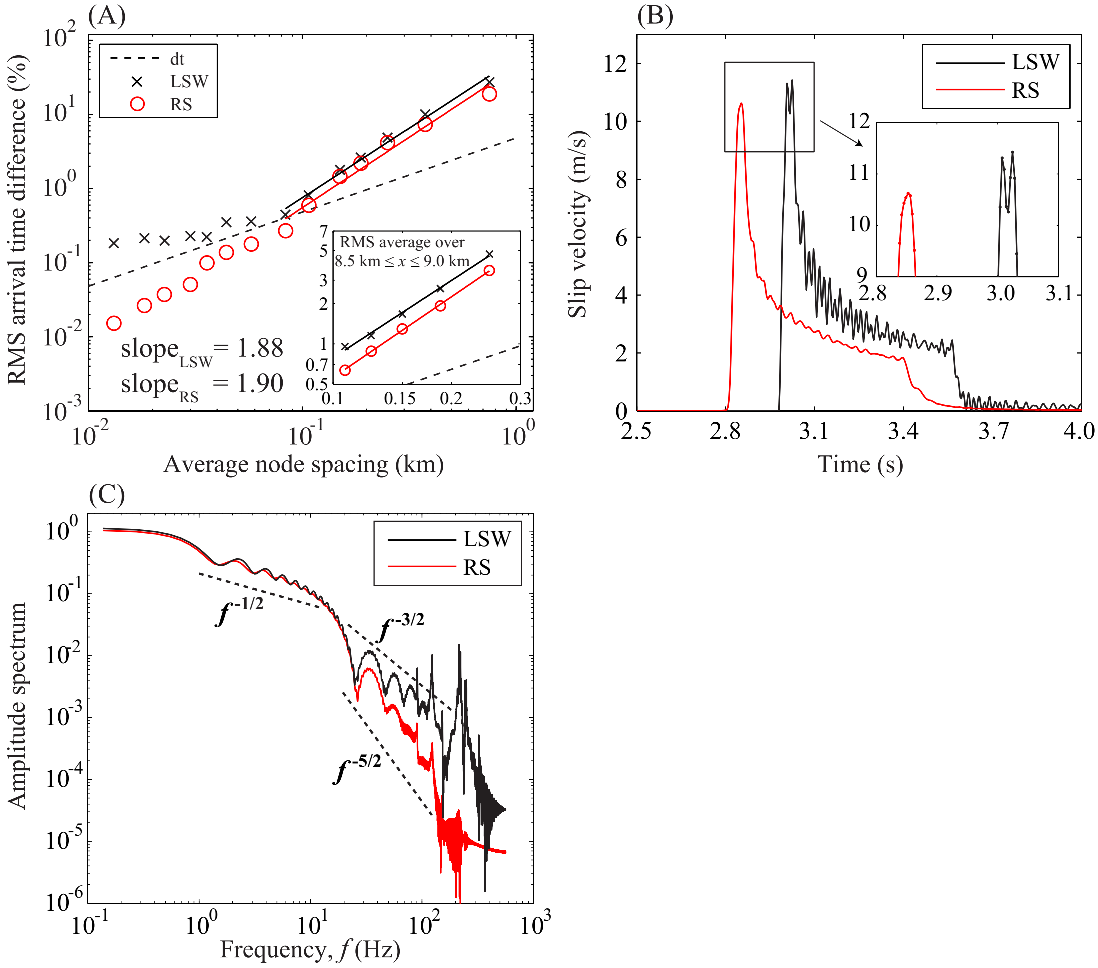

Figure 5.5: (A) Comparison of errors for SEM solutions with LSW and RS friction. The errors for LSW are consistently higher. The inset shows comparison of RMS arrival time difference over the domain 8.5 km $\leq x \leq$ 9.0 km. (B) Slip-velocity histories at $x = 9.0$ km for the simulations with the average node spacing of 0.036 km. The simulation with LSW has much larger numerical oscillations. Note that the visible time difference between rupture arrivals for the two cases arises because the two simulations are not identical in terms of the friction law, although they are very similar in terms of slip-weakening behavior. The faster rupture arrival in the simulation with RS friction indicates a larger average rupture speed and hence a more challenging calculation. (C) Amplitude spectra of slip velocity at $x = 9.0$ km for the highest-resolution SEM simulations with LSW and RS friction. The faster decay of the high-frequency ($f \gtrsim 20$ Hz) part of the spectra explains the superior convergence behavior and numerical stability of simulations with RS friction as discussed in the text.

the aging law of RS friction. Hence, as expected, RS friction results in smaller errors for the same node spacing. Even though the computational time for the same node spacing is larger for RS friction than LSW friction, one can obtain the same accuracy using a coarser node spacing in the calculations with RS friction, actually reducing the computational time in comparison with LSW. To illustrate this point, we consider RMS difference in PSV arrival time over the domain 8.5 km $\leq x \leq$ 9.0 km, where the errors would be expected to be higher than for smaller x (Figure 5.5A inset). LSW simulation with $\Delta x = 0.107$ km and RS simulation with $\Delta x = 0.125$ km have comparable error of about 1%. For the node spacing of 0.107 km, the CPU time is 1.35 times longer in the calculation with RS friction than in that with LSW friction. However, the CPU time and memory in the RS calculation with the node spacing of 0.107 km is 1.53 and 1.36 times larger, respectively, than the one with 0.125 km. Hence, RS calculation with $\Delta x = 0.125$ km takes 12% less CPU time and 36% less memory than the LSW calculation with $\Delta x = 0.107$ km that has comparable accurary. This illustrates that the computational cost with respect to a given accuracy of a solution is smaller in calculations with RS friction than in those with LSW friction. Note that the differences in CPU time and memory become even larger for 3D computations, as the differences increase with the number of the node points.

In addition, numerical oscillations, caused by discontinuities of derivatives in LSW friction, increase numerical noise and prevent further reduction of errors for finer discretizations. Such numerical oscillations are appreciably smaller in simulations with RS friction than in those with LSW friction, as Figure 5.5B shows for the node spacing of 0.036 km. The oscillatory slip velocity near the peak in the LSW simulation results in much higher errors for finer discretizations (Figure 5.5B). Note that numerical damping in the form of Kelvin-Voigt viscosity is often used to suppress numerical noise for the calculations with LSW friction [e.g., *Day et al.,* 2005]. Our experience with using damping indicates that it also results in slower rupture speed (longer PSV arrival time), which decreases the convergence rate.

We quantify the degree of smoothness of the solutions obtained using the two friction laws by comparing the spectra of slip velocity (Figure 5.5C). The spectra differ for high frequencies ($f > 20$ Hz). While that frequency range cannot be resolved by inversions of seismological data and it is beyond the frequency band relevant for most engineering applications, it reveals important differences in the behavior of the two solutions. The decay of high frequencies (20 Hz $\lesssim f \lesssim 100$ Hz) for the simulation with RS friction is approximately proportional to $f^{-5/2}$, which is faster than the $f^{-3/2}$ decay for the simulation with LSW friction. Hence slip velocity at the onset of sliding for RS and LSW friction are proportional to $t^{3/2}$ and $t^{1/2}$, respectively, and the corresponding slip acceleration is proportional to $t^{1/2}$ and $t^{-1/2}$. This behavior of the numerical solutions for LSW indicates that, in the corresponding continuum solutions, slip acceleration at the onset of sliding is infinite, consistently with the finding of *Ida* [1973], and abruptly jumps from zero, whereas slip acceleration for RS friction is finite and smoothly changes from zero. The discontinuity in the continuum solution with LSW friction limits the quality of the corresponding numerical solutions. That is why the model with RS friction results in numerical solutions with smaller oscillations and has better convergence than that with LSW friction (Figure 5.5A,B).

We conclude that, for a given accuracy of solutions, the aging form of RS law leads to more stable and accurate simulations than LSW law, while producing savings in computational time and memory.

5.3.5 Simulations with the slip law of state-variable evolution

In addition to the aging law considered so far, other formulations of the state-variable evolution have been proposed, including the slip law, the composite law, and laws with more than one state variable [*Ruina*, 1983; *Rice and Ruina*, 1983; *Gu et al.*, 1984; *Kato and Tullis*, 2001]. Several recent nucleation studies [*Kato and Tullis*, 2001; *Rubin and Ampuero*, 2005; *Ampuero and Rubin*, 2008] found notable differences between models with different state-variable evolution laws. Which formulations most adequately represent laboratory experiments is a question of active current research [e.g., *Bayart et al.*, 2006].

Figure 5.6A shows that the errors of SEM solutions with the slip law are much higher than those with the aging law, for the same parameters. In comparison with the aging law, the slip law requires much higher numerical resolution to establish the same order of accuracy. This is because the effective slip-weakening rate (i.e., the rate of stress decrease with slip) is variable for the slip law, with the maximum effective slip-weakening rate larger in simulations with the slip law than with the aging law for the same RS parameters (Figure 5.6B) by a logarithmic factor of peak slip velocity [*Ampuero and Rubin*, 2008]. In our test problem, when the value of the characteristic slip L in the slip law is increased eight times, the maximum effective slip-weakening rate becomes approximately equal for both laws in this particular model, and the errors in simulations with the slip law (Figure 5.6A) become comparable to the errors in the simulations with the aging law (Figure 5.4B). These

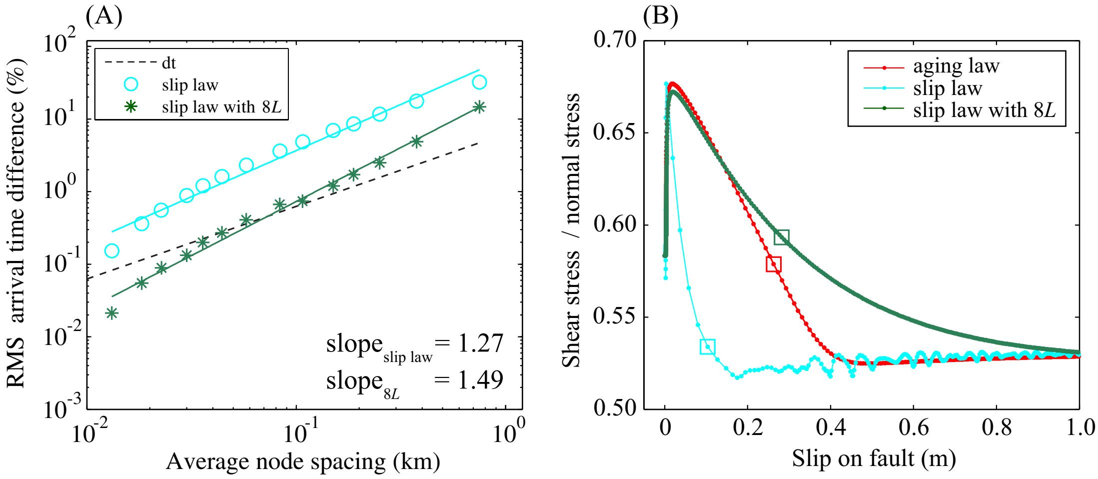

Figure 5.6: (A) Errors for SEM solutions with the slip law of state-variable evolution. Blue circles correspond to the errors for SEM calculations with the parameters of Table 5.1. Green stars correspond to the errors for SEM calculations with eight times larger characteristic slip L. The overall errors for the slip law with eight times larger L is comparable to that of the aging law shown in panel B of Figure 5.4. (B) Effective slip dependence of the friction coefficient at $x = 9.0$ km for the highest-resolution simulations with the aging law, the slip law, and the slip law with eight times larger L. The squares show the values of stress and slip at the PSV arrival time at $x = 9.0$ km.

results suggest that errors are controlled by the resolution of the maximum effective slip-weakening rate. Note that this is consistent with the notion that the resolution of cohesive zone controls errors for calculations with LSW friction and the aging law of RS friction. In LSW friction, effective slip-weakening rate at the rupture front is constant, and the cohesive-zone size reflects that rate. The aging law results in slip-dependent behavior close to that of LSW friction (Figure 5.6B).

5.4 Effect of velocity-strengthening fault friction at shallow depths on dynamic rupture

We use the SEM for rate-and-state faults developed in section 5.2 and validated in section 5.3 to investigate the effect of different fault rheologies on dynamic rupture in a 3D fault model. The fault is governed by the aging form of RS friction, with relatively uniform pre-stress. We consider two dynamic rupture scenarios on a vertical strike-slip fault embedded into an elastic half-space: Case 1 with velocity-weakening friction extending up to the free surface, and Case 2 with a shallow 3-km velocity-strengthening region next to the free surface (Figure 5.7). Case 2 is motivated by the inferred existence of a velocity-strengthening fault rheology at shallow depths as described in section 1. Absorbing conditions [*Clayton and Engquist*, 1977] are used on all boundaries of the SEM model except the free surface and the fault boundary, to simulate a semi-infinite elastic half-space.

Figures 5.7 and 5.8 illustrate parameters and initial conditions for the SEM model. The effective normal stress, $\bar{\sigma} = \min[1.0 + 16.2z, 80.0]$ MPa, where z is in kilometers, increases with depth due to the difference of overburden minus hydrostatic pore pressure and becomes constant (80.0 MPa) at depths larger than 4.9 km, due to the assumption that fluid over-pressure prevents further increase of $\bar{\sigma}$ with depth [*Rice*, 1993; *Ben-Zion and Rice*, 1997]. We compute the initial stress distribution in Figure 5.8A based on (5.12) by assuming that initial slip velocity $\dot{\delta}_{\text{in}} = 10^{-12}$ m/s and initial state variable $\theta_{\text{in}} = 34.38$ years are constant throughout the fault (Table 5.1). The initial stress distribution at shallow depths are slightly different in Cases 1 and 2 due to the difference in the friction parameters

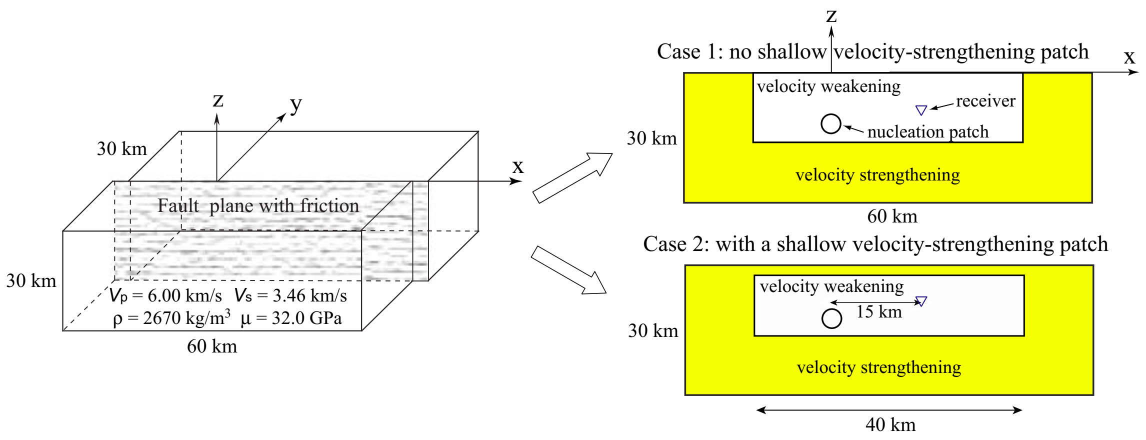

Figure 5.7: A 3D model of a vertical strike-slip fault embedded into an elastic half space. Two cases with different fault rheologies are considered, with and without shallow velocity-strengthening patch. At the horizontal transitions from velocity-weakening to velocity-strengthening properties ($x = -10$ km and $x = 30$ km), the value of a stays constant and the value of $(a - b)$ abruptly changes from -0.004 (velocity weakening) to 0.004 (velocity strengthening). The depth dependence of a and $(a - b)$ within the region -10 km $< x <$ 30 km is shown in Figure 5.8.

a and b.

The medium is initially moving on the two sides of the fault with equal and opposite horizontal particle velocities of $\dot{\delta}_{\text{in}}/2 = 5 \cdot 10^{-13}$ m/s, values much smaller than typical plate loading rates of 10^{-10} to 10^{-9} m/s. Starting at time $t = 0$, dynamic rupture is initiated by imposing a rapid but smooth time-dependent variation of the horizontal shear traction in a circular patch (*E. Dunham, personal communication*, 2008; *Rojas et al.* [2007]; appendix 5.8). This initiation procedure results in fast but gradual variations in slip velocity, producing more stable numerical results for lower numerical resolutions in comparison to the more abrupt initiation procedure (in the form of an overstressed patch of higher initial stress) of section 2. The difference between the two procedures is especially important in 3D problems, which are expensive computationally.

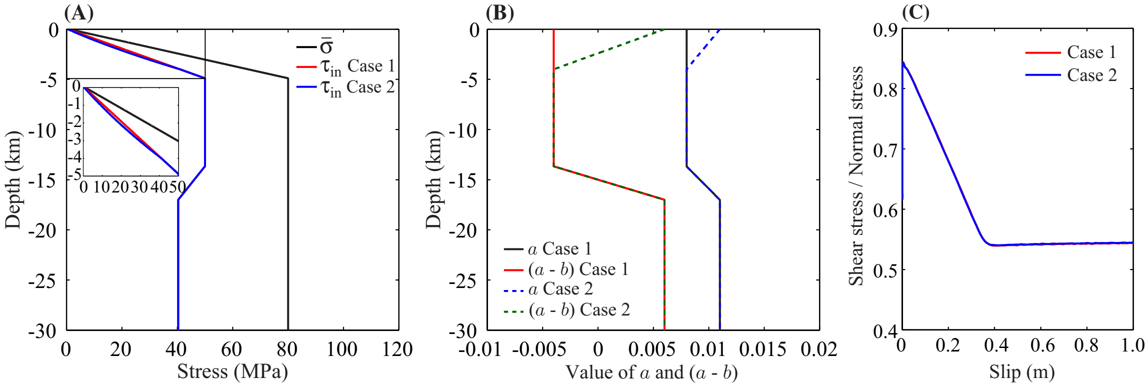

Figure 5.8: (A) Depth-variable distribution of effective normal stress and initial horizontal shear traction in Cases 1 and 2. The initial shear traction for $z \leq 5.0$ km is slightly different in each Case due to the difference in friction parameters a and b. The initial shear strength is equal to the initial horizontal shear traction. (B) Depth-variable distribution of the parameters $(a - b)$ and a within the region -10 km $< x <$ 30 km. (C) The resulting effective slip dependence of friction at the fault location (x, z) = (15 km, -7.5 km).

Dynamic ruptures in the two cases are compared in Figures 5.9-5.12. Each simulation has an average node spacing of 0.050 km and takes 5 hours with 150 processors on Caltech supercomputer, CITerra. Figure 5.9 gives snapshots of the strike-parallel component of slip velocity every 2 seconds for Case 1 (top) and Case 2 (bottom). The rupture initiates at the nucleation patch and then spontaneously propagates until it encounters velocity-strengthening regions at the 15-km depth and at lateral distances of $-10, 30$ km, where slip gradually terminates. The resulting slip dependence of the RS simulation at the fault location $(x, z) = (15 \text{ km}, -7.5 \text{ km})$ is shown in Figure 5.8C.

5.4.1 Suppression of supershear rupture near the free surface

Significant differences between the two cases start to arise when the rupture reaches the velocity-strengthening patch next to the free surface. In the absence of the shallow velocity-

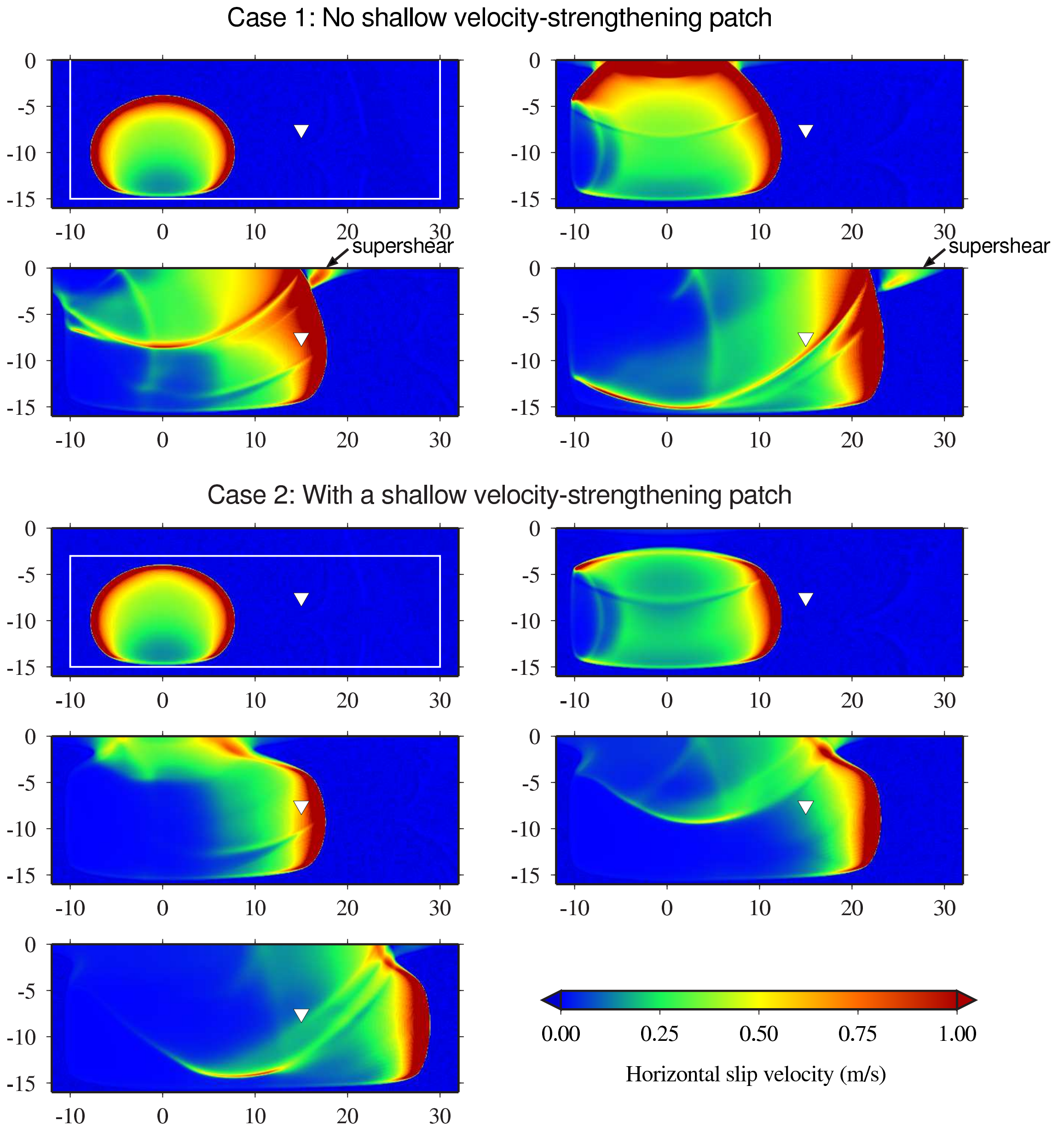

Figure 5.9: Snapshots of horizontal slip velocity (m/s) on the fault every 2 seconds for Case 1 (top) and Case 2 (bottom). White lines on two snapshots represent the boundary between velocity-weakening and velocity-strengthening regions. Slip velocity and slip at the location of an inverted triangle are plotted in Figure 5.12. Note that only a part of the fault close to the velocity-weakening region is shown.

strengthening patch (Case 1), the rupture front next to the free surface propagates with a supershear speed (Figure 5.9). This supershear rupture propagation near the free surface has been observed in simulations with LSW faults [*Aagaard et al.*, 2001; *Day et al.*, 2008].

In the presence of the shallow velocity-strengthening patch (Case 2), the supershear rupture propagation near the free surface is suppressed (Figure 5.9). This is consistent with the fact that supershear rupture propagation near the free surface has not been commonly reported in large crustal earthquakes. Our results indicate that velocity-strengthening friction at shallow depths may account for, or at least contribute to, the lack of universal supershear rupture near the free surface. Other factors might contribute to suppression of supershear propagation at the free surface, such as a potential increase in breakdown work close to the free surface due to more distributed shear at low normal stresses or lower initial shear stress than assumed in this work.

Figure 5.10 shows particle-velocity seismograms on the free surface, 2.0 km away from the fault trace. We see that the arrival phase in the waveforms (a solid black line) has a speed higher than the shear wave speed (V_s). The differences in waveforms for the two cases are significant due to the combination of two effects in Case 1: high slip velocity on the fault near the free surface and the supershear phase. The differences indicate that it might be possible to infer the existence of shallow velocity-strengthening patches from seismic observations.

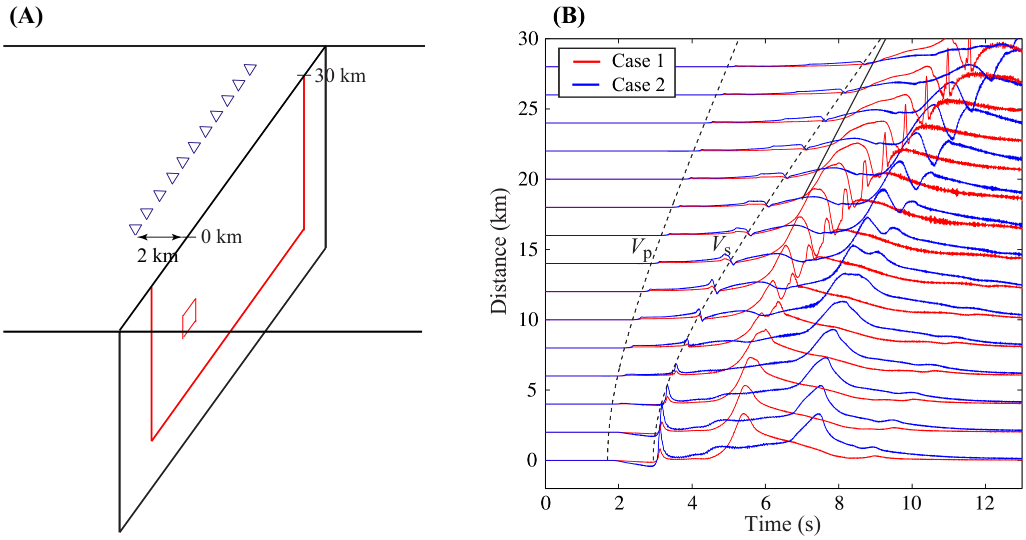

Figure 5.10: (A) Off-fault receiver locations for the 3D SEM model. (B) Strike-parallel particle velocity at those receivers. The amplitudes at the individual receivers are normalized by the maximum amplitude at that receiver for Case 1 (red curve). The dashed lines correspond to apparent V_p and V_s arrivals. The black solid line shows approximate arrival of the phase that corresponds to the supershear rupture.

5.4.2 Smaller final slip throughout the fault

The shallow velocity-strengthening patch in Case 2 causes an appreciable slip reduction over the entire fault (Figure 5.11). The existence of the shallow velocity-strengthening patch suppresses the slip due to the combination of two effects. The first one is that the healing phase created at the shallow rheological transition gradually ceases the slip at depth. The second effect is that the rupture reflected from the free surface in Case 1 induces further slip at depths, whereas in Case 2, the effect of the reflected rupture decreases due to the suppressed slip in the velocity-strengthening patch at shallow depths. Thus, the total amount of slip at depth is smaller in Case 2 than in Case 1 (i.e., 25% smaller at the receiver in Figure 5.11). The difference in final slip between Case 1 and Case 2 is largest next to the free surface. The resulting profile of slip with depth (Figure 5.11) indicates shallow

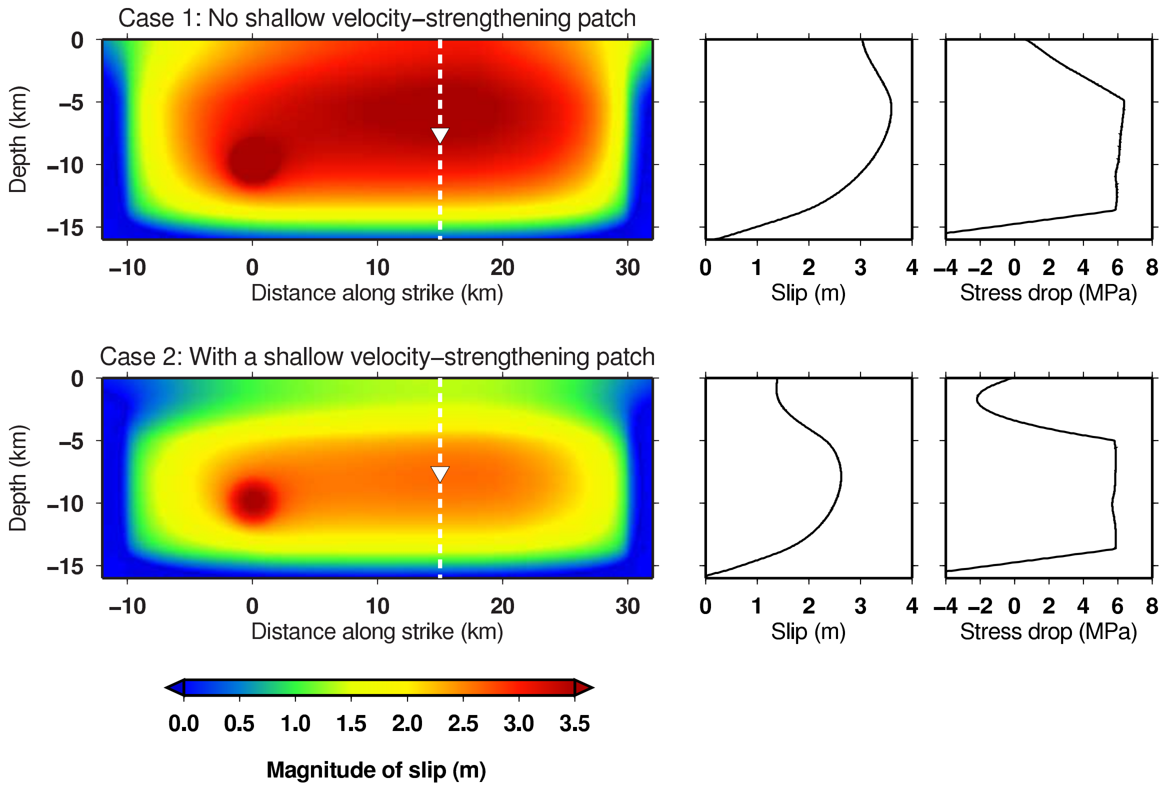

Figure 5.11: Final slip over the fault and depth profiles of slip and stress drop along the dashed lines for Case 1 (top row) and Case 2 (bottom row). Slip in Case 2 is reduced throughout the fault. The shallow velocity-strengthening patch results in negative stress drop (or stress increase).

coseismic slip deficit, which is qualitatively consistent with observations [*Fialko et al.*, 2005]. Note that these two rupture scenarios yield comparable moment magnitudes; M_w = 7.1 in Case 1 and 7.0 in Case 2.

The slip reduction corresponds to smaller stress drop. The values of depth-averaged (from 0 km to 15 km) static stress drop for Case 1 and 2 (Figure 5.11) are 4.9 MPa and 3.5 MPa, respectively. Note that stress drop within the shallow velocity-strengthening patch is negative, that is, shear stress increases after the earthquake. Another mechanism that can contribute to negative stress drop at shallow depths is low initial stress in low-rigidity shallow materials resulting from uniform tectonic strain [*Rybicki and Yamashita*, 1998].

5.4.3 Faster decrease of slip velocity behind the rupture front: implications for the rise time

One of the important source parameters inferred by seismic inversions is the rise time T_s (i.e., slip duration at a point on the fault). Let us consider the rise time for Cases 1 and 2. Figure 5.12A shows the evolution of slip velocity at the middle of the seismogenic depth (7.5 km depth) at the distance of 15 km from the center of the nucleation patch (the inverted triangle in Figure 5.9). This representative profile has a strong rupture front followed by gradually decreasing weak "tail," for both Cases 1 and 2. Such slip velocity profile is commonly referred to as "crack-like," as there is no self-healing behind the rupture front. However, slip velocity in the "tail" is rather small and slowly varying compared to the rupture front. The rise time that seismic inversions would determine for such rupture should depend on the inversion method, the amount and quality of available seismic data, and other factors, and determining that "seismic" estimate of the rise time is beyond the scope of this study. To obtain some simple estimates, we consider here slip durations with slip velocities larger than a given cutoff value (Figure 5.12B). Note that the resulting slip durations are generally lower for Case 2 which contains the shallow velocity-strengthening region.

We compare these slip durations with the study by *Heaton* [1990], which demonstrated that the rise time T_s in seismic inversions is significantly shorter than the time T_s^H required for rupture to receive the healing phase due to the effective seismogenic width of faults:

$$T_\mathrm{s} \ll T_\mathrm{s}^\mathrm{H} \equiv \frac{2\sqrt{S}}{3V_\mathrm{r}} \;, \tag{5.25}$$

where $T_{\mathrm{s}}^{\mathrm{H}}$ is the rise time estimate from *Day* [1982] used in *Heaton* [1990] for the fault aspect ratio < 2, V_{r} is the velocity of the rupture front, and S is the ruptured area. Using the average rupture velocity around the receiver location in Figure 5.9 (2.75 km/s) and the ruptured area up to the location (25 km by 15 km), we obtain $T_{\mathrm{s}}^{\mathrm{H}} = 4.7$ s. This value is comparable to the slip duration in our simulations for the cutoff velocity of 0.1 m/s. For larger cutoff velocities, the estimated slip durations are shorter, especially for the case with the shallow velocity-weakening region, being closer to the range of rise times given by seismic inversion data in *Heaton* [1990]. This is consistent with studies [e.g., *Beroza and Mikumo*, 1996] that noted that fault heterogeneity can produce local arrest phases and reduce the rise time. The shallow velocity-strengthening region acts as such a heterogeneity, effectively reducing the width of the seismogenic zone, as well as diminishing the effect of the free surface. Note that a number of dynamic weakening mechanisms promote self-healing of ruptures and hence short rise times [e.g., *Lu et al.*, 2007, and references therein]; the work of *Heaton* [1990] advocated strongly rate-dependent friction that can result from shear heating [e.g., *Rice*, 2006]. Our methodology can incorporate dynamic weakening mechanisms by combining them with RS friction, and our implementation of enhanced co-seismic velocity weakening in a 3D SEM code has been successfully validated as a part of the SCEC code comparison exercise.

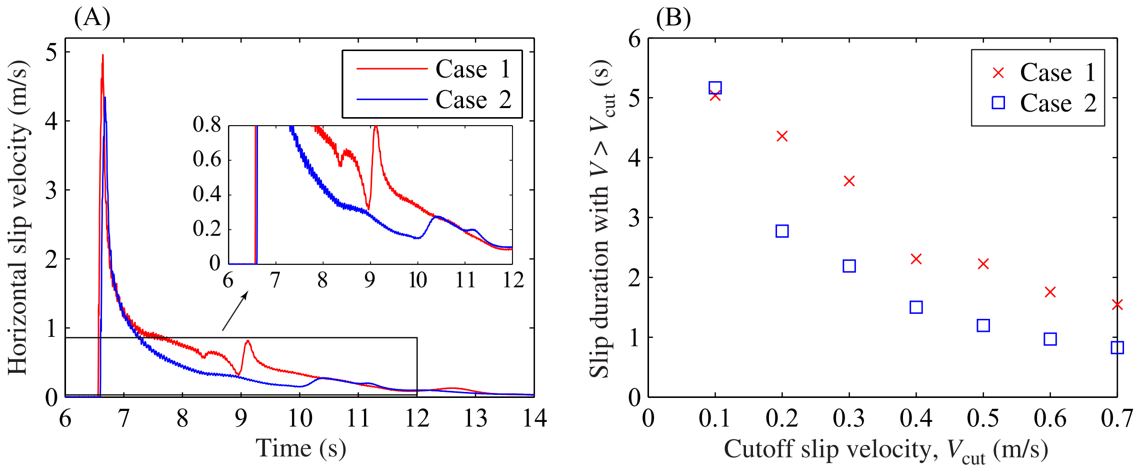

Figure 5.12: (A) Horizontal slip velocity at a location indicated by an inverted triangle in Figure 5.9 for Case 1 and Case 2. (B) Slip durations for Case 1 and 2 at the same receiver for different slip-velocity cutoffs. The slip durations are smaller for the case with the shallow velocity-strengthening region (Case 2).

5.5 Effect of velocity-strengthening friction at shallow depths on ground-motion amplification due to a layered bulk structure

In this section, we investigate how low-velocity bulk layers at shallow depths, in combination with different fault rheologies, affect the ground motion. Figure 5.13A illustrates elastic parameters used for the layered bulk structure; two low-velocity layers above 5-km depth are added to the homogeneous case used in section 5.4. This layered bulk model approximately corresponds to the 1D Parkfield velocity structure used in the study by *Custódio et al.* [2005]. Uniform bulk attenuation is accommodated by the approach of *Komatitsch and Tromp* [1999], with the shear quality factor $Q_\mu = 40$ and infinite bulk quality factor.

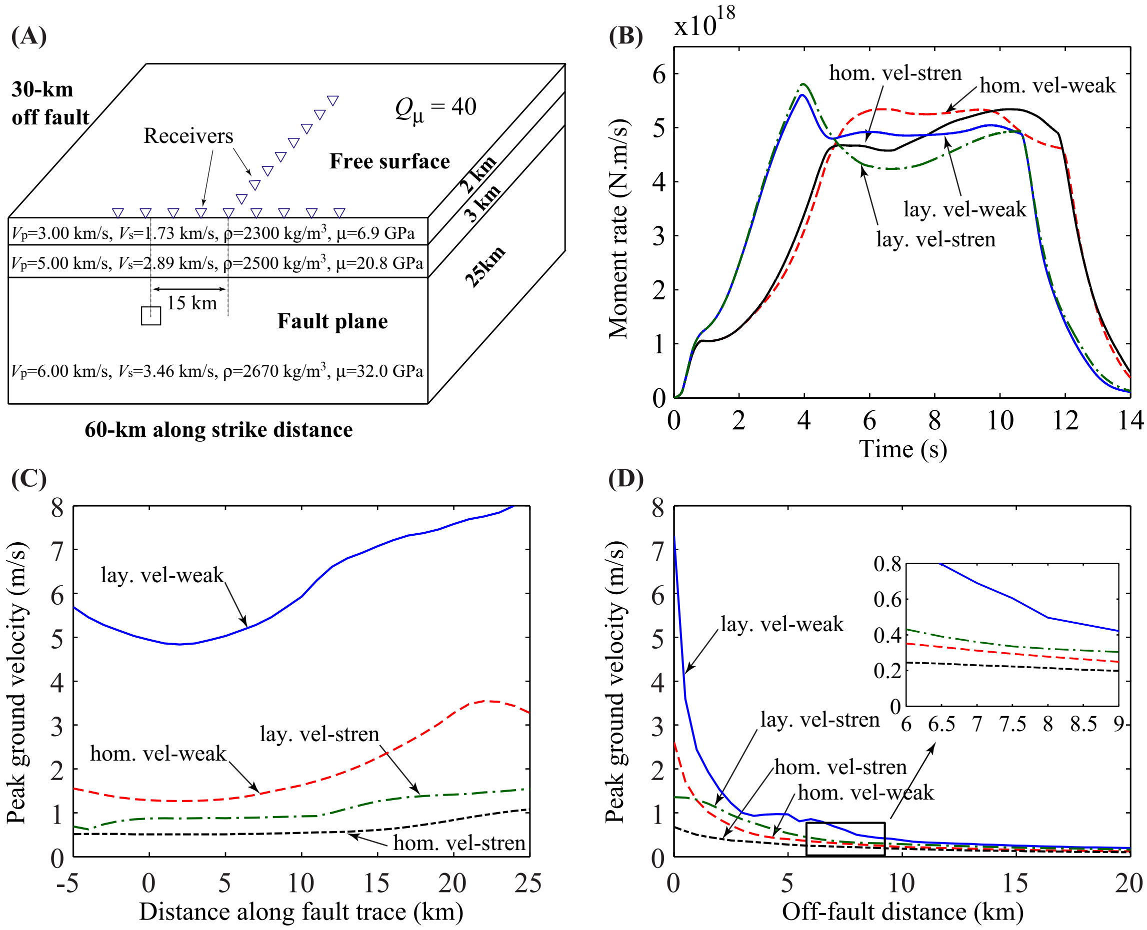

Figure 5.13: (A) A 3D model with a layered bulk structure. (B) Computed moment rate for four different earthquake scenarios with: (1) homogeneous bulk structure without the shallow velocity-strengthening patch; (2) homogeneous bulk structure with the shallow velocity-strengthening patch; (3) layered bulk structure without the shallow velocity-strengthening patch; (4) layered bulk structure with the shallow velocity-strengthening patch. (C) Peak ground velocity (PGV), $\dot{u}_{\text{peak}} = \max(\sqrt{\dot{u}_{\text{x}}^2 + \dot{u}_{\text{y}}^2 + \dot{u}_{\text{z}}^2})$, at on-fault receivers ($z = 0$) shown in panel A. PGV is much smaller in the cases with the shallow velocity-strengthening patch for both layered and non-layered bulk. (D) PGV at off-fault receivers shown in panel A. The difference in PGV for the different fault rheologies remains significant over off-fault distances comparable to the seismogenic width (∼15 km).

We consider four earthquake scenarios. They are combinations of two different fault rheologies (velocity weakening up to the free surface vs. a shallow 3-km velocity-strengthening patch) and two different bulk structures (homogeneous vs. layered). We make the seismic moment rate and total moment approximately equal in the four cases to create similar source processes. As shown in section 5.4, for a given initial stress, the case with the shallow velocity-strengthening patch results in smaller slip, and hence a smaller value of seismic moment, than the case with no shallow velocity-strengthening patch. To obtain similar values of seismic moment for the four scenarios considered here, we use, for the cases with the shallow velocity-strengthening patch, 3% larger initial shear stress than the one used in section 5.4. Figure 5.13B shows the computed moment rate for the four earthquake scenarios. We see that the four scenarios result in similar values of seismic moment rate; the total moment differs by less than 4%. Note that the seismic moment is relatively insensitive to the change in a bulk structure because the slip gets amplified at places where the shear modulus is relatively low.

The change in bulk properties as well as the slip redistribution due to fault rheology substantially influence the peak ground velocity (PGV). PGV at the on- and off-fault receivers is amplified in the layered bulk cases due to the reduction in elastic moduli (Figure 5.13C,D). An interesting feature is the smaller values of PGV, for a given bulk structure, for the cases with the shallow velocity-strengthening patch, even as far as 10 km away from the fault. For example, the PGV at the 7.5-km off-fault receiver is 45% smaller for the case with the shallow velocity-strengthening patch (blue line) than for the case with no shallow velocity-strengthening patch (green line). The difference is large near the fault trace and decreases with the distance away from the fault. This result suggests that both bulk structure as well as fault rheology are important parameters for the peak ground motion.

Another interesting feature is the presence of high-frequency surface waves whose energy is trapped within the shallow low-velocity bulk layers (Figure 5.14). In the case of the layered bulk structure without the shallow velocity-strengthening fault rheology, high-frequency Rayleigh waves (Figure 5.14A) form as a result of the large fault-perpendicular particle velocities on the fault near the free surface (Figure 5.14B), which are, in turn, related to the large slip velocities (e.g., fault-parallel velocities) near the free surface. In the absence of attenuation or for weaker attenuation ($Q_s \gtrsim 40$), the amplitude of the Rayleigh waves becomes larger than the amplitude of body waves at the distance of several kilometers from the fault trace and remains high over a wide range of the off-fault distances. However, such high-frequency Rayleigh waves have not yet been observed in strong-motion records (*Heaton*, personal communication, 2007). One explanation for the absence of the high-frequency Rayleigh waves is their scatter by more complex bulk structure than the idealized layered bulk assumed in our simulations (*Heaton*, personal communication, 2007). We show that a shallow velocity-strengthening fault region can provide an alternative explanation, since high-frequency Rayleigh waves do not form in the case with velocity-strengthening fault friction at shallow depths (Figure 5.14), which suppresses slip velocity near the free surface.

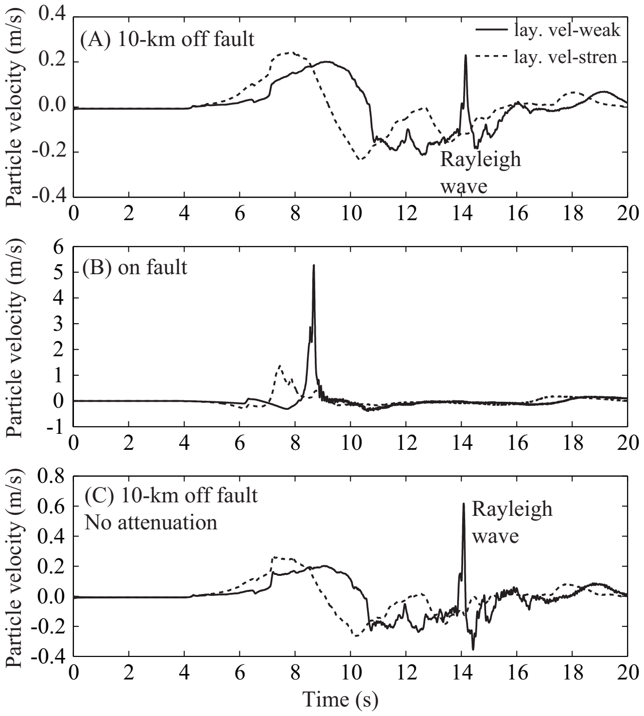

Figure 5.14: (A) Fault-perpendicular particle velocity at the off-fault receiver located 10 km away from the fault, at the distance of 15 km from the nucleation point along the strike. (B) Fault-perpendicular particle velocity at the on-fault receiver with the same along-strike distance. (C) Fault-perpendicular particle velocity at the off-fault receiver in panel A in the case without attenuation. These seismograms correspond to the cases with the layered bulk structure. When there is no velocity-strengthening region close to the free surface (solid lines in panels A, C), a high-frequency Rayleigh peak is observed. In the non-attenuating medium (panel C), the amplitude of the high-frequency Rayleigh wave becomes significantly higher than the body wave amplitude. Note that the scale is different in panels A and C. The Rayleigh wave peak is not observed for the cases with the shallow velocity-strengthening patch both with and without attenuation (dashed lines in panels A, C).

5.6 Conclusions

We have developed an algorithm for simulating dynamic rupture on rate and state (RS) faults in the context of 2D and 3D SEM models. Our SEM test results have accuracy comparable to that of BIM over a wide range of node spacings. We have also demonstrated that the computational cost with respect to a given accuracy of a solution is smaller in calculations with the aging form of RS friction than with linear slip-weakening friction. Simulations with the slip form of RS friction require much higher numerical resolution than those with the aging form due to the higher maximum effective slip-weakening rate at the rupture front for the slip law than for the aging law, for the same rate and state parameters. As a result, we have found that solution errors in dynamic rupture problems are controlled by the resolution of the maximum effective slip-weakening rate at the propagating rupture front.

Using the developed SEM approach, we have shown that the presence of velocity-strengthening fault friction at shallow depths significantly affects dynamic rupture. A shallow velocity-strengthening region suppresses supershear propagation near the free surface, which could explain the lack of universal observations of such near-surface supershear rupture. In addition, it decreases slip accumulation over the entire fault. The largest slip decrease occurs close to the free surface, consistently with the observed deficit of shallow coseismic slip in large earthquakes. Note that velocity-strengthening properties of the shallow layer can be adjusted to reduce the slip accumulation there further, or even completely prevent the rupture from propagating to the free surface. A shallow velocity-strengthening region results in faster decrease of slip at the tail of propagating rupture at seismogenic depths than in the case without such region, creating shorter effective rise times. The amplification of ground motion due to low-velocity elastic structure is decreased in the presence of a velocity-strengthening region at shallow depths, due to the redistribution of slip. These results suggest the importance of the shallow velocity-strengthening fault region not only for quasi-static response such as aseismic transients and afterslip, but also for dynamic rupture and the associated seismic hazard.

There is growing evidence that friction is much lower at seismic slip velocities than RS friction laws predict [e.g., *Toro et al.*, 2003; *Rice*, 2006; *Han et al.*, 2007; *Lu et al.*, 2007, and references therein]. The presented SEM framework can be extended to include dynamic weakening mechanisms such as pore pressurization and flash heating [*Rice*, 2006, and references therein], which can be combined with RS friction to account for a wide range of seismic and aseismic slip velocities. SEM can incorporate complex 3D geometrical effects such as 3D basins and seismic Moho [*Casarotti et al.*, 2007]. Furthermore, it can be extended to include non-planar fault geometries and heterogeneous and/or non-elastic bulk properties, factors that are important for understanding fault behavior, and in particular large earthquakes.

5.7 Fault boundary matrix

The fault surface Γ consists of quadrilateral elements Γ_e inherited from hexahedral elements lying on the two sides $\Gamma_\pm$ of the fault. The matrix $\mathbf{B}$ in (5.1) is a sparse rectangular matrix obtained by assembling the contributions $\mathbf{B}_e$ from each of the fault boundary elements Γ_e that are the same for the three components of traction. The term of $\mathbf{B}_e$ associated with the GLL node with local indices (i, j) in $\Gamma_e \in \Gamma_\pm$ is

$$B^{e\pm}_{ij,ij} = \pm\omega_i\omega_j J^{ij}_e \ , \tag{5.26}$$

where ω_k denote the weights associated with the GLL integration quadrature and

$$J^{ij}_e = \left\| \frac{\partial \mathbf{x}}{\partial \xi} \times \frac{\partial \mathbf{x}}{\partial \eta} \right\| (\xi_i, \eta_j) \tag{5.27}$$

is the Jacobian of the coordinate transformation from $\mathbf{x} \in \Gamma_e$ to $\boldsymbol{\xi} = (\xi, \eta) \in [-1, 1]^2$.

The outward normal vector of the fault boundary Γ^+ is obtained by

$$\mathbf{n}(\xi, \eta) = \frac{1}{J_e} \frac{\partial \mathbf{x}}{\partial \xi} \times \frac{\partial \mathbf{x}}{\partial \eta} \ . \tag{5.28}$$

5.8 Appendix: Rupture initiation procedure

To nucleate dynamic rupture in a short period of time, we need to abruptly increase slip velocity from values below typical plate loading rate ($\sim 10^{-12}$ m/s) to coseismic ones (~ 1 m/s). To achieve this numerically, we use a perturbation of shear stress that smoothly grows from zero to its maximum amplitude $\Delta\tau_o$ over a finite time interval T, and is confined to a finite circular region of the fault of radius R. Following the approach used in *Rojas et al.* [2007] and in the 2008 SCEC code validation, we apply a horizontal shear traction perturbation of the form:

$$\Delta\tau(x, z, t) = \Delta\tau_o F(\sqrt{(x - x_o)^2 + (z - z_o)^2}) G(t) \ , \tag{5.29}$$

where

$$F(r) = \begin{cases} \exp\left[r^2/(r^2 - R^2)\right] & \text{if } r < R\ , \\ 0 & \text{if } r \geq R\ , \end{cases} \tag{5.30}$$

and

$$G(t) = \begin{cases} \exp\left[(t - T)^2/(t^2 - 2tT)\right] & \text{if } 0 < t < T\ , \\ 1 & \text{if } t \geq T\ . \end{cases} \tag{5.31}$$

The perturbation is radially symmetric, with the radial distance away from the hypocenter along the fault given by $r = \sqrt{(x - x_o)^2 + (z - z_o)^2}$. We use $R = 2.5$ km, $\Delta\tau_o = 19.0$ MPa, and $T = 0.1$ seconds.

Chapter 6

Spectral Element Modeling of Long-term Slip Histories Punctuated by Dynamic Ruptures on Rate and State Faults

In this Chapter, we develop a 2D SEM that can enable us to simulate long-term fault slip histories and that allows us to consider scenarios with heterogeneous bulk properties. Our model merges a quasi-static SEM with the fully dynamic SEM presented in Chapter 5. To validate the developed SEM approach, we compare SEM and BIM simulation results in a 2D model of small repeating earthquakes (Section 6.2). Using the developed SEM approach, we investigate the effect of variable fault-zone and bulk properties on earthquake cycles (Section 6.3). In particular, we study whether vertically stratified bulk structure can cause shallow coseismic slip deficit without the presence of a shallow velocity-strengthening region.

This Chapter is based on the manuscript in preparation by Y. Kaneko, N. Lapusta, and J.-P. Ampuero.

6.1 A quasi-static SEM algorithm for simulations of long-term deformation histories

6.1.1 Discretized elastodynamic relations

As in Chapter 5, we start from the discretized weak form of the equation of motion in its matrix form:

$$\mathbf{M}\ddot{\mathbf{u}} = -\mathbf{K}\mathbf{u} + \mathbf{B}\boldsymbol{\tau} \ , \tag{6.1}$$

where $\mathbf{M}$ and $\mathbf{K}$ are the mass and stiffness matrix respectively, $\mathbf{B}$ is the fault-boundary matrix, $\boldsymbol{\tau} = \mathbf{T} - \boldsymbol{\tau}_o$ is the relative traction vector on the fault, $\mathbf{T}$ is the total traction, and $\boldsymbol{\tau}_o$ is the traction on the fault that corresponds to the reference zero-displacement state. Vectors $\mathbf{u}$, $\dot{\mathbf{u}}$, and $\ddot{\mathbf{u}}$ collect the values of displacements, particle velocities, and accelerations, respectively, of all the computational nodes of the bulk mesh.

The SEM dynamic model presented in Chapter 5 relies on an explicit time updating scheme, the approach commonly used in SEMs for wave propagation [e.g., *Komatitsch and Vilotte*, 1998]. However, the explicit time scheme limits the maximum length of each time step by the Courant condition. For dynamic rupture simulations, the value of this time step is of the order of a fraction of a second, and hence simulating tens to thousands of years of deformation histories is not computationally feasible. To take a longer time step, one needs to use an implicit time updating scheme. SEMs with implicit schemes have been been used to solve elastic and acoustic wave equations [e.g., *Ampuero*, 2002; *Zampieri and Pavarino*, 2006].

We develop a quasi-static SEM with an adaptive time stepping and merge it with the fully dynamic SEM. We switch from one regime to the other based on the values of the maximum slip velocity on the fault. In the case of quasi-static static problems, the discretization of the weak form of the equation becomes

$$\mathbf{Ku} = \mathbf{B}\boldsymbol{\tau} \ , \tag{6.2}$$

Let us decompose the displacement values $\mathbf{u}$ into the ones on the fault, denoted by $\mathbf{u}^{\mathrm{f}}$ and ones in the medium, denoted by $\mathbf{u}^{\mathrm{m}}$. Then

$$\mathbf{K}_{11}\mathbf{u}^{\mathrm{f}} + \mathbf{K}_{12}\mathbf{u}^{\mathrm{m}} = \mathbf{B}\boldsymbol{\tau} \ , \tag{6.3}$$

$$\mathbf{K}_{21}\mathbf{u}^{\mathrm{f}} + \mathbf{K}_{22}\mathbf{u}^{\mathrm{m}} = \mathbf{0} \ , \tag{6.4}$$

where $\mathbf{K}_{11}$ and $\mathbf{K}_{12}$ are the parts of the stiffness matrix corresponding to $\mathbf{u}^{\mathrm{f}}$, and $\mathbf{K}_{21}$ and $\mathbf{K}_{22}$ are the parts corresponding to $\mathbf{u}^{\mathrm{m}}$. From (6.4), we have

$$\mathbf{K}_{22}\mathbf{u}^{\mathrm{m}} = -\mathbf{K}_{21}\mathbf{u}^{\mathrm{f}} \ . \tag{6.5}$$

Given the displacement on the fault $\mathbf{u}^{\mathrm{f}}$, one can obtain the corresponding displacement field in the medium $\mathbf{u}^{\mathrm{m}}$.

In (6.3), let us introduce $\mathbf{A} \equiv \mathbf{K}_{11}\mathbf{u}^{\mathrm{f}} + \mathbf{K}_{12}\mathbf{u}^{\mathrm{m}}$. We now write relation (6.3) for the fault nodes with the ± signs indicating the values of field variables on the two sides of the

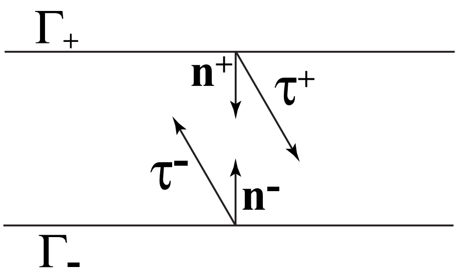

Figure 6.1: The fault divided into two non-overlapping surfaces $\Gamma_\pm$.

fault (Figure 6.1):

$$\mathbf{B}^\pm \boldsymbol{\tau}^\pm = \mathbf{A}^\pm \ . \tag{6.6}$$

Subtracting the minus side from the plus side, and using the sign convention $\boldsymbol{\tau} = -\boldsymbol{\tau}^+ = \boldsymbol{\tau}^-$, where $\boldsymbol{\tau}^\pm$ are defined with respect to the outward normal from the fault boundary $\Gamma_\pm$ (Figure 6.1), we obtain

$$\boldsymbol{\tau} = -(\mathbf{B}_+ + \mathbf{B}_-)^{-1}(\mathbf{A}_+ - \mathbf{A}_-) \ . \tag{6.7}$$

Note that $\mathbf{B}_+ = \mathbf{B}_-$ for conformal meshes. The expression (6.7) is a local relation which can be computed node by node on the fault. It is convenient to rewrite (6.7) in terms of total traction, $\mathbf{T} = \boldsymbol{\tau}_o + \boldsymbol{\tau}$:

$$\mathbf{T} = \boldsymbol{\tau}_0 + \boldsymbol{\tau} = \boldsymbol{\tau}_0 - (\mathbf{B}_+ + \mathbf{B}_-)^{-1}(\mathbf{A}_+ - \mathbf{A}_-) \ . \tag{6.8}$$

6.1.2 Updating scheme: advancing one evolution time step during quasi-static periods

We have developed an updating scheme appropriate for the rate and state fault boundary condition. Here, we discuss how values of field variables are updated over one evolution time step. Suppose that the discretized values of displacement $\mathbf{u}$ and particle velocity $\dot{\mathbf{u}}$ are known at the nth time step. To find the values of the field variables at the $(n+1)$th time step, we perform the following steps.

1. Update the values of displacements on the fault $\mathbf{u}^{\mathrm{f}}$, based on the known values at the nth time step:
$$\mathbf{u}^{*\mathrm{f}}_{n+1} = \mathbf{u}^{\mathrm{f}}_{n} + \Delta t \ \dot{\mathbf{u}}^{\mathrm{f}}_{n} \ . \tag{6.9}$$

2. Solve for displacement field in the medium $\mathbf{u}^{*\mathrm{m}}_{n+1}$ using (6.5):
$$\mathbf{K}_{22}\mathbf{u}^{*\mathrm{m}}_{n+1} = -\mathbf{K}_{21}\mathbf{u}^{*\mathrm{f}}_{n+1} \ . \tag{6.10}$$

   This is solved by a preconditioned conjugate gradient method, an iterative method for solving symmetric-positive-definite systems of equations. The algorithm we use is based on *Hestenes and Stiefel* [1952] and is summarized in *Trefethen and Bau* [1997]. Because the stiffness matrix $\mathbf{K}_{22}$ is large ($\sim 10^4$ by 10^4), a direct method such as Gaussian elimination cannot be used. Fortunately, the matrix $\mathbf{K}_{22}$ is sparse, and the product $\mathbf{K}\mathbf{u}$ is always computed at a local elemental level as in the case with the dynamic SEM (Chapter 5). This is why we use an iterative method.

3. Compute $\mathbf{A}^* = \mathbf{K}_{11}\mathbf{u}^{*\mathrm{f}}_{n+1} + \mathbf{K}_{12}\mathbf{u}^{*\mathrm{m}}_{n+1}$ and $\mathbf{T}^*_{n+1}$ in (6.8).

$$\mathbf{T}^*_{n+1} = \boldsymbol{\tau}_0 - (\mathbf{B}_+ + \mathbf{B}_-)^{-1}(\mathbf{A}^*_{+,\,n+1} - \mathbf{A}^*_{-,\,n+1}) \ . \tag{6.11}$$

4. Determine the first prediction of the state variable, θ^*_{n+1}. By integrating the evolution law (5.13) or (5.14) with the constant magnitude $\dot{\delta}_n$ of slip velocity $\dot{\boldsymbol{\delta}}_n = \mathbf{u}^+_n - \mathbf{u}^-_n$ during the time step, we obtain

$$\theta^*_{n+1} = \theta_n \exp\left(-\frac{\dot{\delta}_n \Delta t}{L}\right) + \frac{L}{\dot{\delta}_n}\left(1 - \exp\left(-\frac{\dot{\delta}_n \Delta t}{L}\right)\right) \tag{6.12}$$

for the aging law, and

$$\theta^*_{n+1} = \frac{L}{\dot{\delta}_n}\left(\frac{\dot{\delta}_n \theta_n}{L}\right)^{\exp\left(-\dot{\delta}_n \Delta t / L\right)} \tag{6.13}$$

for the slip law.

5. Find the first prediction of slip velocity $\dot{\boldsymbol{\delta}}^*_{n+1}$ by equating the magnitude of shear stress in (6.11) and strength in (5.15). The directions of shear traction vector $\mathbf{T}_{n+1}$ and slip velocity vector $\dot{\boldsymbol{\delta}}_{n+1}$ have to coincide. From (6.11), the traction $\mathbf{T}^*_{n+1}$ and $\mathbf{A}^*_{n+1}$ have the same direction. By projecting (6.11) onto that direction and using an inverted form of (5.15), we obtain

$$\dot{\delta}^*_{n+1} = \psi(T^*_{n+1}, \theta^*_{n+1}) \ . \tag{6.14}$$

Using the directional cosines constructed from the components of $\mathbf{T}^*_{n+1}$, we obtain the components of $\dot{\boldsymbol{\delta}}^*_{n+1}$.

6. Calculate the final prediction of displacement and slip on the fault, $\mathbf{u}^{**\mathrm{f}}_{n+1} = \frac{1}{2}\boldsymbol{\delta}^{**}_{n+1}$, at the $(n+1)$th time step by

$$\mathbf{u}^{**\mathrm{f}}_{n+1} = \mathbf{u}^{\mathrm{f}}_{n} + \frac{\Delta t}{2}\left(\dot{\mathbf{u}}^{\mathrm{f}}_{n} + \dot{\mathbf{u}}^{*\mathrm{f}}_{n+1}\right) \ . \tag{6.15}$$

7. Make the corresponding prediction $\mathbf{u}^{**\mathrm{m}}_{n+1}$ of the displacement in the medium using the $\mathbf{u}^{**\mathrm{f}}_{n+1}$ as in step 2.

8. Make the corresponding prediction T^{**}_{n+1} and θ^{**}_{n+1} by repeating steps 3 and 4 and by replacing $\dot{\delta}_n$ in equation (6.12) or (6.13) with $\left(\dot{\delta}_n + \dot{\delta}^*_{n+1}\right)/2$.

9. Find the final prediction $\dot{\delta}^{**}_{n+1}$ and the components of $\dot{\boldsymbol{\delta}}^{**}_{n+1}$ by repeating step 5 with T^{**}_{n+1} and θ^{**}_{n+1} instead of T^*_{n+1} and θ^*_{n+1}.

10. Declare the values of $\dot{\delta}_{n+1}$, θ_{n+1}, and T_{n+1} on the fault, and the values of displacement of the entire medium $\mathbf{u}_{n+1}$, to be equal to the predictions with the superscript double asterisks.

This scheme is second-order accurate in Δt for slip and state variable. As in the case of single spontaneous dynamic rupture (Chapter 5), its accuracy is comparable to that of BIM only when the second iteration is included.

6.2 Implementation example

6.2.1 Formulation of a 2D model

The response of faults to tectonic loading is characterized by long periods of quasi-static deformation combined with short periods of fast dynamic slip. To simulate such response, we adopt the variable time stepping of *Lapusta et al.* [2000], in which the time step is set to be inversely proportional to slip velocity on the fault as described in Appendix 6.5. As a result, relatively large time steps, a fraction of a year, are used in the interseismic periods, while small time steps, a fraction of a second or smaller, are used to simulate fast seismic slip. Note that the stability of the stepping procedure relies on the presence of the positive direct effect in the rate and state formulation, the feature that has ample laboratory confirmation.

The updating scheme illustrated in the previous section can be merged with the one for the dynamic SEM shown in Chapter 5. The main challenge in merging these two schemes is to find proper criteria for switching from the quasi-static to dynamic scheme and vice versa. Prior to the onset of earthquakes (or during nucleation processes), slip velocities abruptly increase from values much smaller than typical plate loading rates ($\sim 10^{-10}$ - 10^{-9} m/s) to coseismic values (∼1 - 10 m/s), where inertial effects become dominant. Hence we switch from one scheme to the other based on the values of the maximum slip velocity, which, for the problems discussed below, are $\dot{\delta}^{\mathrm{QD}}_{\mathrm{max}} = 0.5$ mm/s for switching from the quasi-static to dynamic scheme, and $\dot{\delta}^{\mathrm{DQ}}_{\mathrm{max}} = 0.2$ mm/s from the dynamic to quasi-static scheme. The selection of these values ensures that the field quantities change smoothly at the time of

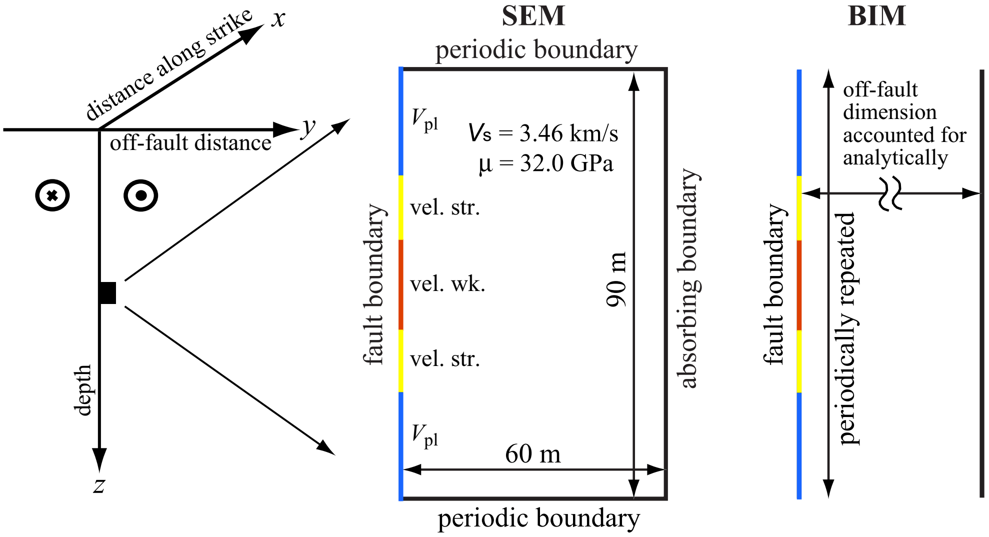

Figure 6.2: 2D fault models of a vertical strike-slip fault. Small repeating earthquakes at seismogenic depths in a region indicated by a black rectangle are modeled using these models. By symmetry consideration, the medium across the fault boundary has equal and opposite motion.

the switch, that the time step is already equal to the minimum time step $\Delta t_{\min}$ given in Appendix 6.5, and that the results compare well with BIM methods as discussed below. More work is needed to formulate the criteria in terms of the magnitude of inertial terms with respect to other forces in the problem.

To demonstrate how the ideas outlined so far are combined to produce long-term deformation histories, let us consider response of a 2D fault model (Figure 6.2). In this model, a vertical strike-slip fault is embedded in an elastic medium. On the fault, a potentially seismogenic patch borders regions steadily moving with a prescribed slip rate $V_{\rm pl} = 2$ mm/yr, as illustrated in Figure 6.2. That steady motion provides loading in the model. The fault motion is in the along-strike direction x, but only variations with depth z are considered, so that the fault behavior is described by strike-parallel slip $\delta(z,t)$, slip velocity (or slip rate) $\dot{\delta}(z,t) = \partial\delta(z,t)/\partial t$, and the relevant component of shear stress $T(z,t)$.

It is convenient to express the formulae in terms of variables $(u - V_{\mathrm{pl}}t/2)$ and $(\dot{u} - V_{\mathrm{pl}}/2)$, in which case $\tau_0(z,t)$ becomes independent of time and equal to the initial stress $\tau_0(z)$. This approach was used for the BIM model of *Lapusta et al.* [2000]. For the 2D problems we consider here, the medium across the fault boundary has equal and opposite motion by symmetry consideration. Then the relations (5.11) and (6.8) on the fault become

$$T(z,t) = \tau_0(z) + \tilde{T}(z,t) - Z(z)\left(\dot{\delta}(z,t) - V_{\mathrm{pl}}\right) \tag{6.16}$$

for the dynamic scheme, and

$$T(z,t) = \tau_0(z) - \frac{1}{2B(z)}\left\{K_{11}(y,z,t)\left[u^{\mathrm{f}}(z,t) - \frac{V_{\mathrm{pl}}t}{2}\right] + K_{12}(y,z,t)\left[u^{\mathrm{m}}(z,t) - \frac{V_{\mathrm{pl}}t}{2}\right]\right\} \tag{6.17}$$

for the quasi-static scheme. Note that our mesh is conformal and hence $B = B_+ = B_-$.

The SEM model consists of a 90 km by 60 km rectangular domain (Figure 6.2). The domain is replicated using periodic boundary conditions on both sides of the domain (Figure 6.2). The fault boundary obeys rate and state (RS) friction with the aging law of state variable evolution. The model contains variations in steady-state friction properties that create rheological transitions (Figure 6.3). The parameters used in the simulations are listed in Table 6.1. The effective normal stress $\bar{\sigma}$ and characteristic slip L are uniform along the fault.

We use the criteria for spatial discretizations developed in the work by *Lapusta and Liu* [2009], which showed that resolving a cohesive zone size during the dynamic rupture propagation is a more stringent requirement than resolving the nucleation size, for the

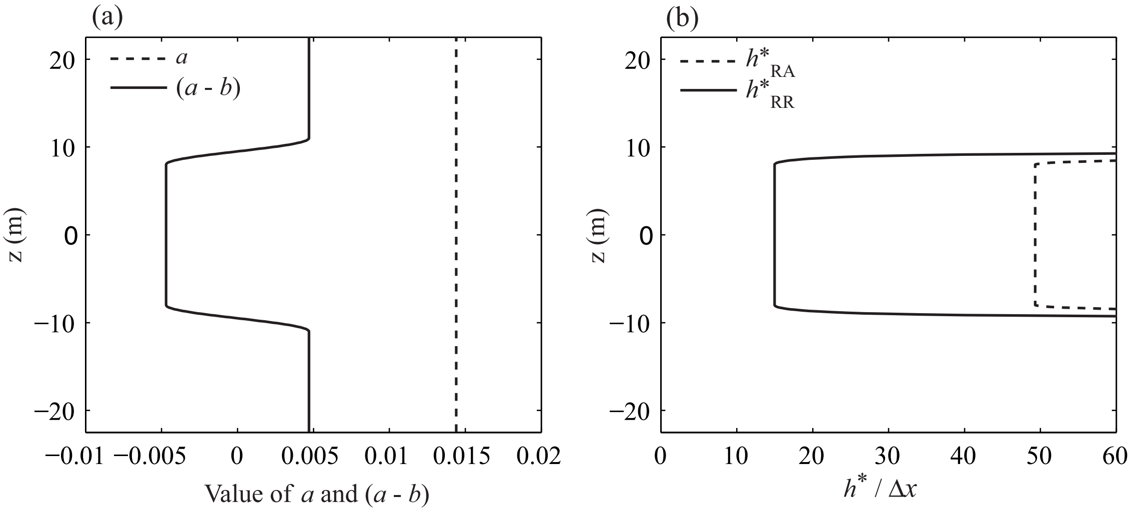

Figure 6.3: (a) Depth-variable distribution of friction parameters a and $(a-b)$. (b) Distribution of the ratio $h^*/\Delta x$. Two theoretical estimates h^* of the nucleation size by Rubin-Ampuero (RA) and Rice-Ruina (RR) are shown.

Table 6.1: Parameters used in the 2D SEM and 2D BIM models of small repeating earthquakes. The indicated value of b is valid for the steady-state velocity-weakening region in Figure 6.2.

Parameter	Symbol	Value
Shear modulus	μ	32 GPa
Shear wave speed	V_s	3.46 km/s
Reference slip rate	$\dot{\delta}_0$	10^{-6} m/s
Reference friction coefficient	f_0	0.6
Characteristic slip distance	L	84 μm
Effective normal stress	$\bar{\sigma}$	120 MPa
Rate and state parameter a	a	0.0144
Rate and state parameter b	b	0.0191

aging formulation of rate and state friction and typical rate and state parameters. In our simulations, we use $\Delta x = 0.25$ m, which results in $\Lambda_0/\Delta x \approx \mu L/(b\bar{\sigma}\Delta x) \approx 5$ where Λ_0 is the cohesive zone size at the rupture speed $c \rightarrow 0^+$. Such resolution has shown to be adequate in the work of *Day et al.* [2005] and *Lapusta and Liu* [2009], and it leads to stable results in our simulations that do not change due to finer discretizations. The selected spatial discretization corresponds to $h^*_{RA}/\Delta x \approx 50$ (Figure 6.3b), where h^*_{RA} is the estimate of the nucleation size obtained by *Rubin and Ampuero* [2005] for $a/b \gtrsim 0.5$, which points to more than adequate resolution of nucleation processes.

6.2.2 Comparison of simulation results obtained with 2D SEM and 2D BIM

To assess the accuracy of numerical results, we conduct comparison of simulation results obtained using the quasi-static/dynamic combined SEM model with a BIM model. The BIM model used for the comparison is based on the BIM spectral formulation of *Lapusta et al.* [2000] that resolves all stages of each earthquake episode under a single computational scheme. Figure 6.2 illustrates the geometry of the antiplane SEM and BIM models. In BIM, wave propagation is analytically accounted for by boundary integral expressions. The fault is repeated periodically, as in the SEM model.

Earthquake sequences simulated in SEM and BIM models are shown and compared in Figure 6.4. The solid lines are plotted every 0.5 years and show the continuous slow sliding (creep) of the steady-state velocity-strengthening regions. That slow slip creates stress concentration at its tip and penetrates into the velocity-weakening region. In due time, an

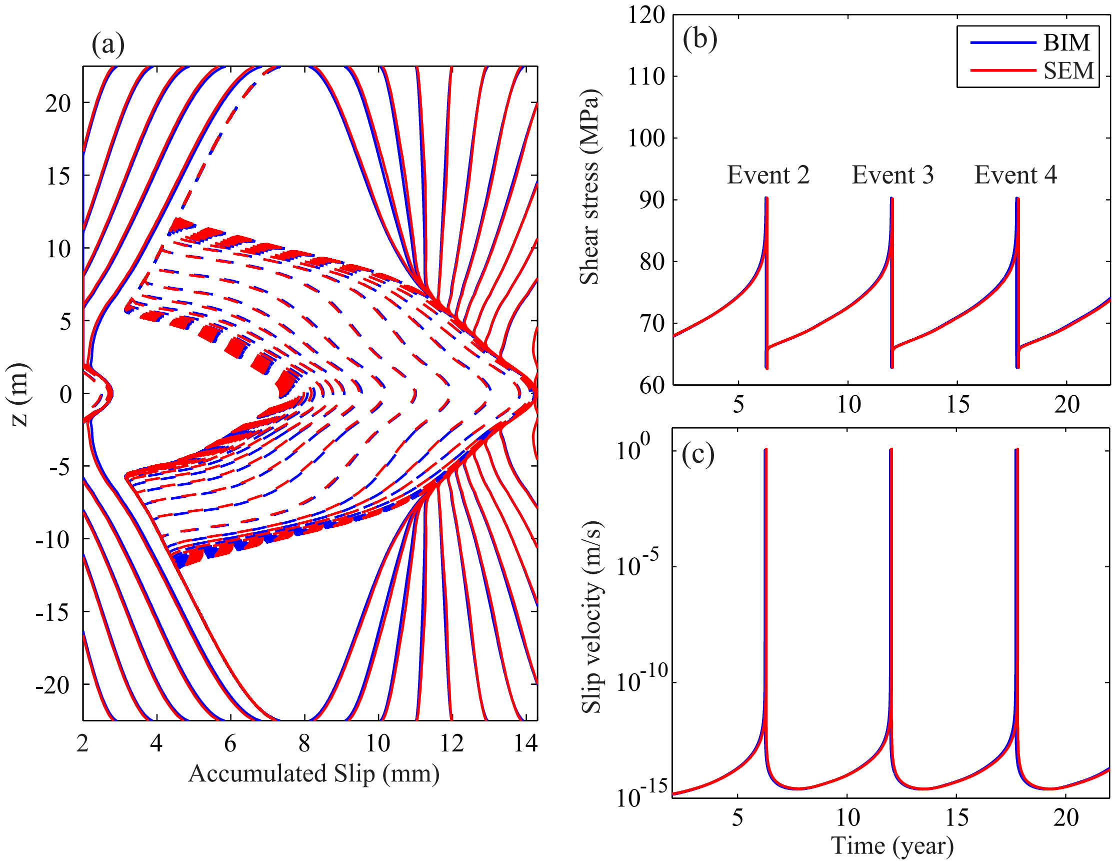

Figure 6.4: Comparison of earthquake sequences simulated in BIM and the combined quasi-static/dynamic SEM. (a) Solid lines show slip accumulation every 0.5 years for BIM (blue) and SEM (red). Dashed lines are intended to capture dynamic events and are plotted every 1 millisecond (ms) during the simulated earthquakes (or $\dot{\delta}_{\max} > 1$ cm/s). Evolution of aseismic slip and seismic slip of the 2nd event are shown. Spatial distributions of slip contours in these models agree very well. (b) Shear-stress and (c) slip-velocity histories at the center of the fault. The 2nd, 3rd, and 4th earthquake events are shown. The timings of earthquake events in these models are nearly identical as quantified in the text, validating our quasi-static/dynamic combined SEM implementation.

earthquake rupture nucleates and propagates bilaterally; its progression is shown by dashed lines. After an earthquake arrests, the velocity-strengthening region experiences accelerated sliding, or afterslip, due to the transferred stress. The interseismic period between two successive events is 6 years. The overall agreement of spatial slip distributions between two models during coseismic as well as interseismic periods validates our developed SEM approach (Figure 6.4a). The histories of shear stress and slip velocity at the center of the fault in these models are virtually identical, and the timings of the onset ($\dot{\delta}_{\max} > 1$ cm/s) of the 4th seismic events in these models differ by 0.46% (Figure 6.4b,c). The agreement is very good given that, in the SEM simulation, there are a total of $\sim$40,000 adaptive time steps, each of which includes 1 to 500 conjugate gradient iterations. To make sure that the solution is accurate, we have checked that the result of a BIM simulation with a twice higher resolution shows identical slip patterns and timings of seismic events, confirming that the results here are grid independent.

There are several interesting observations in the outcome of this particular example. Figure 6.5 shows the evolution of the displacement and velocity fields during the quasi-static and dynamic periods in the SEM model. In Figure 6.5a, warm colors indicate a larger amount of displacement relative to the displacement given by the plate loading, whereas cold colors correspond to a smaller amount of displacement. About one minute before the onset of the seismic event, the displacement field localizes near the eventual nucleation site. The change in strain field associated with this localization can be detected if a strain-meter were placed at an off-distance comparable to the size of the nucleation region. This is why observations of premonitory slip prior to the eventual mainshock are difficult, consistent with the study by *Tullis* [1996]. After the seismic event that occurred between the 4th and 5th panels in Figure 6.5a, the red-colored region gradually expands due to afterslip on the velocity-strengthening segments of the fault. The corresponding change in the displacement field for the afterslip is much larger than that for the nucleation process. Therefore, one should look for signals associated with afterslip of small repeating earthquakes before searching for signals for the nucleation process. In Chapter 2, we have shown several implications for the presence of a velocity-strengthening patch: the termination of coseismic ruptures, decreased values of interseismic coupling, the decrease of seismic potency rates, and the occurrence of afterslip. Another physical implication is the formation of healing waves that propagate into a bulk, when the rupture front encounters a velocity-strengthening region (Figure 6.5b).

6.3 Effect of variable bulk properties on earthquake cycles: Can vertically stratified bulk structure cause shallow coseismic slip deficit?

Using the developed formulation, we investigate the effects of variable bulk properties combined with different fault rheologies on shallow coseismic slip deficit inferred from earthquake inversions [*Fialko et al.*, 2005]. In Chapter 5, we showed that such deficit can be caused by a shallow fault region of velocity-strengthening friction. Another candidate mechanism is low initial stress in low-rigidity shallow bulk materials resulting from uniform tectonic strain [*Rybicki and Yamashita*, 1998]. Here we investigate both mechanisms

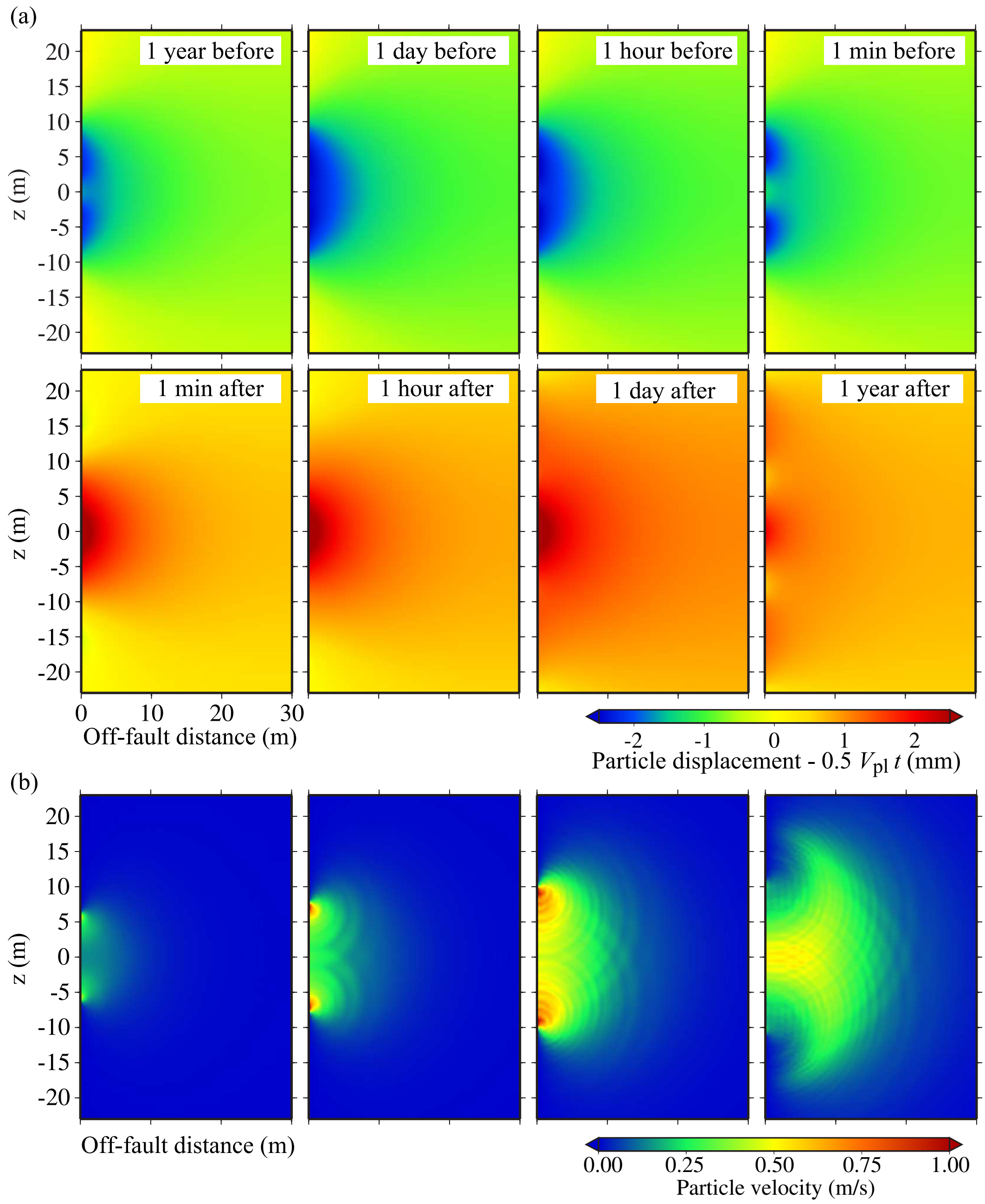

Figure 6.5: (a) Snapshots of displacement field (minus plate loading) in the 2D SEM model. (b) Snapshots of SH particle velocity field every 2 ms during the seismic event.

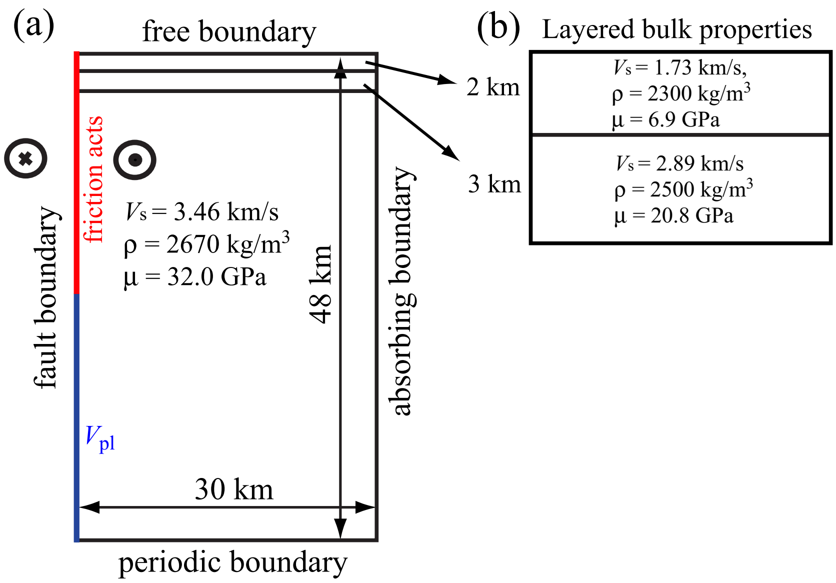

Figure 6.6: 2D SEM model of a vertical strike-slip fault. (a) A sketch illustrating the antiplane problem for the 2D SEM model. (b) Layered bulk properties used in some scenarios we consider.

using the developed SEM.

We model earthquake sequences on a planar vertical strike-slip fault embedded into an elastic half-space (Figure 6.6). The setup is similar to the depth-variable model of *Lapusta et al.* [2000], where friction acts in the top 24 km of the fault and its deeper extension moves with a prescribed plate rate of 35 mm/year. The physical parameters of the simulations presented in this work are shown in Figure 6.6 and Figure 6.7. The value of L used is 8 mm, larger than the laboratory values of the order of 1 - 100 μm, to make large-scale simulations numerically tractable. The variation of friction parameters a and b with depth shown in Figure 6.7a is similar to the one in *Rice* [1993] and *Lapusta et al.* [2000]; it is derived from laboratory experiments [*Blanpied et al.*, 1995]. The region between 3.0 km and 15.3 km has steady-state velocity-weakening properties. The transition from steady-state velocity weakening to steady-state velocity strengthening at 15.3-km depth is due to

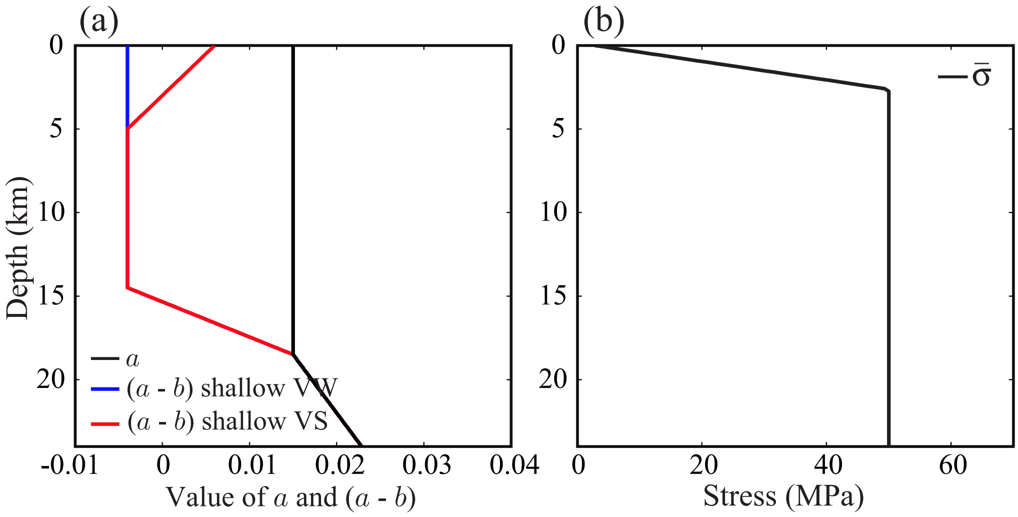

Figure 6.7: (a) Depth-variable distribution of the parameters $(a - b)$ and a. (b) Depth-variable distribution of effective normal stress $\bar{\sigma}$.

temperature increase with depth. The effective normal stress $\bar{\sigma}$ becomes constant and equal to 50 MPa at depths larger than 2.6 km (Figure 6.7b), due to the assumption that fluid over-pressure prevents further increase of $\bar{\sigma}$ with depth [*Rice*, 1993; *Ben-Zion and Rice*, 1997].

We consider four different scenarios of earthquake sequences in: (i) homogeneous bulk structure without the shallow velocity-strengthening fault patch, (ii) layered bulk structure without the shallow velocity-strengthening fault patch, (iii) homogeneous bulk structure with the shallow velocity-strengthening fault patch, and (iv) layered bulk structure with the shallow velocity-strengthening fault patch. The layered bulk model approximately corresponds to the 1D Parkfield velocity structure down to the depth of ∼15 km used in the study by *Custódio et al.* [2005]. The scenarios with the velocity-strengthening patch at depths less than 3.0 km (Figure 6.7a) are motivated by laboratory experiments and field observations as discussed in Chapter 1.

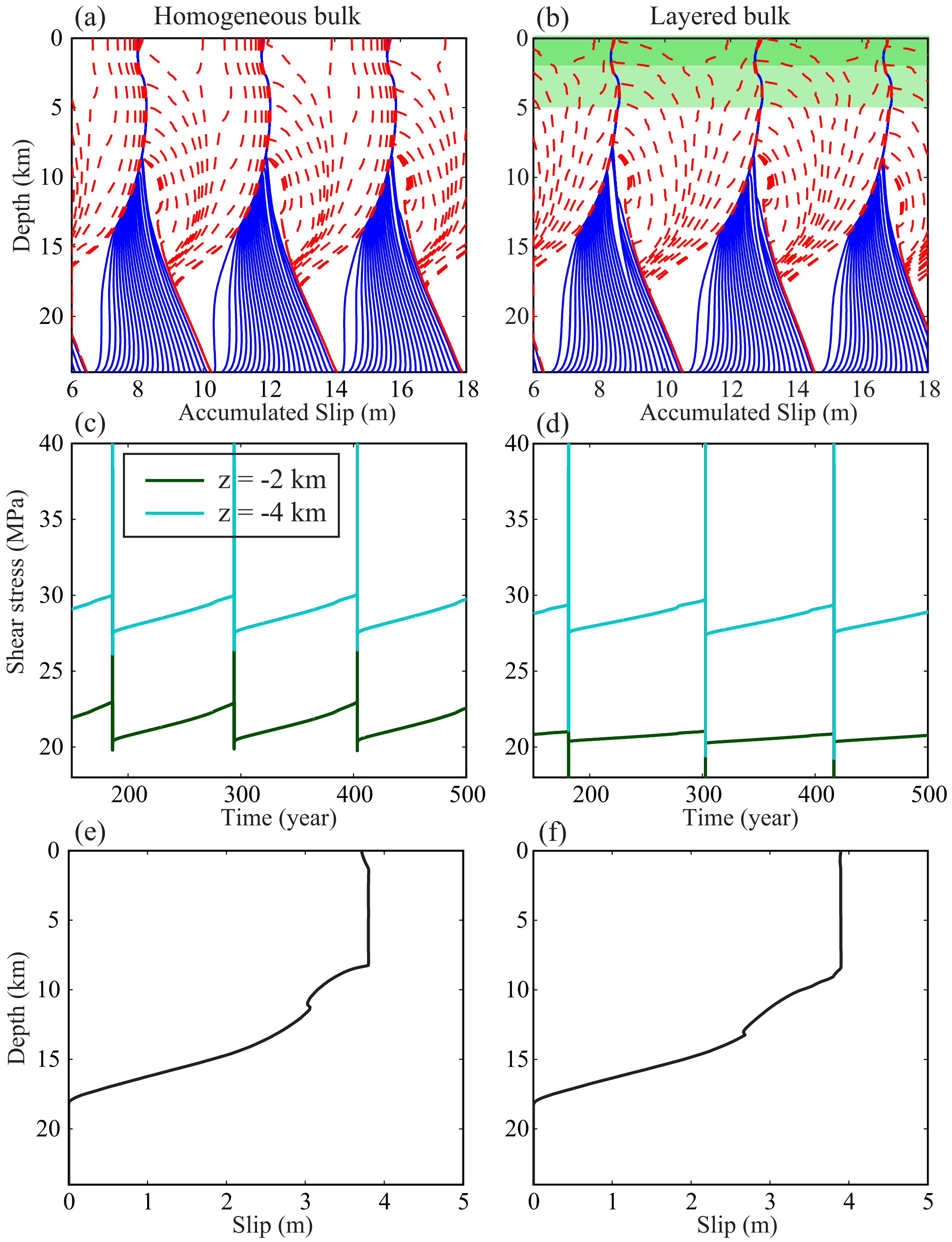

Figure 6.8: Simulated earthquake sequences and event characteristics of models with: (a), (c), (e) homogeneous bulk structure without the shallow velocity-strengthening fault patch, and (b), (d), (f) layered bulk structure without the shallow velocity-strengthening fault patch. (a), (b) Solid lines show slip accumulation every 5 years. Dashed lines are intended to capture dynamic events and are plotted every 1 second during the simulated earthquakes (for $\dot{\delta}_{\max} > 1$ cm/s). (c), (d) Shear stress evolution at two different depths ($z = -2, \ -4$ km). (e), (f) Simulated seismic slip of representative events.

Figure 6.8a,b show earthquake sequences simulated in the 2D SEM model for scenarios (i) and (ii). The solid lines are plotted every 5 years and show the continuous slow sliding (creep) of the steady-state velocity-strengthening region at depth. That slow slip creates stress concentration at its tip and penetrates into the velocity-weakening region. In due time, an earthquake nucleates close to the transition. We show the progression of earthquakes with dashed lines plotted every second.

The scenarios with homogeneous and layered bulk do not lead to shallow coseismic slip deficit in this particular examples (Figure 6.8e,f). From the evolution of shear stress, the stress accumulation rates in the lower-rigidity materials during the interseismic periods are smaller than those in the materials with higher rigidity (Figure 6.8c,d). However, the coseismic slip rates get amplified in the low-rigidity materials, resulting in the net effect on slip being nearly zero. Note that the levels of the interseismic shear stress are different at $z = -2$ and -4 km due to the depth-dependent effective normal stress (Figure 6.7b).

Figure 6.9a,b show earthquake sequences simulated in the 2D SEM model for scenarios (iii) and (iv). The presence of the shallow velocity-strengthening patch lead to shallow coseismic slip deficit regardless of the properties of the bulk (Figure 6.9e,f). Due to the interseismic creep and afterslip on the shallow velocity-strengthening region, the stress accumulation rates during the interseismic periods are very small in both scenarios. Hence the coseismic slip at the shallow parts is driven by the dynamic stress supplied by the incoming ruptures propagating updip.

The results here suggest that coseismic slip deficit can be caused by the presence of a shallow velocity-strengthening region, but not by that of low-rigidity shallow bulk materi-

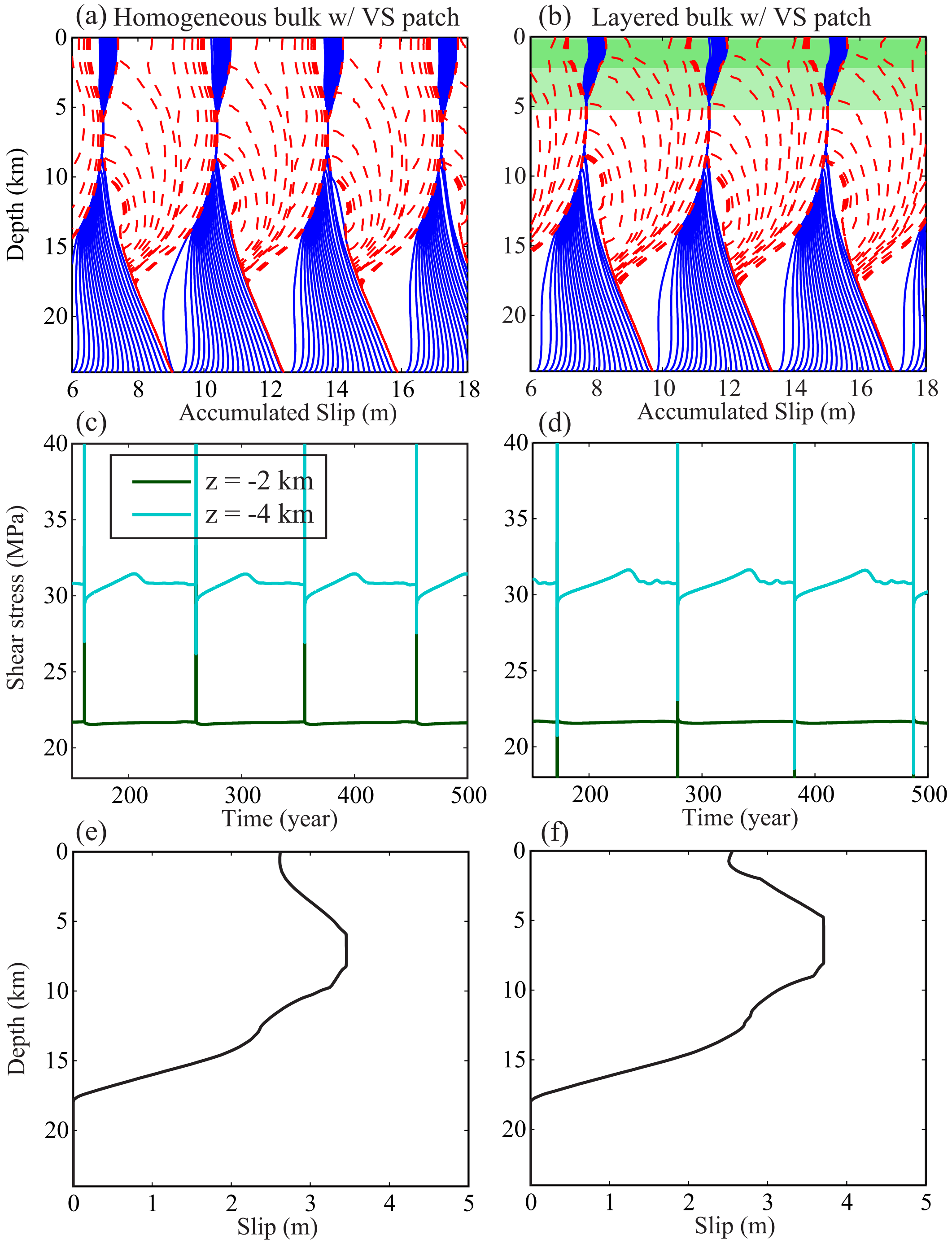

Figure 6.9: Simulated earthquake sequences and event characteristics of models with: (a), (c), (e) homogeneous bulk structure with the shallow velocity-strengthening fault patch, and (b), (d), (f) layered bulk structure with the shallow velocity-strengthening fault patch. Panels and lines have the same meaning as in Figure 6.8.

als. In a model embedded in elastic media, the accumulated slip is equal to the sum of co-, inter-, and postseismic slip. On velocity-weakening faults accommodating little inter- and postseismic slip, the coseismic slip at a given point has to catch up with that on the rest of the fault plane. Hence the cancellation of the net effect of dynamic amplification and low interseismic stress accumulation in Figure 6.8 is reasonable. The studies by *Rybicki* [1992] and *Rybicki and Yamashita* [1998], which proposed that shallow coseismic deficit can be caused by the presence of low-rigidity materials, did not consider dynamic amplification of coseismic slip, even though they considered a wider range of conditions. While exploring the wider range of parameters is our next goal, our conclusions should still be valid, unless certain conditions lead to significant interseismic creep or afterslip on faults with velocity-weakening friction.

6.4 Conclusions

We have developed a 2D SEM algorithm for simulating long-term fault slip histories on rate and state faults. We have set up an antiplane benchmark problem and validate the developed SEM approach by comparing SEM and BIM simulation results in a 2D model of small repeating earthquakes. Our approach allows us to study seismic events that naturally develop in our models, with conditions before the nucleation originating from the previous stages of earthquake occurrence and not from arbitrarily selected initial conditions that one would need to impose to study only one instance of an earthquake. The SEM model can also allow for more flexibility in fault geometry and bulk properties in long-term simulations of fault slip. Furthermore, while the methodology is presented using the 2D antiplane problem, it can be readily extended to the 2D in-plane and 3D problems.

Using the developed formulation, we have investigated the effects of variable fault-zone bulk properties combined with different fault rheologies on nature of shallow coseismic slip deficit. For the set of parameters we have considered, low-rigidity shallow bulk materials do not lead to coseismic slip deficit. While the low-rigidity materials do cause lower interseismic stress accumulation, they also cause dynamic amplification of coseismic slip rates, with the net effect on slip being nearly zero. At the same time, the addition of velocity-strengthening friction to shallow parts of the fault leads to coseismic slip deficit in all cases we have considered.

6.5 Appendix: Variable evolution time step in 2D antiplane problems

Simulations of long-term deformation histories with periods of rapid dynamic slip (earthquakes) requires time steps that change by orders of magnitude. For our quasi-static/dynamic combined SEM model, we adopt the time-stepping scheme developed for BIM by *Lapusta et al.* [2000] for a 2D antiplane problem. This scheme works well for our 2D SEM model. Note that the maximum time step is limited by the Courant condition and constant in the dynamic SEM. The variable time step Δt is chosen as:

$$\Delta t = \max\{\Delta t_{\min}, \Delta t_{\mathrm{ev}}\} \ , \tag{6.18}$$

where $\Delta t_{\min}$ is the minimum time step, and Δt_{ev} depends on slip velocity at each time step. The minimum time step is set by the Courant condition and given by

$$\Delta t_{\min} = \gamma \Delta x_{\min}/c_s \ , \tag{6.19}$$

where $\gamma = 0.6$ is used in our 2D antiplane problem. The same condition is used for modeling single dynamic ruptures in the 2D antiplane test problem in Chapter 5. The time step Δt_{ev} is set to be inversely proportional to slip velocity:

$$\Delta t_{\mathrm{ev}} = \min[\xi_i L_i/\dot{\delta}_i] \ , \tag{6.20}$$

where L_i, $\dot{\delta}_i$, and ξ_i are the characteristic slip, the current slip velocity, and a prescribed parameter for the ith fault node of the discretized domain, respectively. ξ_i is a function of friction properties from linear stability analysis [*Lapusta et al.*, 2000], and it is constrained to satisfy $\xi_i \leq \xi_c$, where ξ_c is a constant, to ensure that slip at each time step does not exceed $\xi_c L_i$. As in *Lapusta et al.* [2000], we use $\xi_c = 1/2$ in our 2D SEM and BIM models used in this Chapter.

Bibliography

Aagaard, B. T., T. H. Heaton, and J. F. Hall, Dynamic earthquake ruptures in the presence of lithostatic normal stresses: Implications for friction models and heat production, *Bull. Seismol. Soc. Am., 91(6)*, 11,765–11,796, 2001.

Ampuero, J.-P., Etude physique et numérique de la nucléation des séismes, Ph.D. thesis, Univ. Paris 7, Denis Diderot, Paris, 2002.

Ampuero, J.-P., and A. M. Rubin, Earthquake nucleation on rate and state faults - Aging and slip laws, *J. Geophys. Res., 113*, B01302, doi:10.1029/2007JB005082, 2008.

Andrews, D. J., Test of two methods for faulting in finite-difference calculations, *Bull. Seismol. Soc. Am., 89(4)*, 931–937, 1999.

Baba, T., K. Hirata, T. Hori, and H. Sakaguchi, Offshore geodetic data conducive to the estimation of the afterslip distribution following the 2003 Tokachi-oki earthquake, *Earth Planet. Sci. Lett., 241*, 281–292, 2006.

Bayart, E., A. M. Rubin, and C. Marone, Evolution of fault friction following large velocity jumps, *EOS Trans. Am. Geophys. Union, 87(52)*, Fall Meet. Suppl., S31A–0180, 2006.

Belardinelli, M. E., M. Cocco, O. Coutant, and F. Cotton, Redistribution of dynamic stress during coseismic ruptures: Evidence for fault interaction and earthquake triggering, *J. Geophys. Res.*, *104*, 14,925–14,945, 1999.

Ben-Zion, Y., and V. Lyakhovsky, Analysis of aftershocks in a lithospheric model with seismogenic zone governed by damage rheology, *Geophys. J. Int.*, *165*, 197–210, 2006.

Ben-Zion, Y., and J. R. Rice, Dynamic simulations of slip on a smooth fault in an elastic solid, *J. Geophys. Res.*, *102*, 17,771–17,784, 1997.

Benioff, H., Earthquakes and Rock Creep, *Bull. Seismol. Soc. Am.*, *41*, 31–62, 1951.

Beroza, G. C., and T. Mikumo, Short slip duration in dynamic rupture in the presence of heterogeneous fault properties, *J. Geophys. Res.*, *101*, 22,449–22,460, 1996.

Bilek, S. L., and T. Lay, Tsunami earthquakes possibly widespread manifestations of frictional conditional stability, *J. Geophys. Res.*, *109*, B09308, doi:10.1029/2004JB003039, 2002.

Bilek, S. L., T. Lay, and L. J. Ruff, Radiated seismic energy and earthquake source duration variations from teleseismic source time functions for shallow subduction zone thrust earthquakes, *J. Geophys. Res.*, *109*, B09308, doi:10.1029/2004JB003039, 2004.

Blanpied, M. L., D. A. Lockner, and J. D. Byerlee, Fault stability inferred from granite sliding experiments at hydrothermal conditions, *Geophys. Res. Lett.*, *18*, 609–612, 1991.

Blanpied, M. L., D. A. Lockner, and J. D. Byerlee, Frictional slip of granite at hydrothermal conditions, *J. Geophys. Res.*, *100*, 13,045–13,064, 1995.

Blanpied, M. L., C. J. Marone, and D. A. Lockner, Quantitative measure of the variation in fault rheology due to fluid-rock interactions, *J. Geophys. Res.*, *103*, 9,691–9,712, 1998.

Bollinger, L., J.-P. Avouac, R. Cattin, M. R. Marone, and D. A. Pandey, Stress buildup in the Himalaya, *J. Geophys. Res.*, *109*, B11405, doi:10.1029/2003JB002911, 2004.

Bosl, W. J., and A. Nur, Aftershocks and pore fluid diffusion following the 1992 Landers earthquake, *J. Geophys. Res.*, *107*(B12), 2366, doi:10.1029/2001JB000155, 2002.

Bourouis, S., and P. Bernard, Evidence for coupled seismic and aseismic fault slip during water injection in the geothermal site of Soultz (France), and implications for seismogenic transients, *Geophys. J. Int.*, *169*, 723–732, 2007.

Briggs, R., et al., Deformation and Slip Along the Sunda Megathrust in the Great 2005 Nias-Simeulue Earthquake, *Science*, *311*, 1,897 – 1,901, doi:10.1126/science.1122602, 2006.

Broberg, K. B., *Cracks and Fracture*, Elsevier, New York, 1999.

Bürgmann, R., M. G. Kogan, G. M. Steblov, G. Hilley, V. E. Levin, and E. Apel, Interseismic coupling and asperity distribution along the Kamchatka subduction zone, *J. Geophys. Res.*, *110*(B7), doi:10.1029/2005JB003648, 2005.

Casarotti, E., M. Stupazzini, S.-J. Lee, D. Komatitsch, A. Piersanti, and J. Tromp, CUBIT and seismic wave propagation based upon the spectral-element method: An advanced unstructured mesher for complex 3D geological media, in *Proceedings of the 16th International Meshing Roundtable*, Springer, New York, New York, 2007.

Chaljub, E., D. Komatitsch, J.-P. Vilotte, Y. Capdeville, B. Valette, and G. Festa, Spectral Element Analysis in Seismology, in *Advances in Wave Propagation in Heterogeneous Media,* edited by Ru-Shan Wu and Valérie Maupin, Advances in Geophysics, Elsevier, *48*, 365–419, 2007.

Chen, T., and N. Lapusta, Scaling of small repeating earthquakes explained by interaction of seismic and aseismic slip in a rate and state fault model, *J. Geophys. Res.*, *114*, B01311, doi:10.1029/2008JB005749, 2009.

Chlieh, M., J.-P. Avouac, K. Sieh, D. H. Natawidjaja, and J. Galetzka, Heterogeneous coupling of the Sumatran megathrust constrained by geodetic and paleogeodetic measurements, *J. Geophys. Res.*, *113*, B05305, doi:10.1029/2007JB004981, 2008.

Chlieh, M., et al., Coseismic slip and afterslip of the Great (Mw 9.15) Sumatra-Andaman Earthquake of 2004, *Bull. Seismol. Soc. Am.*, *97*, doi:10.1785/0120050631, 2007.

Clayton, R., and B. Engquist, Absorbing boundary conditions for acoustic and elastic wave equations, *Bull. Seismol. Soc. Am.*, *67,* 1,529–1,540, 1977.

Cochard, A., and R. Madariaga, Complexity of seismicity due to highly rate-dependent friction, *J. Geophys. Res.*, *101*, 25,321–25,336, 1996.

Custódio, S., P. Liu, and R. J. Archuleta, The 2004 $\mathrm{M_w}$6.0 Parkfield, California, earthquake: Inversion of near-source ground motion using multiple data sets, *Geophys. Res. Lett.*, *32*, L23312, doi:10.1029/2005GL024417, 2005.

Daniel, G., D. Marsan, and M. Bouchon, Earthquake triggering in southern Iceland following the June 2000 Ms 6.6 doublet, *J. Geophys. Res.*, *113*, B05310, doi:10.1029/2007JB005107, 2008.

Day, S. M., Three-dimensional finite difference simulation of fault dynamics: Rectangular faults with fixed rupture velocity, *Bull. Seismol. Soc. Am.*, *72*, 705–727, 1982.

Day, S. M., L. A. Dalguer, N. Lapusta, and Y. Liu, Comparison of finite difference and boundary integral solutions to three-dimensional spontaneous rupture, *J. Geophys. Res.*, *110*, B12307, doi:10.1029/2005JB003813, 2005.

Day, S. M., S. H. Gonzalez, R. Anooshehpoor, and J. N. Brune, Scale-model and numerical simulations of near-fault seismic directivity, *Bull. Seismol. Soc. Am.*, *98*, doi:10.1785/0120070190, 2008.

Dieterich, J. H., Time-dependent friction and the mechanics of stick-slip, *J. Geophys. Res.*, *116*, 790–806, 1978.

Dieterich, J. H., Modeling of rock friction: 1. Experimental results and constitutive equations, *J. Geophys. Res.*, *84*, 2,161–2,168, 1979.

Dieterich, J. H., Earthquake nucleation on faults with rate- and state-dependent strength, *Tectonophysics*, *211*, 115–134, 1992.

Dieterich, J. H., A constitutive law for rate of earthquake production and its application to earthquake clustering, *J. Geophys. Res.*, *99*(B2), 2601–2618, 1994.

Dieterich, J. H., and B. H. Kilgore, Direct observation of frictional contacts: new insights for state-dependent properties, *Pure Appl. Geophys.*, *143*, 283–302, 1994.

Dieterich, J. H., and B. H. Kilgore, Implications of fault constitutive properties for earthquake prediction, *Proc. Natl. Acad. Sci. U.S.A.*, p. 93, 1996.

Dmowska, R., and L. C. Lovison, Influence of Asperities Along Subduction Interfaces on the Stressing and Seismicity of Adjacent Areas, *Tectonophysics*, *211*, 23–43, 1992.

Felzer, K. R., and E. E. Brodsky, Decay of aftershock density with distance indicates triggering by dynamic stress, *Nature*, *441*, 735–738, 2006.

Festa, G., and J. P. Vilotte, The Newmark scheme as velocity-stress time-staggering: an efficient PML implementation for spectral element simulations of elastodynamics, *Geophys. J. Int.*, *161*, 789–812, 2005.

Festa, G., and J. P. Vilotte, Influence of the rupture initiation on the intersonic transition: Crack-like versus pulse-like modes, *Geophys. Res. Lett.*, *33(15)*, L15,320, 2006.

Fialko, Y., D. Sandwell, M. Simons, and P. Rosen, Three-dimensional deformation caused by the Bam, Iran, earthquake and the origin of shallow slip deficit, *Nature*, *435*, doi: 10.1038/nature.03425, 2005.

Fournier, T. J., and J. T. Freymueller, Transition from locked to creeping subduction in the Shumagin region, *Geophys. Res. Lett.*, *34*, L06303, doi:10.1029/2006GL029073, 2007.

Freed, A. M., and J. Lin, Delayed triggering of the 1999 Hector Mine earthquake by viscoelastic stress transfer, *Nature*, *411*, 180–183, 2001.

Freymueller, J. T., S. C. Cohen, and H. J. Fletcher, Spatial variations in present-day deformation, Kenai Peninsula, Alaska, and their implications, *J. Geophys. Res.*, *105*, 8,079–8,101, 2000.

Gomberg, J., The failure of earthquake failure models, *J. Geophys. Res.*, *106*(B1), 16,253–16,263, 2001.

Gomberg, J., N. M. Beeler, M. L. Blanpied, and P. Bodin, Earthquake triggering by transient and static deformations, *J. Geophys. Res.*, *103*, 24,411–24,426, 1998.

Gomberg, J., N. M. Beeler, and M. L. Blanpied, On rate-state and Coulomb failure models, *J. Geophys. Res.*, *105*(B4), 7,857–7,871, 2000.

Gomberg, J., P. Bodin, and P. A. Reasenberg, Observing earthquakes triggered in the near field by dynamic deformations, *Bull. Seismol. Soc. Am.*, *93*, 118–138, 2003.

Gomberg, J., P. Reasenberg, M. Cocco, and M. E. Belardinelli, A frictional population model of seismicity rate change, *J. Geophys. Res.*, *110*, B05S03, doi:10.1029/2004JB003404, 2005.

Gross, S., and R. Bürgmann, Rate and state of background stress estimated from the aftershocks of the 1989 Loma Prieta, California earthquake, *J. Geophys. Res.*, *103*, 4,915–4,927, 1998.

Gross, S., and C. Kisslinger, Estimating tectonic stress rate and state with Landers aftershocks, *J. Geophys. Res.*, *102*, 7,603–7,612, 1997.

Gu, J. C., J. R. Rice, A. L. Ruina, and S. T. Tse, Slip motion and stability of a single degree of freedom elastic system with rate and state dependent friction, *J. Mech. Phys. Solids, 32*, 167–196, 1984.

Han, R., T. Shimamoto, T. Hirose, J.-H. Ree, and J. Ando, Ultralow friction of carbonate faults caused by thermal decomposition, *Science, 316*, doi:10.1126/science.1139763, 2007.

Haney, M., R. S. J.-P. Ampuero, and R. Hofmann, Spectral element modeling of fault-plane reflections arising from fluid pressure distributions, *Geophys. J. Int.*, *170(2)*, 933–951, 2007.

Harris, R. A., et al., The SCEC/USGS dynamic earthquake rupture code validation exercise, *Seismol. Res. Lett.*, p. in press, 2009.

Heaton, T. H., Evidence for and implications of self-healing pulses of slip in earthquake rupture, *Phys. Earth Planet. Inter.*, *64*, 1–20, 1990.

Hestenes, M. R., and E. Stiefel, Methods of conjugate gradients for solving linear systems, *J. Res. Nat. Bur. Stand.*, *49*, 409–436, 1952.

Hill, D. P., et al., Seismicity remotely triggered by the magnitude 7.3 Landers, California, earthquake, *Science*, *260*, 1,617–1,623, 1993.

Hsu, Y.-J., M. Simons, J.-P. Avouac, J. Galetzka, K. Sieh, M. Chlieh, D. Natawidjaja, L. Prawirodirdjo, and Y. Bock, Frictional Afterslip Following the 2005 Nias-Simeulue Earthquake, Sumatra, *Science*, *312*, doi:10.1126/science.1126960, 2006.

Ida, Y., The maximum acceleration of seismic ground motion, *Bull. Seismol. Soc. Am., 63*, 959–968, 1973.

Igarashi, T., T. Matsuzawa, and A. Hasegawa, Repeating earthquakes and interplate aseismic slip in the northeastern Japan subduction zone, *J. Geophys. Res., 108(B5)*, doi: 10.1029/2002JB001920, 2003.

Ito, T., S. Yoshioka, and S. Miyazaki, Interplate coupling in northeast Japan deduced from inversion analysis of GPS data, *Earth Planet. Sci. Lett., 176*, 117–130, 2000.

Kaneko, Y., and N. Lapusta, Variability of earthquake nucleation in continuum models of rate-and-state faults and implications for aftershock rates, *J. Geophys. Res., 113*, B12312, doi:10.1029/2007JB005154, 2008.

Kaneko, Y., N. Lapusta, and J.-P. Ampuero, Spectral element modeling of spontaneous earthquake rupture on rate and state faults: Effect of velocity-strengthening friction at shallow depths, *J. Geophys. Res., 113*, B09317, doi:10.1029/2007JB005553, 2008.

Kato, N., and T. E. Tullis, A composite rate- and state-dependent law for rock friction, *Geophys. Res. Lett., 28(6)*, 1,103–1,106, 2001.

Komatitsch, D., and J. Tromp, Introduction to the spectral element method for three-dimensional seismic wave propagation, *Geophys. J. Int., 139*, 806–822, 1999.

Komatitsch, D., and J.-P. Vilotte, The spectral element method: An efficient tool to simulate the seismic response of 2D and 3D geological structures, *Bull. Seismol. Soc. Am., 88*, 368–392, 1998.

Komatitsch, D., S. Tsuboi, and J. Tromp, The spectral-element method in seismology, in *The Seismic Earth, Geophys. Monogr. Ser.* edited by A. Levander and G. Nolet, AGU, Washington D.C., *157*, 205–227, 2005.

Konca, O. A., et al., Partial rupture of a locked patch of the Sumatra megathrust during the 2007 earthquake sequence, *Nature*, *456*, 631–635, doi:10.1038/nature07572, 2008.

Lapusta, N., Elastodynamic analysis of sliding with rate and state friction, Ph.D. thesis, Harvard University, Cambridge, MA, 2001.

Lapusta, N., and Y. Liu, 3D boundary-integral modeling of spontaneous earthquake sequences and aseismic slip, *J. Geophys. Res.*, 2009.

Lapusta, N., and J. R. Rice, Nucleation of rate and state frictional instability under non-uniform loading, *EOS Trans. Am. Geophys. Union*, *83(47)*, Fall Meet. Suppl., Abstract S61E–05, 2002.

Lapusta, N., and J. R. Rice, Nucleation and early seismic propagation of small and large events in a crustal earthquake model, *J. Geophys. Res.*, *108*(B4), doi:10.1029/2001JB000793, 2003.

Lapusta, N., J. Rice, Y. Ben-Zion, and G. Zheng, Elastodynamic analysis for slow tectonic loading with spontaneous rupture episodes on faults with rate- and state-dependent friction, *J. Geophys. Res.*, *105*(B10), 23,765–23,789, 2000.

Lehner, F., V. Li, and J. Rice, Stress diffusion along rupturing plate boundaries, *J. Geophys. Res.*, *86*, 6,155–6,169, 1981.

Liu, Y., and J. R. Rice, Aseismic slip transients emerge spontaneously in 3D rate and state modeling of subduction earthquake sequences, *J. Geophys. Res.*, *110*, B08307, doi:10.1029/2004JB003424, 2005.

Lu, X., N. Lapusta, and A. J. Rosakis, Pulse-like and crack-like ruptures in experiments mimicking crustal earthquakes, *Proc. Natl. Acad. Sci. U.S.A.*, p. 10.1073/pnas.0704268104, 2007.

Lyons, S. N., Y. Bock, and D. T. Sandwell, Creep along the Imperial fault, Southern California, from GPS measurements, *J. Geophys. Res.*, *107*, doi:10.1029/2001JB000763, 2002.

Madariaga, R., J.-P. Ampuero, and M. Adda-Bedia, Seismic radiation from simple models of earthquakes, *Earthquakes: Radiated Energy and the Physics of Faulting*. Ed. R. Abercrombie, A. McGarr, H. Kanamori, and G. di Toro, *AGU Monograph*, *170*, 223–236, 2006.

Marone, C., Laboratory-derived friction laws and their application to seismic faulting, *Annu. Rev. Earth Planet. Sci.*, *26*, 643–696, 1998.

Marone, C., C. H. Scholz, and R. Bilham, On the mechanics of earthquake afterslip, *J. Geophys. Res.*, *96*, 8,441–8,452, 1991.

Miyazaki, S., P. Segall, J. Fukuda, and T. Kato, Space time distribution of afterslip following the 2003 Tokachi-oki earthquake: Implications for variations in fault zone frictional properties, *Geophys. Res. Lett.*, *31*, L21603, doi:10.1029/2004GL021457, 2004.

Miyazaki, S., P. Segall, J. McGuire, T. Kato, and Y. Hatanaka, Spatial and temporal evolution of stress and slip rate during the 2000 Tokai slow earthquake, *J. Geophys. Res.*, *111*, doi:10.1029/2004JB003426, 2006.

Murray, J., and P. Segall, Testing time-predictable earthquake recurrence by direct measurement of strain accumulation and release, *Nature*, *419*, 287–291, 2002.

Nadeau, R. M., and T. V. McEvilly, Periodic pulsing of characteristic microearthquakes on the San Andreas fault, *Science*, *303*, 220–222, 2004.

Natawidjaja, D. H., K. Sieh, M. Chlieh, J. Galetzka, B. W. Suwargadi, H. Cheng, R. L. Edwards, J. P. Avouac, and S. N. Ward, Source parameters of the great Sumatran megathrust earthquakes of 1797 and 1833 inferred from coral microatolls, *J. Geophys. Res.*, *111*, B06403, doi:10.1029/2005JB004025, 2006.

Nur, A., and J. Booker, Aftershocks caused by pore fluid flow?, *Science*, *175*, 885–887, 1972.

Oglesby, D. D., R. J. Archuleta, and S. B. Nielsen, Earthquakes on dipping faults: The effects of broken symmetry, *Science*, *280*, 1,055–1,059, 1998.

Olsen, K. B., Site amplification in the Los Angeles basin from three-dimensional modeling of ground motion, *Bull. Seismol. Soc. Am.*, *90(6B)*, S77–S94, 2000.

Perfettini, H., and J. P. Avouac, Postseismic relaxation driven by brittle creep: A possible mechanism to reconcile geodetic measurements and the decay rate of aftershocks, applications to the Chi-Chi earthquake, Taiwan, *J. Geophys. Res.*, *109*, doi: 10.1029/2003JB002488, 2004.

Perfettini, H., J. Schmittbuhl, and A. Cochard, Shear and normal load perturbations on a two-dimensional continuous fault: 1. Static triggering, *J. Geophys. Res.*, *108*(B10), doi:10.1029/2002JB001804, 2003.

Polet, J., and H. Kanamori, Shallow subduction zone earthquakes and their tsunamigenic potential, *Geophys. J. Int.*, *142*, 684–702, 2000.

Rice, J. R., The mechanics of earthquake rupture, in *Physics of the Earth's Interior, Proc. Int. Sch. Phys. Enrico Fermi, Course 78, [*edited by A. M. Dziewonski and E. Boschi, Elsevier, New York.

Rice, J. R., Spatio-temporal complexity of slip on a fault, *J. Geophys. Res.*, *98*(B6), 9,885–9,907, 1993.

Rice, J. R., Heating and weakening of faults during earthquake slip, *J. Geophys. Res.*, *111*, doi:10.1029/2005JB004006, 2006.

Rice, J. R., and Y. Ben-Zion, Slip complexity in earthquake fault models, *Proc. Natl. Acad. Sci. U.S.A.*, *93*, 3,811–3,818, 1996.

Rice, J. R., and A. L. Ruina, Stability of steady frictional slipping, *J. Appl. Mech*, *50*, 343–349, 1983.

Rice, J. R., N. Lapusta, and K. Ranjith, Rate and state dependent friction and the stability of sliding between elastically deformable solids, *J. Mech. Phys. Solids*, *49*, 1,865–1,898, 2001.

Rojas, O., E. Dunham, S. Day, L. A. Dalguer, and J. Castillo, Finite difference modeling of rupture propagation with strong velocity-weakening friction, *SCEC 2007 Annual Meeting*, 2007.

Rubin, A. M., and J.-P. Ampuero, Earthquake nucleation on (aging) rate and state faults, *J. Geophys. Res.*, *110*, doi:10.1029/2005JB003686, 2005.

Ruina, A. L., Slip instability and state variable friction laws, *J. Geophys. Res.*, *88*, 10,359–10,370, 1983.

Rybicki, K. R., Strike-slip faulting in the presence of low-rigidity inhomogeneities, *Bull. Seismol. Soc. Am.*, *82(5)*, 2,170–2,190, 1992.

Rybicki, K. R., and T. Yamashita, Faulting in vertically inhomogeneous media and its geophysical implications, *Geophys. Res. Lett.*, *25(15)*, 2,893–2,896, 1998.

Schaff, D. P., G. H. R. Bokelmann, G. C. Beroza, F. Waldhauser, and W. L. Ellsworth, High resolution image of Calaveras Fault seismicity, *J. Geophys. Res.*, *107(B9)*, doi:10.1029/2001JB000633, 2002.

Scholz, C. H., Slip instability and state variable friction laws, *Nature*, *391*, 37–42, 1998.

Schwartz, D. P., and K. J. Coppersmith, Fault behavior and characteristic earthquakes: Examples from the Wasatch and San Andreas fault zones, *J. Geophys. Res.*, *89*, 5,681–5,698, 1984.

Schwartz, S. Y., Noncharacteristic behavior and complex recurrence of large subduction zone earthquakes, *J. Geophys. Res.*, *104*, 23,111–23,125, 1999.

Schwartz, S. Y., and J. M. Rokosky, Slow slip events and seismic tremor at Circum-Pacific subduction zones, *Rev. Geophys.*, *45*, RG3004, doi:10.1029/2006RG000208, 2007.

Seno, T., Tsunami earthquakes as transient phenomena, *Geophys. Res. Lett.*, *29(10)*, 10.1029/2002GL014,868, 2002.

Shearer, P., E. Hauksson, and G. Lin, Southern California hypocenter relocation with waveform cross-correlation, Part 2: Results using source-specific station terms and cluster analysis, *Bull. Seismol. Soc. Am.*, *95(3)*, 904–915, 2005.

Shimazaki, K., and T. Nakata, Time-predictable recurrence model for large earthquakes, *Geophys. Res. Lett.*, *7*, 279–282, doi:10.1029/GL007i004p00279, 1980.

Sieh, K., et al., Earthquake supercycles inferred from sea-level changes recorded in the corals of west Sumatra, *Science*, *322*, doi:10.1126/science.1163589, 2008.

Thatcher, W., Order and diversity in the modes of Circum-Pacific earthquake recurrence, *J. Geophys. Res.*, *91*, 2,609–2,623, 1990.

Tian, Y., and A. M. Rubin, Abrupt turnoff of aftershocks after a major earthquake, *AGU Chapman conference abstract*, p. 59, 2005.

Toda, S., R. S. Stein, P. A. Reasenberg, J. H. Dieterich, and A. Yoshida, Stress transferred by the 1995 Mw = 6.9 Kobe, Japan, shock: Effect on aftershocks and future earthquake probabilities, *J. Geophys. Res.*, *103*(B10), 24,543–24,565, 1998.

Toda, S., R. S. Stein, K. Richards-Dinger, and S. B. Bozkurt, Forecasting the evolution of seismicity in Southern California: Animations built on earthquake stress transfer, *J. Geophys. Res.*, *110*(B05S16), doi:10.1029/2004JB003415, 2005.

Toro, G. D., D. L. Goldsby, and T. E. Tullis, Friction falls towards zero in quartz rock as slip velocity approaches seismic rates, *Nature*, *427*, doi:10.1038/nature02249, 2003.

Trefethen, L. N., and D. Bau, *Numerical Linear Algebra*, Society for Industrial and Applied Mathematics, Philadelphia, PA, 1997.

Tse, S., and J. R. Rice, Spacio-temporal complexity of slip on a fault, *J. Geophys. Res.*, *91*, 9,452–9,472, 1986.

Tullis, T. E., Rock friction constitutive behavior from laboratory experiments and its implications for an earthquake prediction field monitoring program, *Pure Appl. Geophys.*, *126*, 555–588, 1988.

Tullis, T. E., Rock friction and its implications for earthquake prediction examined via models of Parkfield earthquakes, *Proc. Natl. Acad. Sci. U.S.A.*, *93*, 3,803–3,810, 1996.

Utsu, T., Y. Ogata, and R. Matsu'ura, The centenary of the Omori formula for a decay law of aftershock activity, *J. Geophys. Res.*, *43*, 1–33, 1995.

Vilotte, J.-P., G. Festa, and J.-P. Ampuero, Dynamic fault rupture propagation using non-smooth spectral element method, *EOS Trans. Am. Geophys. Union*, *87(52)*, Fall Meet. Suppl., S52B–05, 2006.

Waldhauser, F., W. L. Ellsworth, D. P. Schaff, and A. Cole, Streaks, multiplets, and holes: High-resolution spatio-temporal behavior of Parkfield seismicity, *Geophys. Res. Lett.*, *31*, L18608, doi:10.1029/2004GL020649, 2004.

Weldon, R., T. Fumal, and G. Biasi, Wrightwood and the earthquake cycle: What a long recurrence record tells us about how faults works, *GSA Today*, *14*, 4–10, 2004.

Wesnousky, S. G., Predicting the endpoints of earthquake ruptures, *Nature*, *444*, 358–360, doi:10.1038/nature05275, 2006.

Yamanaka, Y., and M. Kikuchi, Asperity map along the subduction zone in northeastern Japan inferred from regional seismic data, *J. Geophys. Res.*, *109*, B07307, doi:10,1029/ 2003JB002683, 2004.

Zampieri, E., and L. F. Pavarino, Implicit spectral element methods and Neumann-Neumann preconditioners for acoustic waves, *Comput. Methods Appl. Mech. Engrg.*, *195*, 2,649–2,673, 2006.

Zheng, G., and J. R. Rice, Conditions under which velocity-weakening friction allows a self-healing versus a cracklike mode of rupture, *Bull. Seismol. Soc. Am.*, *88*, 1,466–1,483, 1998.